nature portfolio

https://doi.org/10.1038/s41586-022-04978-6

Supplementary information

Floating perovskite-$BiVO_4$ devices for scalable solar fuel production

In the format provided by the authors and unedited

Supplementary Information for:

Floating perovskite-$BiVO_4$ devices for scalable solar fuel production

Virgil Andrei,[1,2†] Geani M. Ucoski,[1†] Chanon Pornrungroj,[1] Chawit Uswachoke,[3] Qian Wang,[1] Demetra S. Achilleos,[1] Hatice Kasap,[1] Katarzyna P. Sokol,[1] Robert A. Jagt,[4] Haijiao Lu,[1] Takashi Lawson,[1] Andreas Wagner,[1] Sebastian D. Pike,[1] Dominic S. Wright,[1] Robert L. Z. Hoye,[2,5] Judith L. MacManus-Driscoll,[4] Hannah J. Joyce,[3] Richard H. Friend,[2] and Erwin Reisner[1*]

[1] *Yusuf Hamied Department of Chemistry, University of Cambridge, Lensfield Road, Cambridge CB2 1EW, United Kingdom.*

[2] *Optoelectronics Group, University of Cambridge, Cavendish Laboratory, J J Thomson Avenue, Cambridge CB3 0HE, United Kingdom.*

[3] *Electronic and Photonic Nanodevices, Department of Engineering, University of Cambridge, Electrical Engineering Building, 9 J J Thomson Avenue, Cambridge CB3 0FA, United Kingdom.*

[4] *Department of Materials Science and Metallurgy, University of Cambridge, 27 Charles Babbage Rd, Cambridge CB3 0FS, United Kingdom.*

[5] *Department of Materials, Imperial College London, Exhibition Road, London SW7 2AZ, United Kingdom.*

*To whom correspondence should be addressed; E-mail: reisner@ch.cam.ac.uk.

† These authors contributed equally.

Supplementary Table 1 | Electrocatalytic activity of graphite paste electrodes with a CoMTPP@CNT CO_2 reduction catalyst under different applied potentials. CNT sheets are incubated in a 0.05 mM CoMTPP solution in DMF. Fresh graphite paste is used to attach the CoMTPP@CNT sheets to a FTO|Ag support. E - applied potential against the reversible hydrogen electrode (RHE); FY - faradaic yield; n - amount of products; TON - turnover number; TOF - turnover frequency (see Supplementary Table 2 for Co loading). Data obtained from the 4 h CPE at different potentials is plotted in Supplementary Fig. 5.

E (V vs. RHE)	FY_{H2} (%)	FY_{CO} (%)	FY_{total} (%)	Ratio CO:H_2 (–)	n_{H2} (μmol cm^{-2})	n_{CO} (μmol cm^{-2})	TON_{H2} (–)	TON_{CO} (–)	TOF_{H2} (h^{-1})	TOF_{CO} (h^{-1})
-0.4	32.7±5.4	0.5±0.9	33.2±6.0	0.01±0.03	0.7±0.2	0.01±0.02	72.5±18.4	1.2±2.1	18.1±4.6	0.3±0.5
-0.5	22.6±13.1	39.2±26.4	61.8±17.4	2.45±2.23	3.6±1.6	9.6±12.0	392±179	1054±1317	98±45	263±329
-0.6	20.6±4.6	67.5±6.5	88.1±2.8	3.45±1.20	12.1±1.9	40.1±7.2	1322±207	4395±786	331±52	1099±197
-0.7	32.0±5.4	62.8±8.8	94.7±3.4	2.04±0.66	23.0±4.4	45.4±9.0	2525±485	4980±990	631±121	1245±248
-0.8	39.6±7.4	59.0±10.9	98.6±4.7	1.56±0.55	46.5±10.6	69.0±12.0	5103±1166	7569±1319	1276±292	1892±330

Supplementary Table 2 | Electrocatalytic activity of the graphite epoxy (GE) electrodes with different CO_2 and proton reduction catalysts. The graphite paste is spread on top of FTO|Ag, and the edges are sealed with epoxy, similar with the assembly of a perovskite photocathode. A 5 nm layer of Pt is sputtered on top of the graphite paste for H_2 evolution experiments, while carbon nanotube (CNT) sheets incubated in CoMTPP solutions of various concentrations are attached on the fresh paste for CO_2 reduction (Supplementary Fig. 6). c_{CoMTPP} - concentration of CoMTPP in DMF; FY - faradaic yield; n - amount of products; TON - turnover number; TOF - turnover frequency. [a] TON and TOF are calculated using the reported cobalt loading before the 4 h controlled potential electrolysis (CPE) at −0.6 V vs. RHE.[1] [b] CPE at −0.2 V vs. RHE using a GE|Pt electrode. [c] Electrolysis on a bare graphite paste electrode reveals a negligible catalytic activity even at −0.6 V vs. RHE, indicating a complete coverage of the underlying metal film.

c_{CoMTPP} (mM)	FY_{H2} (%)	FY_{CO} (%)	FY_{total} (%)	Ratio CO:H_2 (–)	n_{H2} (μmol cm^{-2})	n_{CO} (μmol cm^{-2})	$Loading_{Co}$ [a] (nmol cm^{-2})	TON_{H2} (–)	TON_{CO} (–)	TOF_{H2} (h^{-1})	TOF_{CO} (h^{-1})
0.01	20.3±1.7	59.8±7.9	80.1±6.3	2.99±0.65	6.0±1.0	17.6±0.9	4.09±0.63	1476±253	4303±217	369±63	1076±54
0.05	20.6±4.6	67.5±6.5	88.1±2.8	3.45±1.20	12.1±1.9	40.1±7.2	9.12±0.65	1322±207	4395±786	331±52	1099±197
0.1	38.4±5.5	56.2±6.0	94.6±0.6	1.50±0.34	39.9±9.1	57.9±6.9	14.03±1.10	2846±646	4123±495	711±161	1031±124
0.5	39.1±10.1	48.4±9.5	87.5±0.6	1.35±0.63	39.2±22.0	43.8±7.0	42.82±4.55	914±513	1023±163	229±128	256±41
1	44.6±3.2	47.8±5.9	92.4±3.5	1.08±0.20	44.2±5.1	48.3±14.5	60.60±3.37	729±84	798±239	182±21	199±60
0[b]	91.4±0.8	–	91.4±0.8	–	89.3±7.8	–	–	–	–	–	–
0[c]	23.3±10.0	–	23.3±10.0	–	0.036±0.025	–	–	–	–	–	–

Supplementary Table 3 | Electronic properties of various electrically conductive substrates. R - electrical resistance, h - sample thickness, $R\,\square^{-1}$ - sheet resistance, σ - electrical conductivity. The raw electrical resistance is measured in a two-point configuration, as depicted in Supplementary Fig. 7 for the individual samples. A parasitic contact resistance below 1 Ω is estimated from the data recorded on a 100 nm Ag layer.

Sample	R (Ω)	h (μm)	$R\,\square^{-1}$ ($\Omega\,\square^{-1}$)	σ ($S\,m^{-1}$)
GE in-plane	379±97	425±65	759±194	3.23±0.53
GE cross-plane	6.67±0.79	507±6	–	0.95±0.11
CNT-in-plane	3.75±0.36	77.1±4.8	4.38±0.42	2977±183
CNT-cross-plane	0.85±0.07	77.1±4.8	–	1.35±0.15
Ag-in-plane	0.89±0.05	0.100	–	–

Supplementary Table 4 | Photoelectrochemical activity of lightweight perovskite|GE|CoMTPP@CNT photocathodes under different light intensity. $J_{0.5h}$ - steady-state photocurrent density after 30 min operation; FY - faradaic yield; n - amount of products; TON - turnover number; TOF - turnover frequency. [a] H_2 production using a fPVK|GE|Pt photocathode. [b] Effect of stirring on the selectivity of fPVK|GE|CoMTPP@CNT photocathodes. The average values obtained after 4 h CPE at 0 V vs. RHE are also plotted in Supplementary Fig. 19.

Light intensity (sun)	$J_{0.5\,h}$ @ 0 V vs. RHE ($mA\,cm^{-2}$)	FY_{H2} (%)	FY_{CO} (%)	FY_{total} (%)	Ratio CO:H_2 (–)	n_{H2} ($\mu mol\,cm^{-2}$)	n_{CO} ($\mu mol\,cm^{-2}$)	TON_{H2} (–)	TON_{CO} (–)	TOF_{H2} (h^{-1})	TOF_{CO} (h^{-1})
1[a]	-16.51±0.52	92.9±1.4	–	92.9±1.4	–	919.5±39.0	–	–	–	–	–
1	-7.86±1.41	28.9±5.0	55.4±23.5	84.3±19.5	2.04±1.11	120.1±42.6	214.6±65.4	3840±1722	6863±2812	960±431	1716±703
0.5	-4.46±0.40	23.0±2.8	72.8±1.0	95.7±3.8	3.19±0.33	52.9±8.3	167.3±12.2	1776±473	5617±1277	444±118	1404±319
0.2	-2.92±0.73	16.8±3.9	78.0±5.8	94.8±9.2	4.80±1.03	30.7±14.9	138.8±51.9	985±488	4458±1722	246±122	1115±431
0.1	-1.86±0.09	13.5±0.9	76.5±2.9	90.0±2.5	5.68±0.55	17.0±0.8	96.7±10.9	557±137	3168±844	139±34	792±211
0.1[b]	-2.15±0.49	10.8±0.4	77.6±4.7	88.3±5.1	7.19±0.21	14.3±2.5	102.7±16.0	508±137	3648±934	127±34	912±233

Supplementary Table 5 | Photoelectrochemical performance of lightweight perovskite-$BiVO_4$ devices of different sizes. $J_{0.5h}$ - steady-state photocurrent density after 30 min operation; FY - faradaic yield; n - amount of products; TON - turnover number; TOF - turnover frequency. STH/C/O - solar-to-H_2/CO/O_2 conversion efficiency. [a] Wired devices. [b] Standalone artificial leaves. The average values obtained during unassisted operation for 10 h (small-scale) or 18 h (large-scale) are also plotted in Supplementary Fig. 33. Deviations in the faradaic yield or in the ratio of reduction to oxidation products originate mainly from bubble trapping and solubilised products, which become more noticeable in case of the floating devices.

Catalyst	Area (cm^2)	FY_{H_2} (%)	FY_{CO} (%)	FY_{total} (%)	FY_{O_2} (%)	Ratio CO:H_2 (–)	n_{H_2} (μmol cm^{-2})	n_{CO} (μmol cm^{-2})	n_{O_2} (μmol cm^{-2})
Pt [a]	1.7	81.0±15.9	–	81.0±15.9	56.1±17.4	–	60.4±21.9	–	19.9±9.5
CoMTPP [a]	1.7	24.0±4.6	56.6±4.1	80.6±4.3	58.2±5.5	2.34±0.48	1.9±0.2	4.5±0.5	2.2±0.3
Pt [b]	100	–	–	–	–	–	23.9	–	13.4
CoMTPP [b]	100	–	–	–	–	0.65	4.9	3.2	4.7

Catalyst	Area (cm^2)	$J_{0.5\,h}$ (mA cm^{-2})	TON_{H_2} (–)	TON_{CO} (–)	TOF_{H_2} (h^{-1})	TOF_{CO} (h^{-1})	STH (%)	STC (%)	STO (%)
Pt [a]	1.7	0.58±0.10	–	–	–	–	0.578±0.152	–	0.401±0.143
CoMTPP [a]	1.7	0.070±0.007	514±80	1186±182	51±8	119±18	0.021±0.004	0.053±0.006	0.053±0.007
Pt [b]	100	–	–	–	–	–	–	–	–
CoMTPP [b]	100	–	2867	1853	159	103	–	–	–

Supplementary Table 6 | Comparison between the performance of various natural and artificial photosynthetic systems. Distinct technologies are compared using commonly reported parameters, as well as unified metrics calculated under the following assumptions. **1** - The activity per gram refers to the mass of the entire setup, including light absorbing unit, catalyst, encapsulant and substrate, without reagents and electrolyte solution (the fresh mass is employed for plant leaves). **2** - The area of a setup corresponds to the projected surface occupied by the light absorber (in case of PC performed in vials, we assume that 1 mL solution corresponds to 1 cm^2 irradiated area). A plot of the product rate against the activity per gram for different technologies is given in Fig. 3 from the main text. [a] Whole device area (i.e. combined area of perovskite and $BiVO_4$). [b] Estimated values (masses were estimated based on the volumes of materials used and their density, or using similar systems). [c] Assuming the dry mass is 12% of the fresh mass.[4,5] Abbreviations: PEC – photoelectrocatalysis, fPVK – flexible perovskite photocathode, FM – Field's metal, H_2ase – hydrogenase, PC – photocatalysis, SED – sacrificial electron donor, CN_x – carbon nitride, CDs – carbon dots, QDs – quantum dots, PET – polyethylene terephthalate, 4-MBA – 4-methylbenzyl alcohol, EDTA – ethylenediaminetetraacetic acid, TEOA – triethanolamine, AA – ascorbic acid, asm – assimilation.

Sample	m ($mg\ cm^{-2}$)	J ($mA\ cm^{-2}$)	STF (%)	n ($\mu mol\ cm^{-2}$)	Rate ($\mu mol\ cm^{-2}\ h^{-1}$)	Activity ($\mu mol\ g^{-1}\ h^{-1}$)	Product	Comments	Ref.
Unassisted PEC devices									
Ti|$BiVO_4$|TiCo – fPVK|GE|CoMTPP@CNT	92	0.070[a]	0.053[a]	4.48[a]	0.448[a]	4.88	CO	syngas + water splitting	this work
			0.021[a]	1.94[a]	0.194[a]	2.11	H_2		
			0.053[a]	2.24[a]	0.224[a]	2.44	O_2		
Ti|$BiVO_4$|TiCo – fPVK|GE|Pt	86	0.58[a]	0.578[a]	60.4[a]	6.04[a]	70.6	H_2	water splitting	this work
			0.401[a]	19.9[a]	1.99[a]	23.2	O_2		
Ti|$BiVO_4$|TiCo – fPVK|GE|CoMTPP@CNT	47			3.18[a]	0.18[a]	3.73	CO	syngas + water splitting,	this work
				4.93[a]	0.27[a]	5.77	H_2	wireless, 100 cm^2	
				4.69[a]	0.26[a]	5.49	O_2		
Ti|$BiVO_4$|TiCo – fPVK|GE|Pt	33			23.9[a]	1.33[a]	40.2	H_2	water splitting, wireless,	this work
				13.4[a]	0.74[a]	22.4	O_2	100 cm^2	
$BiVO_4$ – PVK|FM|CoMTPP@CNT	1390	0.18	0.018	1.8	0.18	0.13	CO	syngas + water splitting	1
			0.056	5.8	0.58	0.42	H_2		
			0.146	6.8	0.68	0.49	O_2		
$BiVO_4$ – PVK|FM|H_2ase	1670[b]	1.1	1.1	21.2	2.65	1.59	H_2	water splitting	2
			0.677	9	1.13	0.68	O_2		
Ti|RuO_2 – GaAs|GaInAs|GaInP|AlInP|TiO_2|Rh	806[b]	15.7	19.3	447	179	222	H_2	water splitting, pH 0	3
				245	98	122	O_2		
PEC photoelectrodes									
fPVK|GE|CoMTPP@CNT	71	-7.86		215	53.7	751	CO	syngas, 0 V vs. RHE	this work
				120	30	420	H_2		
fPVK|GE|Pt	54	-16.5		919	230	4266	H_2	0 V vs. RHE	this work
PVK|FM|CoMTPP@CNT	940[b]	-5.61		53.4	13.3	14.1	CO	syngas, 0 V vs. RHE	1
				280	70	74.2	H_2		

Supplementary Table 6 | Continued.

Sample	m (mg cm^{-2})	J (mA cm^{-2})	STF (%)	n (µmol cm^{-2})	Rate (µmol cm^{-2} h^{-1})	Activity (µmol g^{-1} h^{-1})	Product	Comments	Ref.
Unassisted PC									
Cr_2O_3/Ru-$SrTiO_3$:La,Rh/Au/$BiVO_4$:Mo sheets	260[b]		1.1	196	19.6	74.9	H_2	water splitting	6
				98	9.8	37.5	O_2		
CotpyP/$SrTiO_3$:La,Rh/Au/$BiVO_4$:Mo/RuO_2	260[b]		0.08	6.53	1.09	4.16	HCOOH	aqueous formate production	7
sheets				0.18	0.03	0.11	H_2		
				3.12	0.52	1.99	O_2		
PC photoreforming									
activated $^{NCN}CN_x$, 50 nmol NiP	0.17			0.48	0.12	1690	H_2	SED: α-cellulose	8
activated $^{NCN}CN_x$, 50 nmol NiP	1.67			0.79	0.20	202	H_2	SED: sawdust	8
activated $^{NCN}CN_x$, H_2PtCl_6 (4 wt.%)	1.67			0.29	0.012	7.17	H_2	SED: α-cellulose	8
CDs from α-cellulose, NiP (50 nmol)	0.73			1.13	0.19	231	H_2	SED: river water impurities	9
ultra-sonicated CN_x|Ni_2P, 1 M aq. NaOH	1.60			0.039	0.0096	6.01	H_2	SED: pre-treated rubber	10
CdS QDs, 10 M aq. NaOH	0.12			1.63	0.41	3420	H_2	SED: PET (no pre-treatment)	11
CdS QDs, 10 M aq. NaOH	0.12			5.95	1.49	12400	H_2	SED: PET (with pre-treatment)	11
PC with SED									
activated $^{NCN}CN_x$, 400 nmol NiP	0.17			10.6	1.76	39310	H_2	SED: 4-MBA	8
CDs from α-cellulose, NiP (50 nmol)	0.01			0.3	0.05	13452	H_2	SED: EDTA	9,12
CDs from α-cellulose, NiP (50 nmol)	0.93			4.47	0.74	1410	H_2	SED: EDTA	9,12
mpg-CN_x|CoPPc	0.67			0.30	0.013	19	CO	SED: TEOA	13
				0.075	0.0031	4.66	H_2		
ZnSe-BF_4, 10 µM NiCycP	0.1[b]			1.17	0.29	2925	CO	SED: AA	14
				2.93	0.73	7313	H_2		
Natural photosynthesis									
plants			≤1.0						15,16
Arabidopsis thaliana Col-0s	37[c]				3.1	65	CO_2 asm.	66 days after seeding	17
	70[c]				2.3	28	CO_2 asm.	86 days after seeding	
Arabidopsis thaliana gi-2	31[c]				3.2	86	CO_2 asm.	66 days after seeding	17
	62[c]				2.7	35	CO_2 asm.	86 days after seeding	

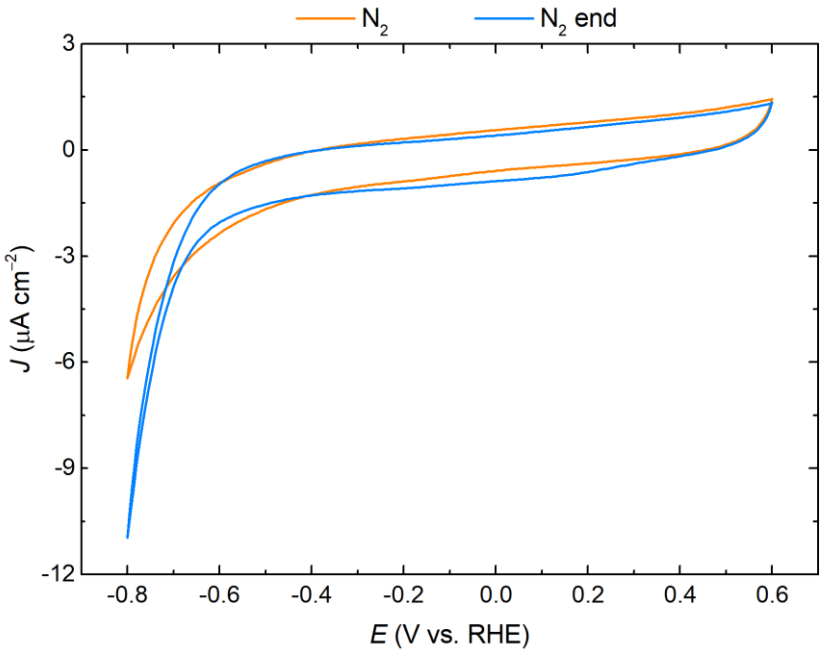

Supplementary Fig. 1 | Cyclic voltammograms (CVs) of graphite epoxy electrodes without a catalyst. CVs were recorded under N_2 atmosphere, before ("N_2") and after ("N_2 end") 4 h electrolysis at –0.6 V vs. RHE (0.1 M KB_i, 0.1 M K_2SO_4 buffer solution, pH 8.5).

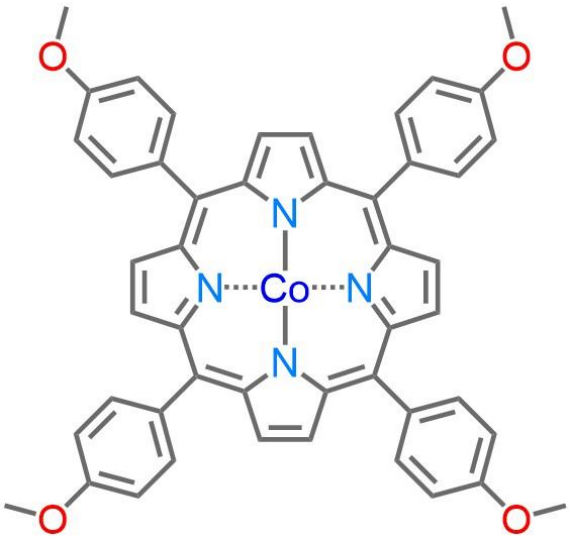

Supplementary Fig. 2 | Molecular structure of the cobalt(II) *meso*-tetrakis(4-methoxyphenyl)-porphyrin (CoMTPP) catalyst for CO_2 reduction. The catalyst is immobilised onto carbon nanotubes via π-π stacking interactions.[1]

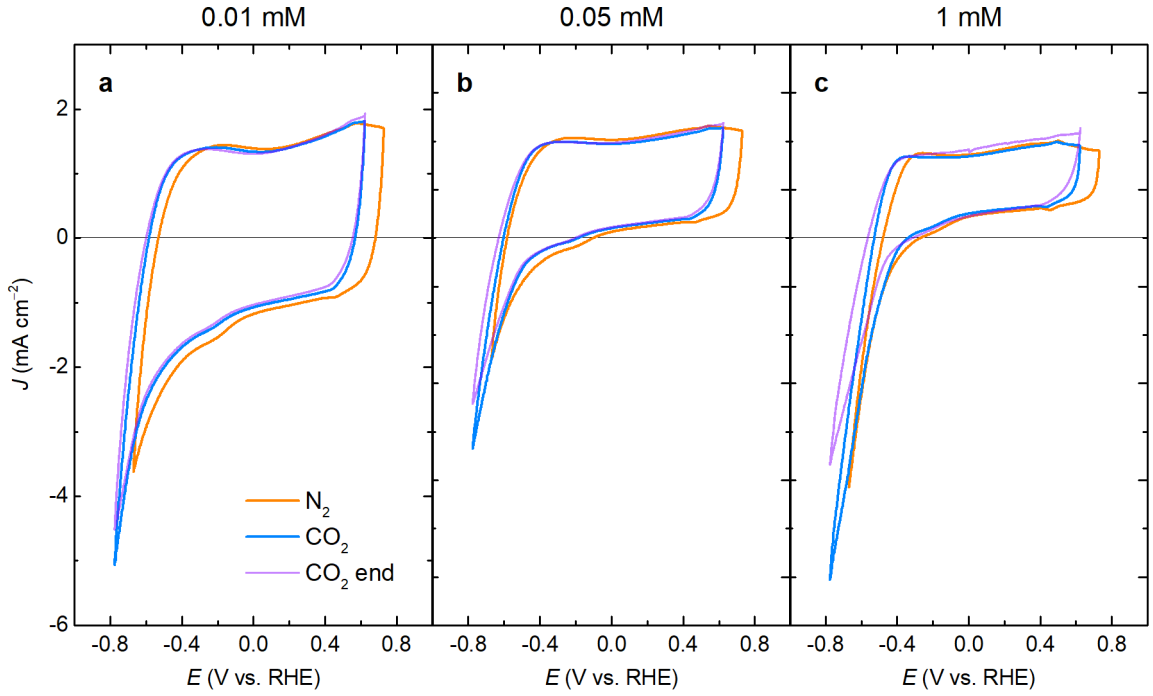

Supplementary Fig. 3 | CVs of graphite epoxy electrodes with carbon nanotube (CNT) sheets incubated in CoMTPP catalyst solutions of different concentrations. a, 0.01 mM. **b**, 0.05 mM. **c**, 1 mM. CVs are first recorded under inert N_2 atmosphere ("N_2"), then under CO_2 atmosphere before ("CO_2") and after ("CO_2 end") 4 h electrolysis at –0.6 V vs. RHE (0.5 M $KHCO_3$ buffer, at room temperature).

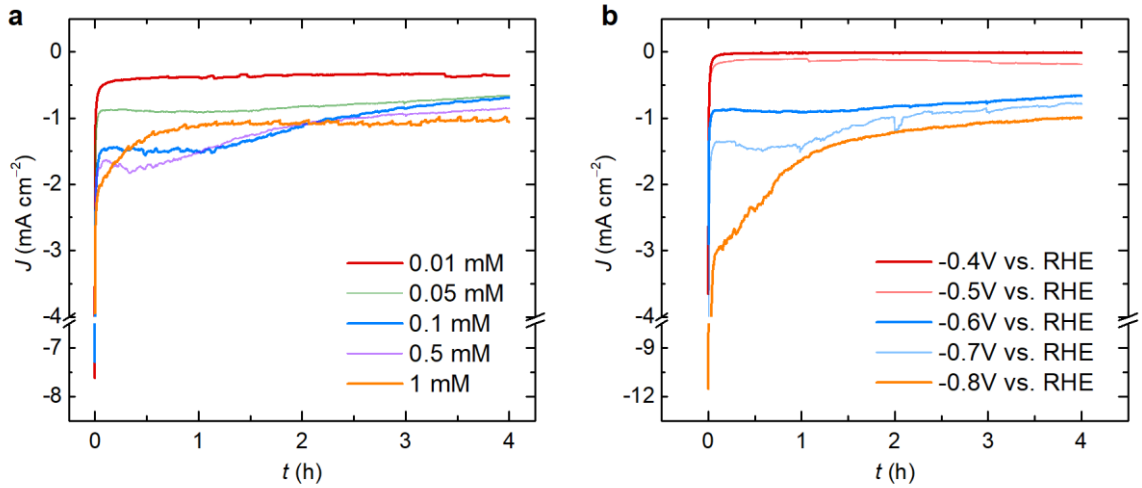

Supplementary Fig. 4 | Examples of 4 h CPE traces of the graphite epoxy electrodes with a CoMTPP@CNT CO_2 reduction catalyst. a, CNTs are incubated in CoMTPP solutions of different concentrations. **b**, CNT sheets incubated in a 0.05 mM CoMTPP solution are studied under different applied potentials (0.5 M $KHCO_3$ buffer, pH 7.4, under CO_2, at room temperature).

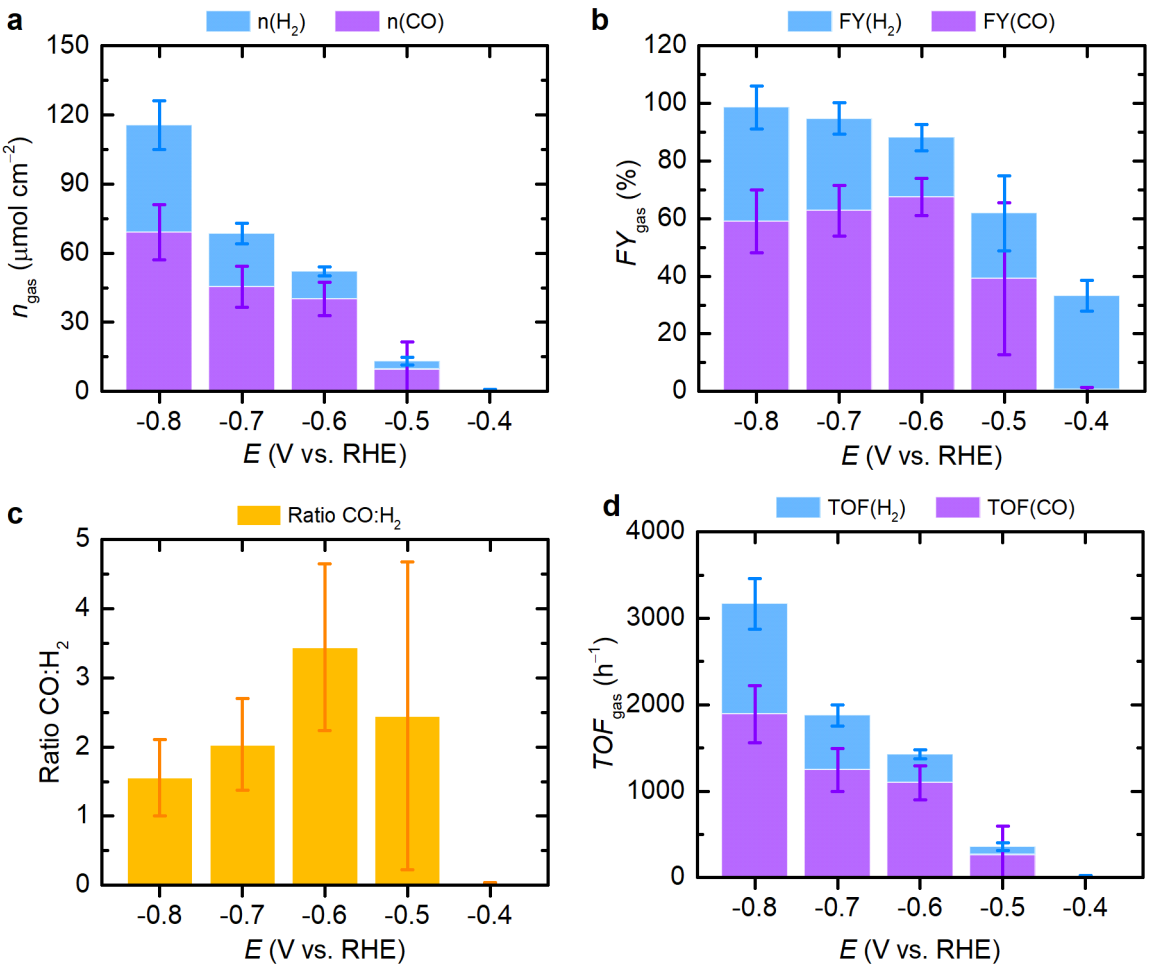

Supplementary Fig. 5 | Electrocatalytic performance of the GE|CoMTPP@CNT electrodes under different applied potentials. a, Product amounts. **b**, Faradaic yields. **c**, CO:H_2 selectivity. **d**, Turnover frequency of the CoMTPP catalyst. CNT sheets were incubated in a 0.05 mM CoMTPP solution in DMF. CPE is conducted for 4 h, in a 0.5 M $KHCO_3$ electrolyte, under CO_2, at room temperature.

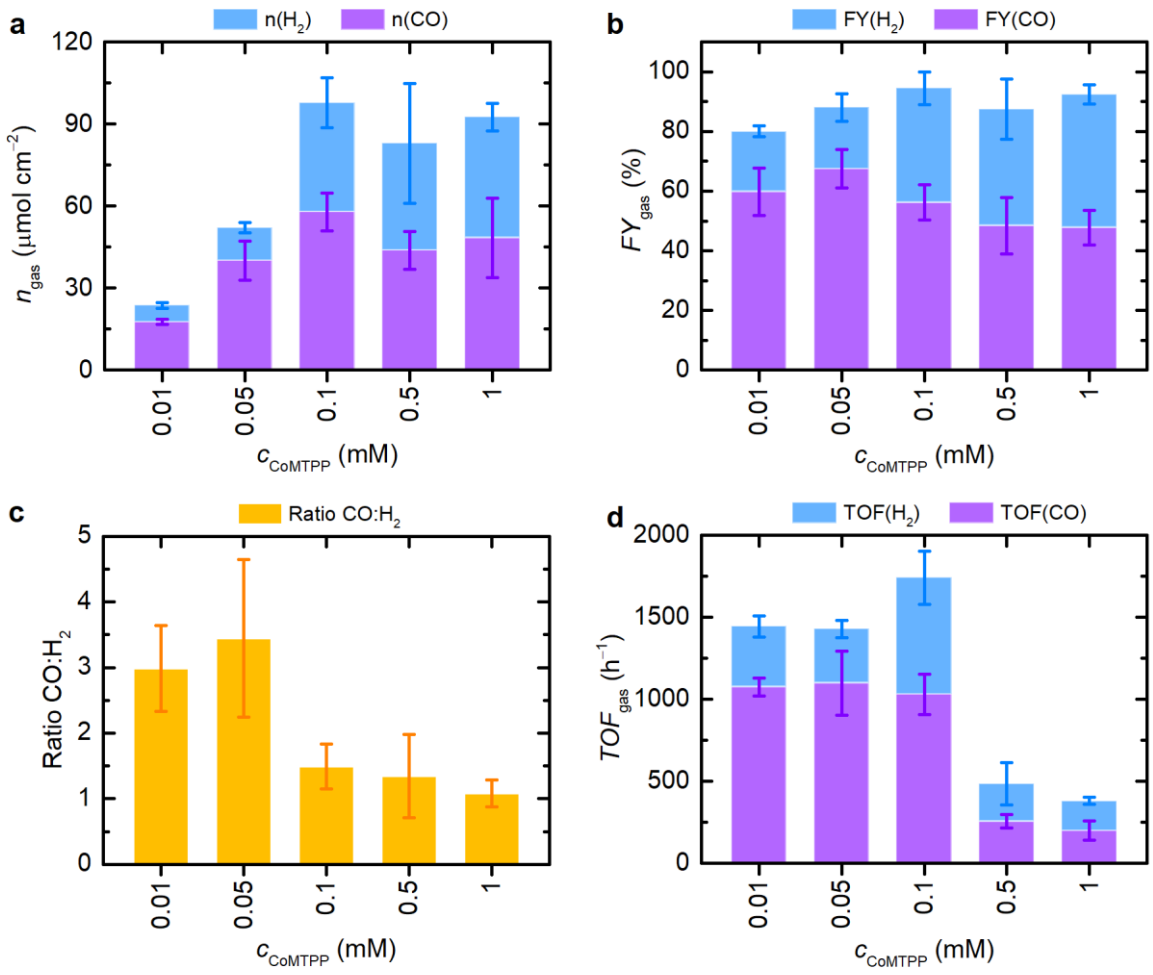

Supplementary Fig. 6 | Electrocatalytic performance of the GE|CoMTPP@CNT electrodes, where the CNT sheets are incubated in solutions of different CoMTPP concentrations. a, Product amounts. **b**, Faradaic yields. **c**, CO:H_2 selectivity. **d**, Turnover frequency. CPE is performed at −0.6 V vs. RHE for 4 h, in a 0.5 M $KHCO_3$ electrolyte, under CO_2, at room temperature.

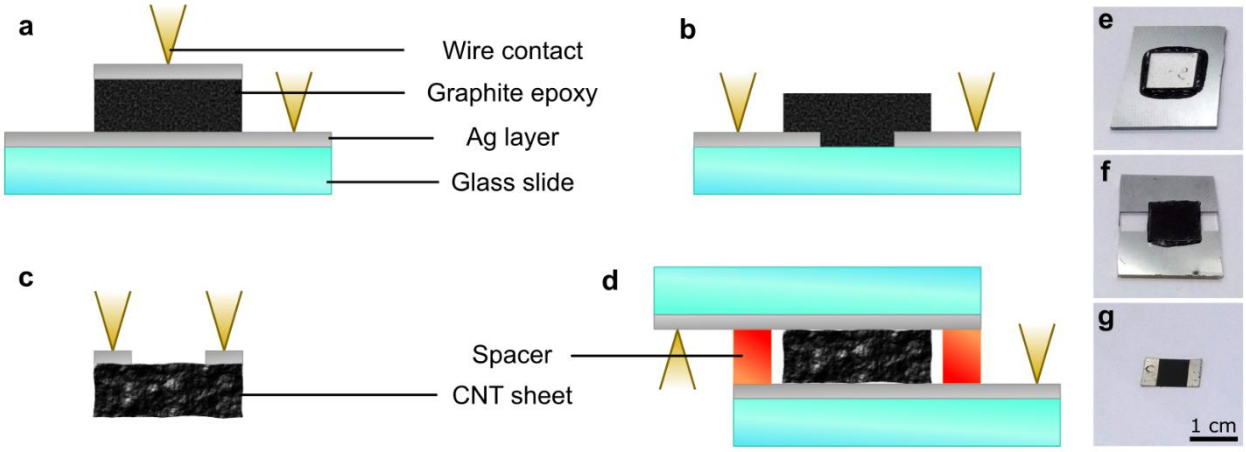

Supplementary Fig. 7 | Schematics of the configurations employed for the two-point electrical resistance measurements. a, Graphite epoxy (GE) cross-plane (CP). **b**, Graphite epoxy in-plane (IP). **c**, Carbon nanotube (CNT) sheets in-plane. **d**, Carbon nanotube sheets cross-plane. **e**-**g**, Photographs corresponding to the depictions from frames **a**-**c**: **e** - GE cross-plane; **f** - GE in-plane; **g** - CNT sheet in-plane. 100 nm Ag is deposited onto masked samples or bare glass slides as metal contacts. An even thickness of the GE is ensured by doctor-blading the graphite paste through a cardboard mask (Supplementary Table 3 and Fig. 8). Adhesive tape stripes are used as thin spacers for cross-plane measurements of CNT sheets (**d**), as the electrical resistance of porous conductive networks depends on their compression.[18,19]

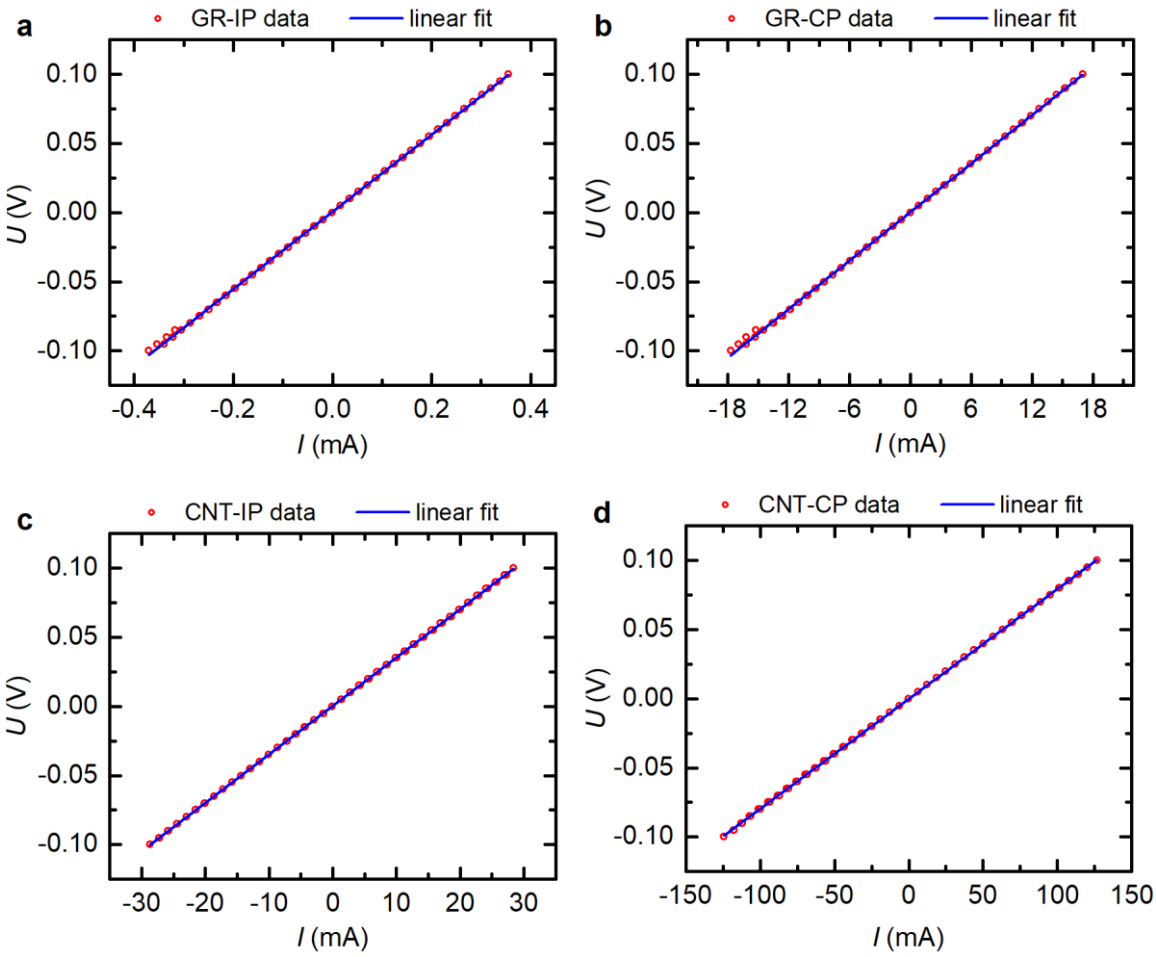

Supplementary Fig. 8 | Examples of the *U-I* data employed to calculate the electrical resistance. a, GE in-plane. **b**, GE cross-plane. **c**, CNT sheets in-plane. **d**, CNT sheets cross-plane. Red dots indicate raw data points and linear fits are depicted in blue. Forward and backward *I-U* scans are recorded between –0.1 and 0.1 V, at a 10 mV s^{-1} scan rate, contacting the samples as shown in Supplementary Fig. 7.

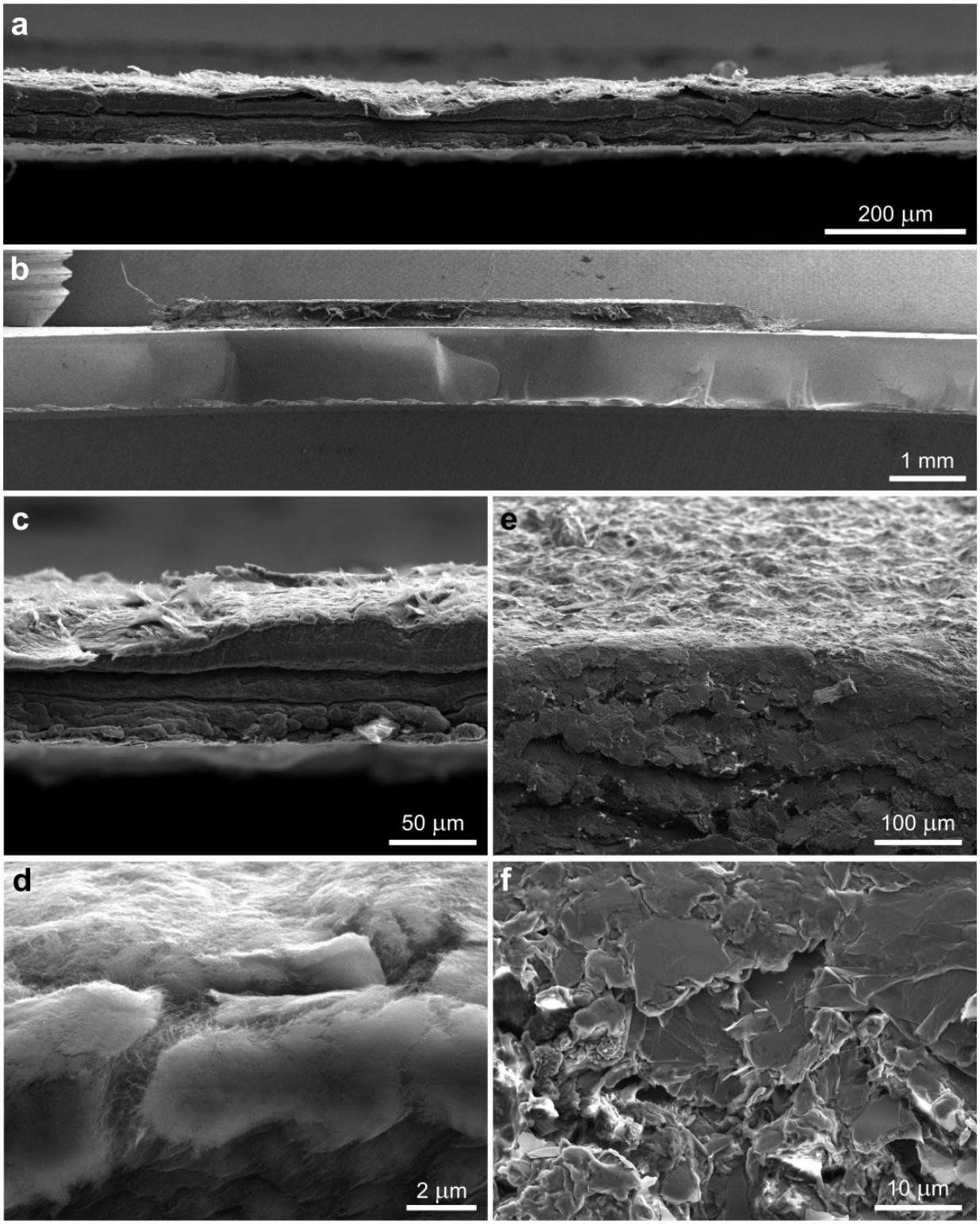

Supplementary Fig. 9 | Cross-section scanning electron microscopy (SEM) images of CNT sheets and graphite epoxy. a,**c**,**d**, Standalone CNT sheets. **b**,**e**,**f**, Graphite epoxy. The graphite paste is deposited onto a glass|Ag substrate by doctor-blading through a cardboard mask, to ensure a homogeneous film thickness for the electrical conductivity measurements (Supplementary Table 3 and Fig. 7).

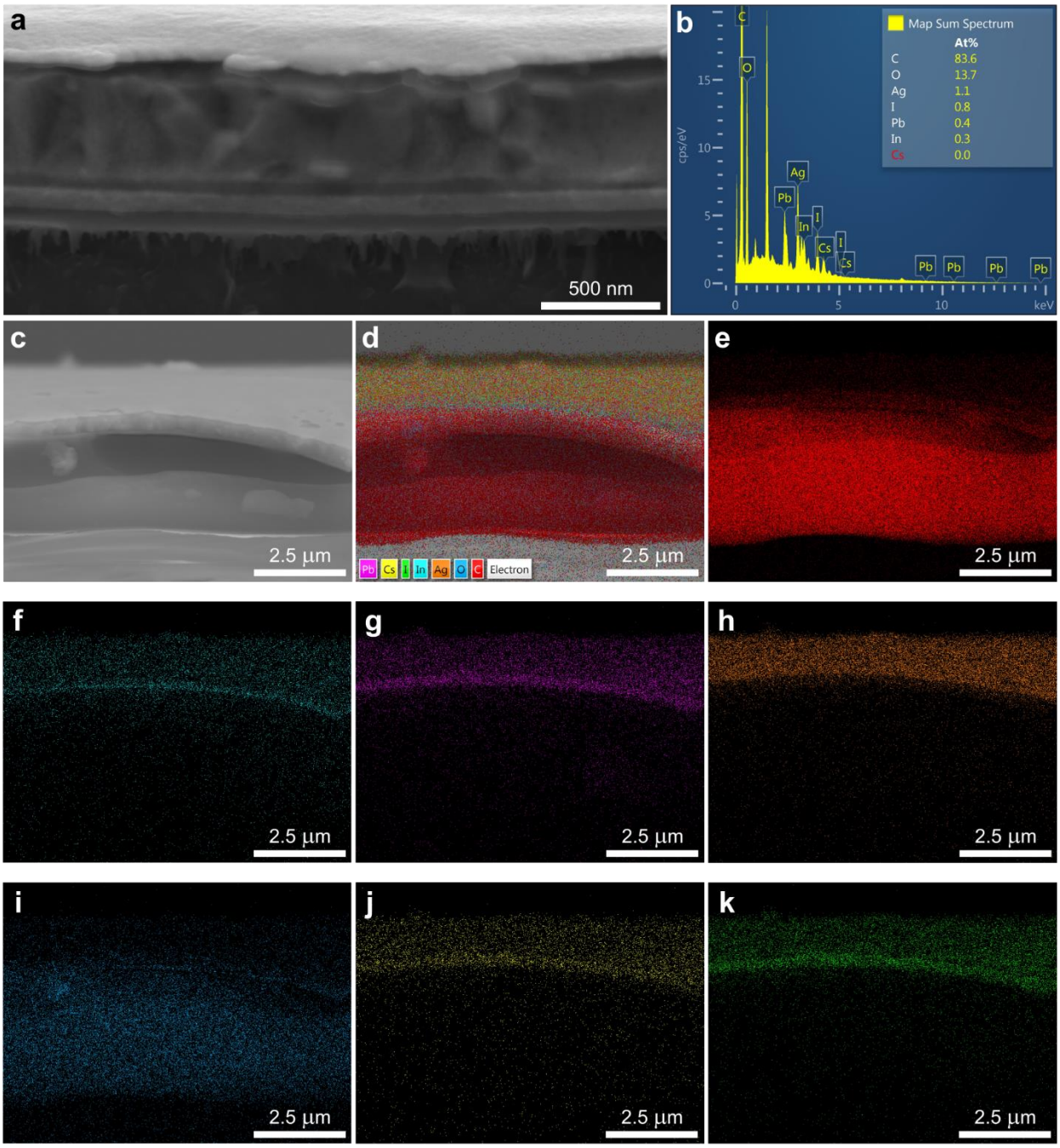

Supplementary Fig. 10 | Cross-section SEM images and energy-dispersive X-ray (EDX) elemental mapping of thin film perovskite solar cells. a, Close-up of the perovskite device layers, recorded at 5.0 kV beam intensity. **b**, EDX elemental spectrum corresponding to the area depicted in frame **c**. **d**-**k**, Overall (**d**), carbon (**e**), indium (**f**), lead (**g**), silver (**h**), oxygen (**i**), caesium (**j**) and iodine (**k**) elemental mapping. Frames **c**-**k** are recorded at a lower magnification, as the 15.0 kV beam intensity required for EDX analysis induces local heating, bending the thin PET plastic substrate.

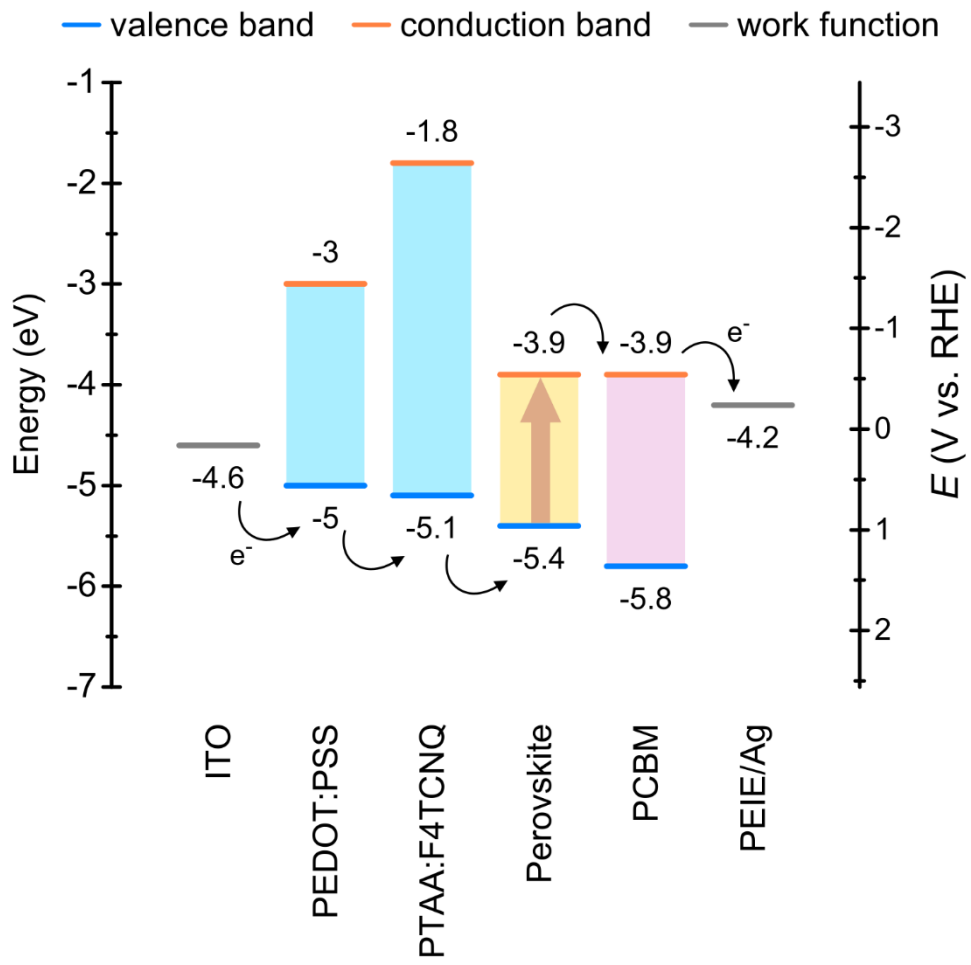

Supplementary Fig. 11 | Energy diagram of the perovskite PV device. The vacuum energy levels are gathered from reported literature.[20–23]

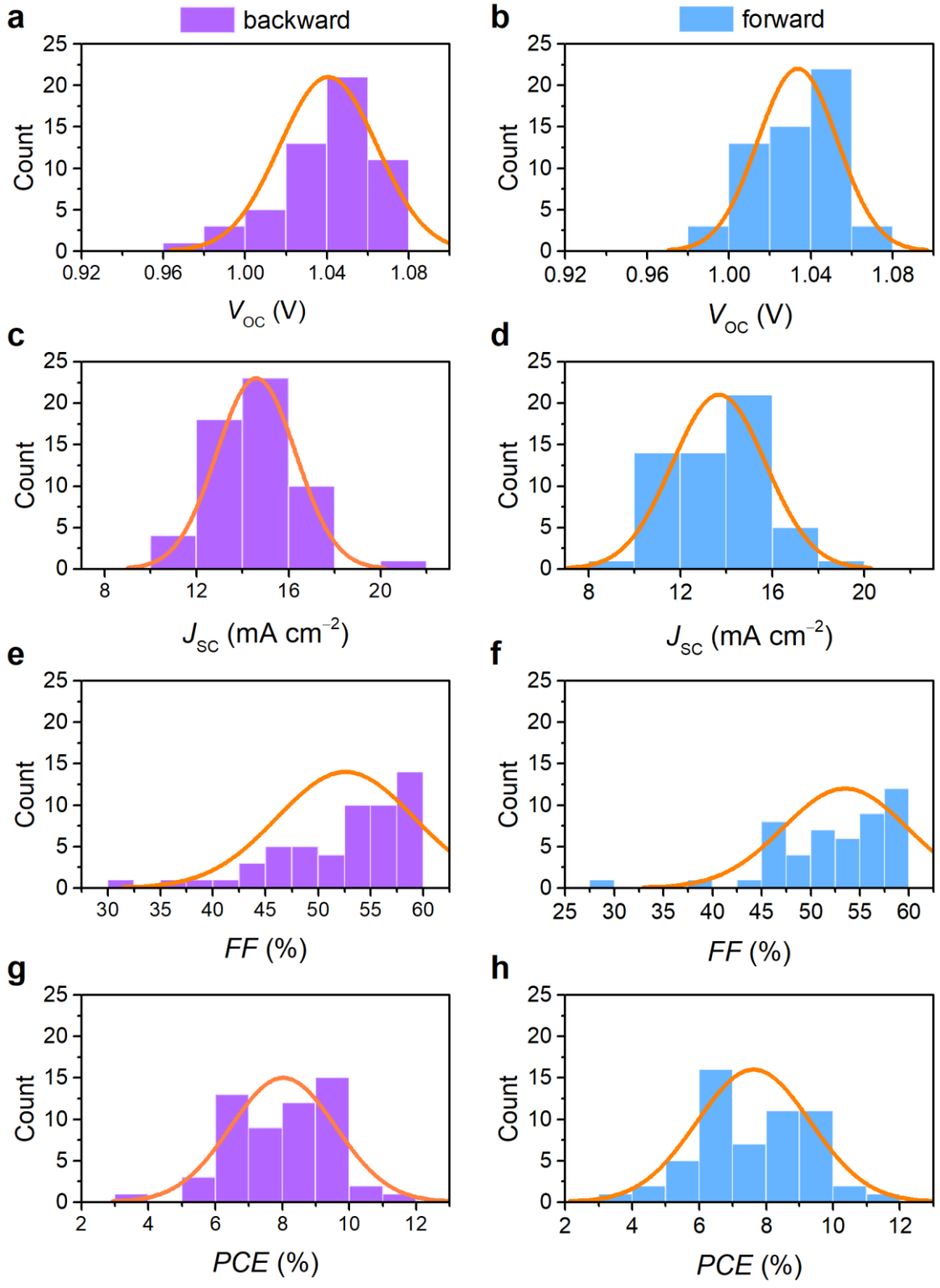

Supplementary Fig. 12 | Histograms showing the distribution in photovoltaic performance of the 56 flexible perovskite cells prepared for this work. a,**b**, Open circuit voltage (V_{OC}). **c**,**d**, Short circuit current density (J_{SC}). **e**,**f**, Fill factor (FF). **g**,**h**, Photovoltaic cell efficiency (PCE) (**a**,**c**,**e**,**g** - backward, **b**,**d**,**f**,**h** - forward scan direction, with normal distribution curves in orange). The average values amount to 1.04±0.02 V V_{OC}, −14.6±1.7 mA cm^{-2} J_{SC}, 52.6±6.5% FF, 8.0±1.6% PCE for the backward scans, and 1.03±0.02 V V_{OC}, −13.7±2.0 mA cm^{-2} J_{SC}, 53.5±6.3% FF, 7.6±1.7% PCE for the forward scans.

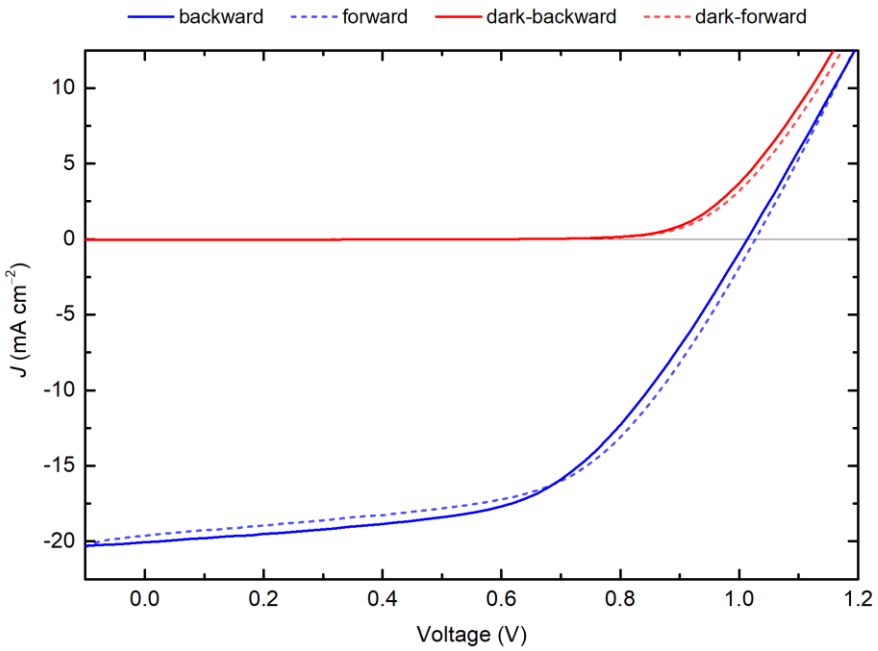

Supplementary Fig. 13 | Forward and backward *J-V* sweeps of the champion thin film perovskite device. The device shows 1.01 V V_{OC}, −20.1 mA cm^{-2} J_{SC}, 54.9% FF and 11.1% PCE in backward scan direction. A small hysteresis was observed between the forward and backward scans.

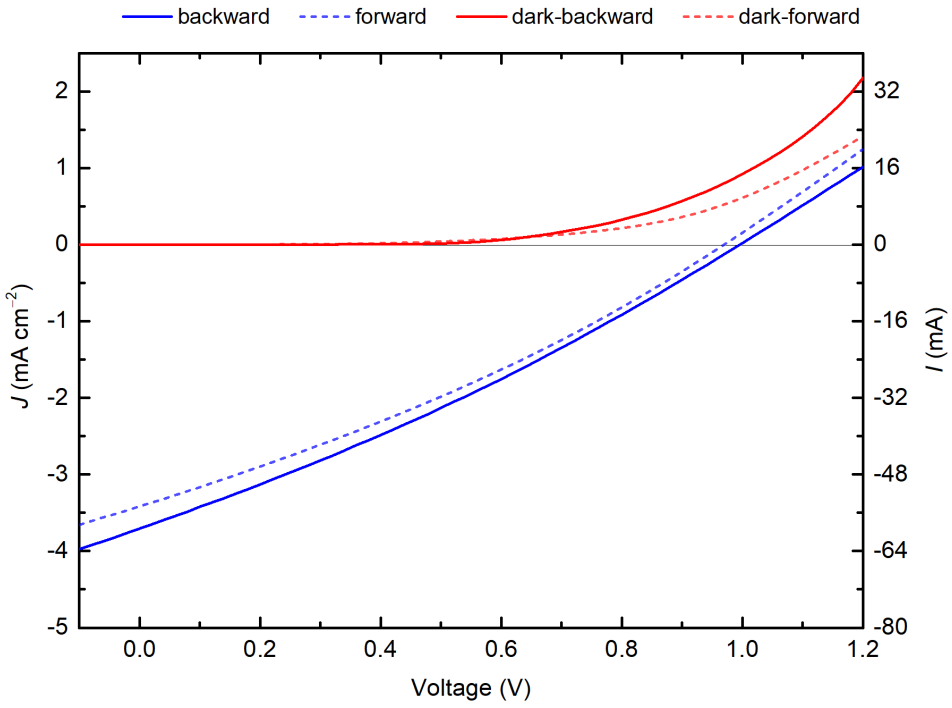

Supplementary Fig. 14 | Forward and backward *J-V* sweeps of the champion 16 cm^2 perovskite device. The device reached a 0.996 V V_{OC}, −3.71 mA cm^{-2} J_{SC}, 29.0% FF and 1.07% PCE in backward scan direction. The 6 up-scaled devices prepared in this study displayed average values of 0.99±0.02 V V_{OC}, −2.96±0.68 mA cm^{-2} J_{SC}, 28.5±1.6% FF, 0.84±0.21% PCE for the backward scans, and 0.98±0.02 V V_{OC}, −2.84±0.62 mA cm^{-2} J_{SC}, 29.1±1.7% FF, 0.81±0.20% PCE in forward scan direction.

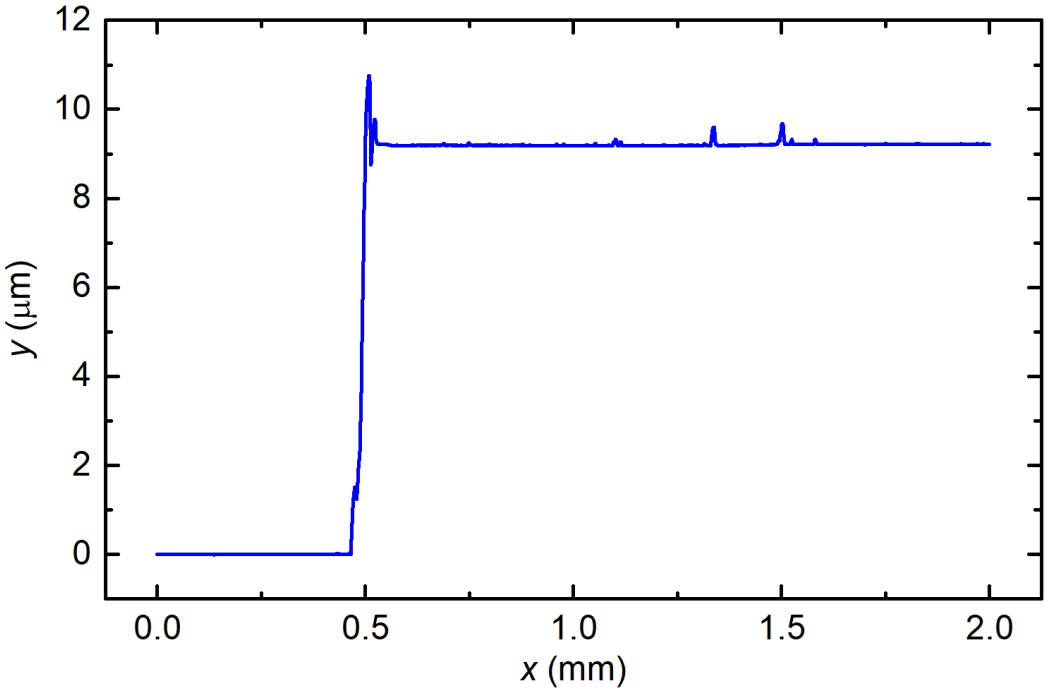

Supplementary Fig. 15 | Thickness profile of the parylene-C coating onto a glass substrate. The glass substrate is placed as reference along the perovskite samples in the reaction chamber. The thickness of the deposited film is subsequently determined using a profilometer (see Methods).

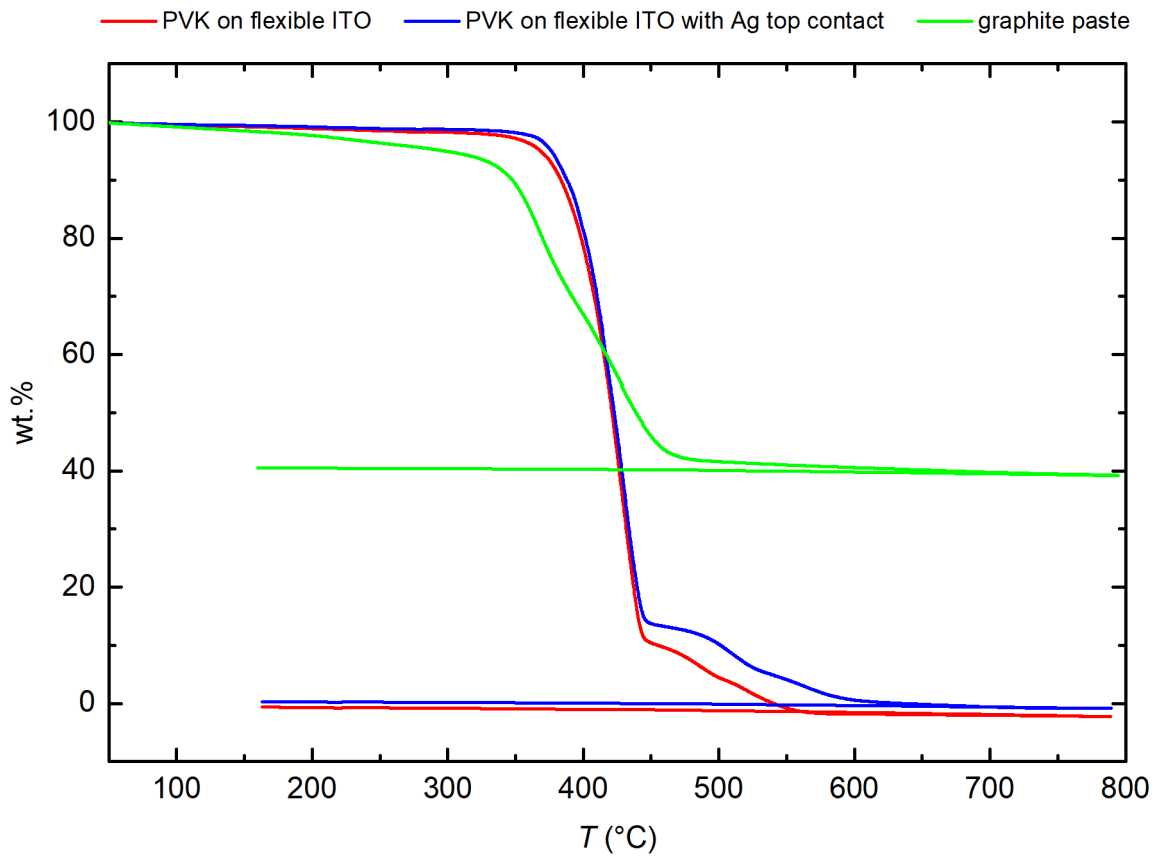

Supplementary Fig. 16 | Thermogravimetric analysis (TGA) of the perovskite lightweight device and corresponding graphite paste encapsulant. No substantial relative mass change occurs below 350°C for perovskite PV cells with, or without a Ag top contact. The 100 nm Ag contact accounts for the residual mass at higher temperatures (see difference between blue and red traces above 600°C, as the carbon support and device layers are combusted). A negligible loss in the relative mass of the graphite paste occurs below 150°C, whereas a graphitic amount of roughly 40% is maintained after heating the sample to 800°C, corresponding to the loss of the epoxy. Those observations, combined with reported data on the thermal stability of perovskite light absorbers,[24–27] indicate that the complete encapsulated device can withstand the temperatures of approximately 120°C which are temporarily achieved in the chemical vapor deposition (CVD) sample chamber during parylene-C deposition.

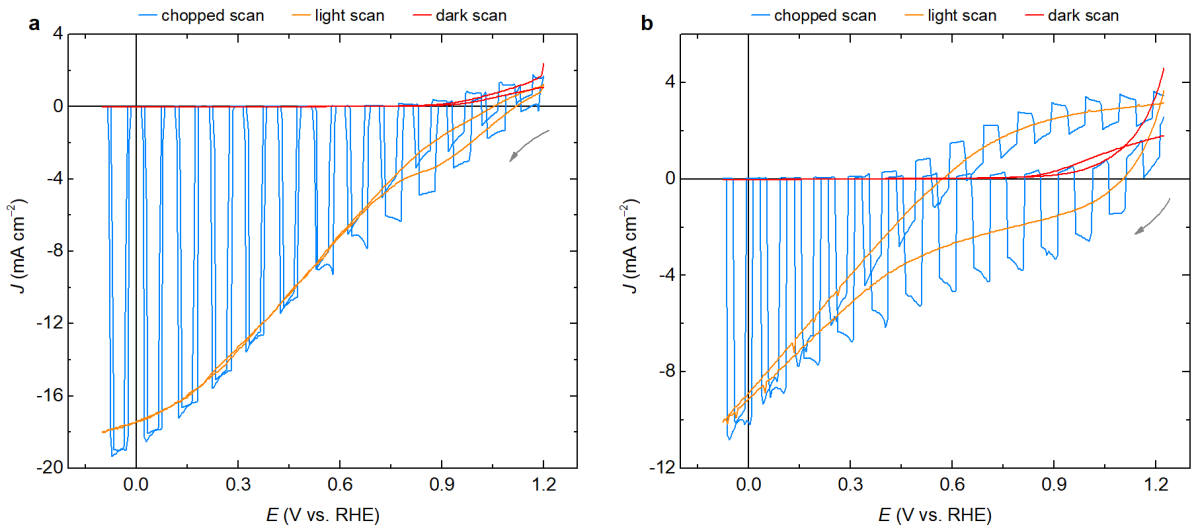

Supplementary Fig. 17 | CVs of the lightweight perovskite photocathodes with different catalysts. a, fPVK|GE|Pt for proton reduction. **b**, fPVK|GE|CoMTPP@CNT for syngas production. CVs are recorded under chopped, continuous, and no simulated solar light irradiation (AM1.5G, 100 mW cm^{-2}), at a 10 mV s^{-1} scan rate, in a 0.1 M KB_i, 0.1 M K_2SO_4 solution, pH 8.5, under N_2 for H_2 evolution, and in 0.5 M $KHCO_3$, under CO_2, pH 7.4 for CO_2 reduction.

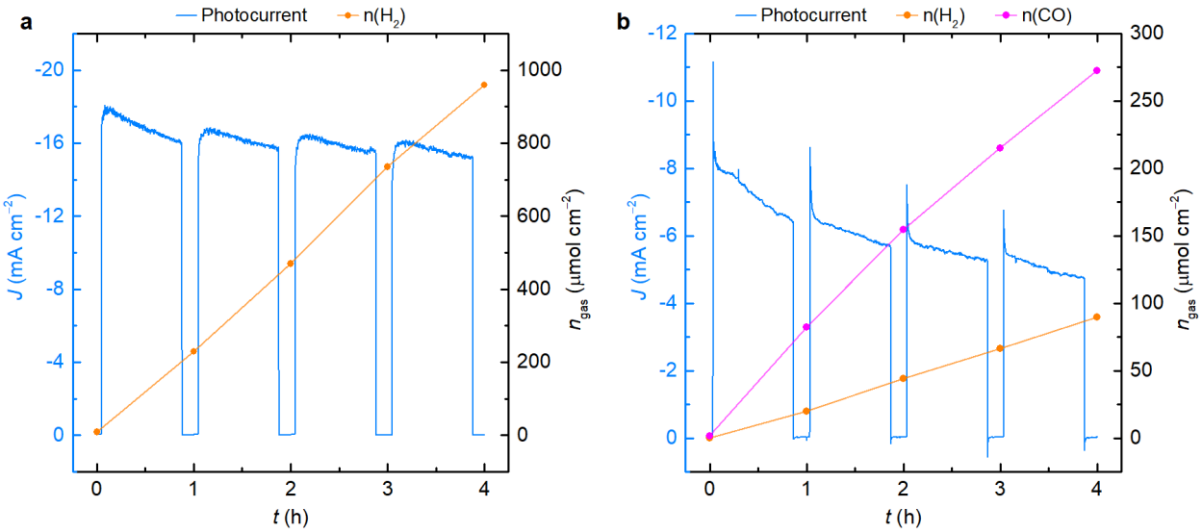

Supplementary Fig. 18 | Examples of 4 h CPE traces and corresponding product amounts for thin perovskite photocathodes with different catalysts. a, fPVK|GE|Pt for proton reduction. **b**, fPVK|GE|CoMTPP@CNT for syngas production. CPE is recorded under chopped irradiation (AM1.5G, 100 mW cm^{-2}, 50 min on - 10 min off), in a 0.1 M KB_i, 0.1 M K_2SO_4 solution, pH 8.5, under N_2 for H_2 evolution, and in 0.5 M $KHCO_3$, under CO_2, pH 7.4 for CO_2 reduction.

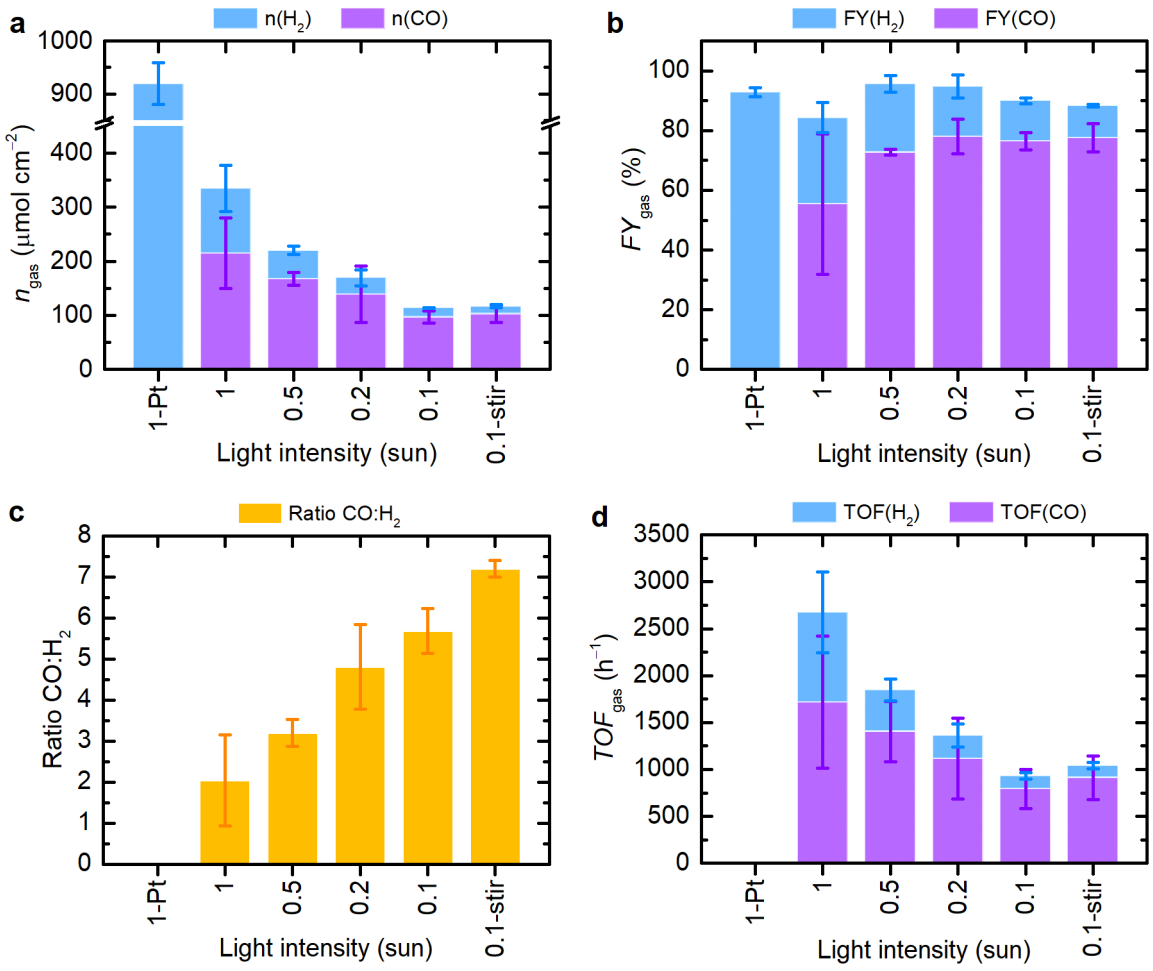

Supplementary Fig. 19 | Photoelectrochemical performance of fPVK|GE|CoMTPP@CNT photocathodes under varying light irradiation. a, Product amounts. **b**, Faradaic yields. **c**, CO:H_2 selectivity. **d**, Turnover frequency. A CO:H_2 ratio as high as 7.2:1 can be obtained by decreasing the light intensity to 0.1 sun, under stirring of the electrolyte solution. The results obtained from fPVK|GE|Pt photocathodes under 1 sun irradiation are also plotted for comparison. CPE is performed at 0 V vs. RHE for 4 h at room temperature, in a 0.5 M $KHCO_3$ electrolyte under CO_2 for syngas production, and in 0.1 M KB_i, 0.1 M K_2SO_4 solution, pH 8.5, under N_2 for H_2 evolution.

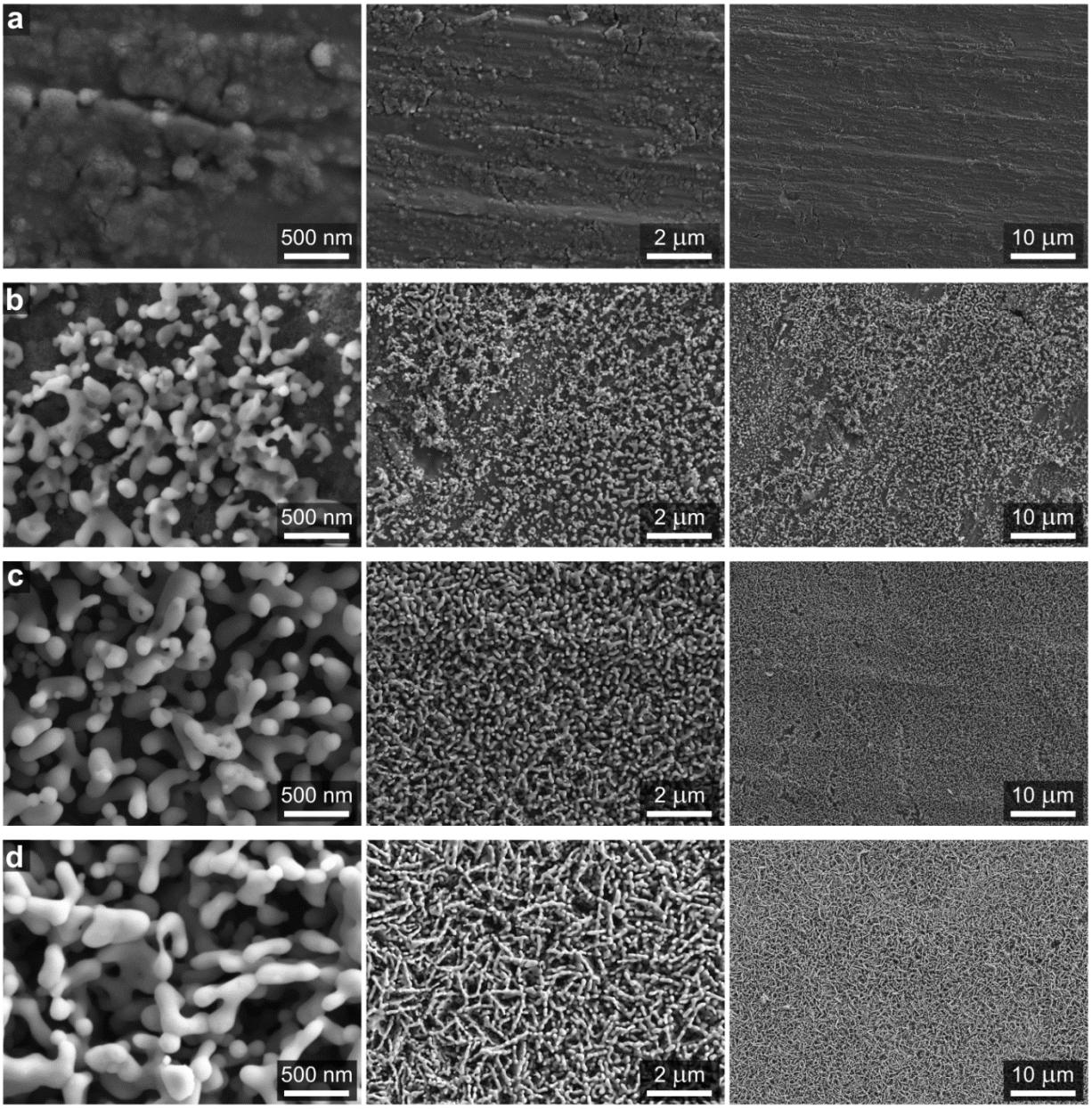

Supplementary Fig. 20 | Surface morphology of $BiVO_4$ photoanodes depending on the BiOI electrodeposition time. a, Ti foil indicates the presence of a TiO_2 layer, which is confirmed by EDX and XRD (Supplementary Figs. 21,25). **b**-**d**, $BiVO_4$ electrodes obtained from BiOI electrodeposited for: **b** - 0.5 min, **c** - 3 min, **d** - 10 min. The growth of small $BiVO_4$ grains and an incomplete film coverage is observed at short BiOI electrodeposition times, corresponding to a lower light absorption (**b**). The $BiVO_4$ nanostructures begin merging into triangular-oriented plates for longer BiOI electrodeposition times, diminishing the active surface area (**d** and Supplementary Fig. 23). A compromise between optimal surface coverage and porosity is obtained for the 3 min BiOI electrodeposition, yielding the highest photocurrents (Supplementary Fig. 27). The resulting worm-like structures resemble the morphology of FTO-deposited $BiVO_4$.[28]

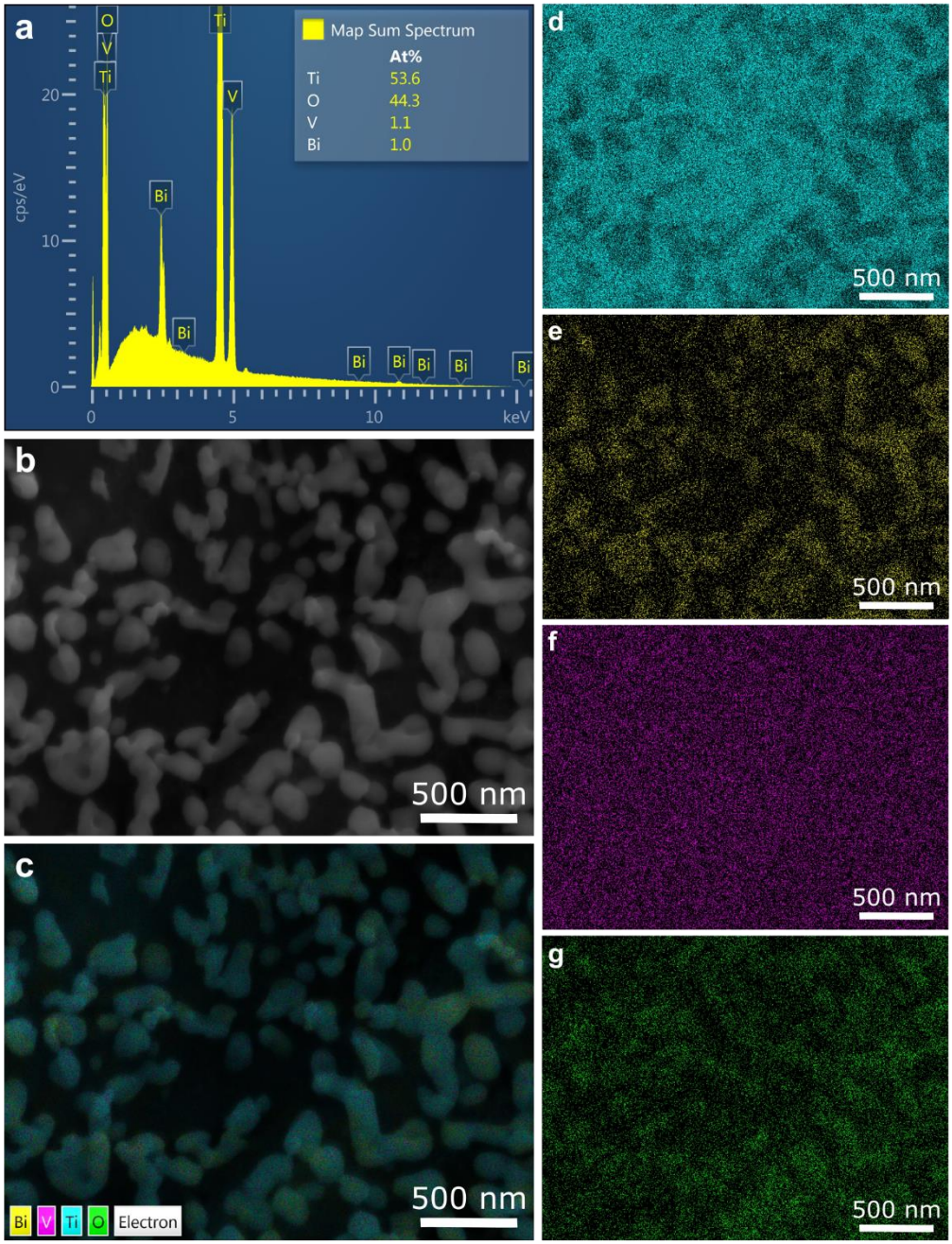

Supplementary Fig. 21 | EDX elemental mapping of $BiVO_4$ prepared from 0.5 min electrodeposited BiOI. **a**, EDX spectrum. **b**, SEM image of the scan area. **c**-**g**, Overall (**c**), titanium (**d**), bismuth (**e**), vanadium (**f**) and oxygen (**g**) elemental mapping.

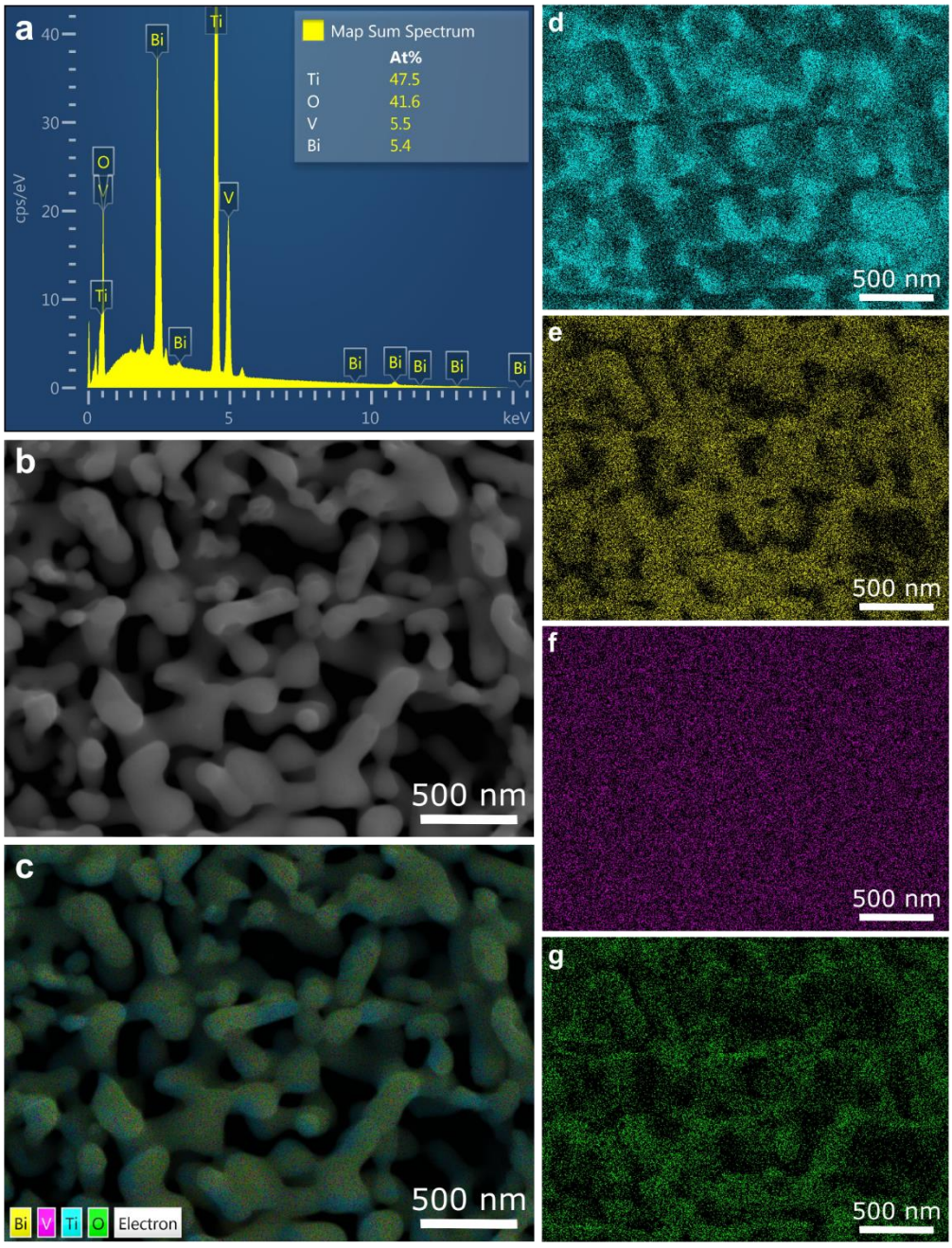

Supplementary Fig. 22 | EDX elemental mapping of $BiVO_4$ obtained from BiOI electrodeposited for 3 min. a, EDX spectrum. **b**, SEM image of the scan area. **c**-**g**, Overall (**c**), titanium (**d**), bismuth (**e**), vanadium (**f**) and oxygen (**g**) elemental mapping.

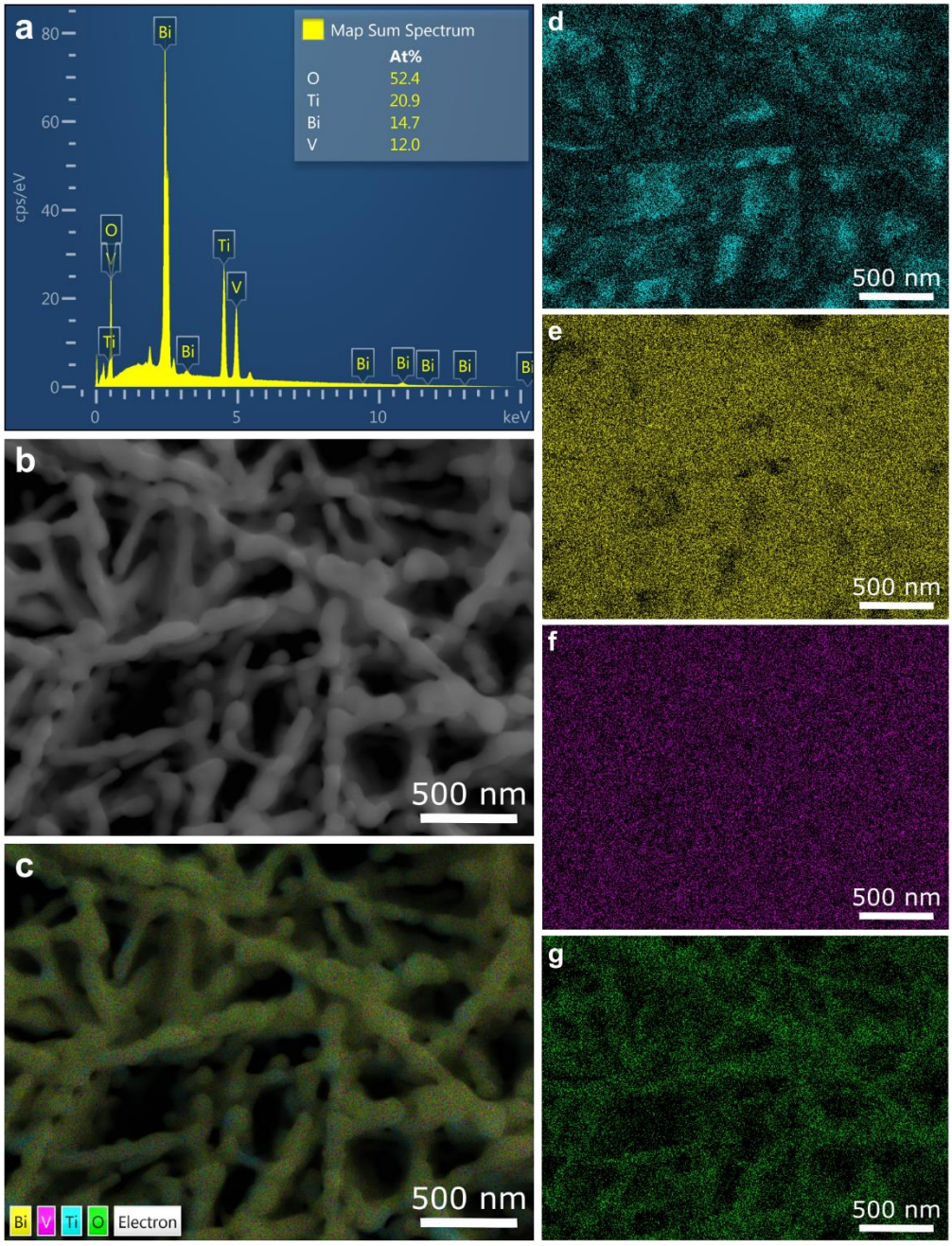

Supplementary Fig. 23 | EDX elemental mapping of $BiVO_4$ prepared from 10 min electrodeposited BiOI. **a**, EDX spectrum. **b**, SEM image of the scan area. **c**-**g**, Overall (**c**), titanium (**d**), bismuth (**e**), vanadium (**f**) and oxygen (**g**) elemental mapping.

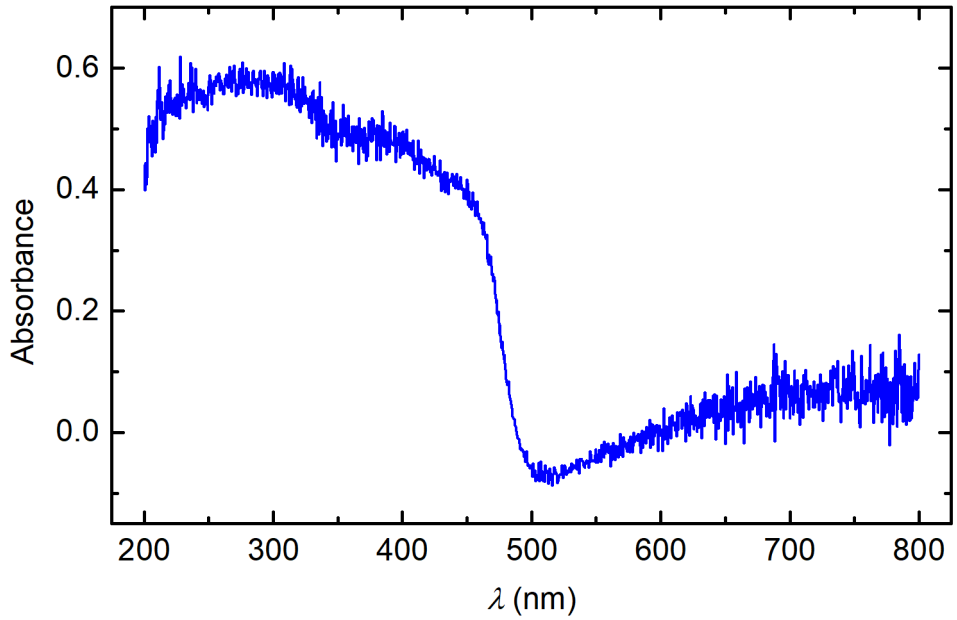

Supplementary Fig. 24 | UV-vis diffuse reflectance spectrum (DRS) of a Ti|$BiVO_4$ photoanode. A strong absorption is observed below 500 nm, which is assigned to $BiVO_4$.[28] A pristine Ti foil with a native TiO_2 layer is used as the reference for background subtraction.

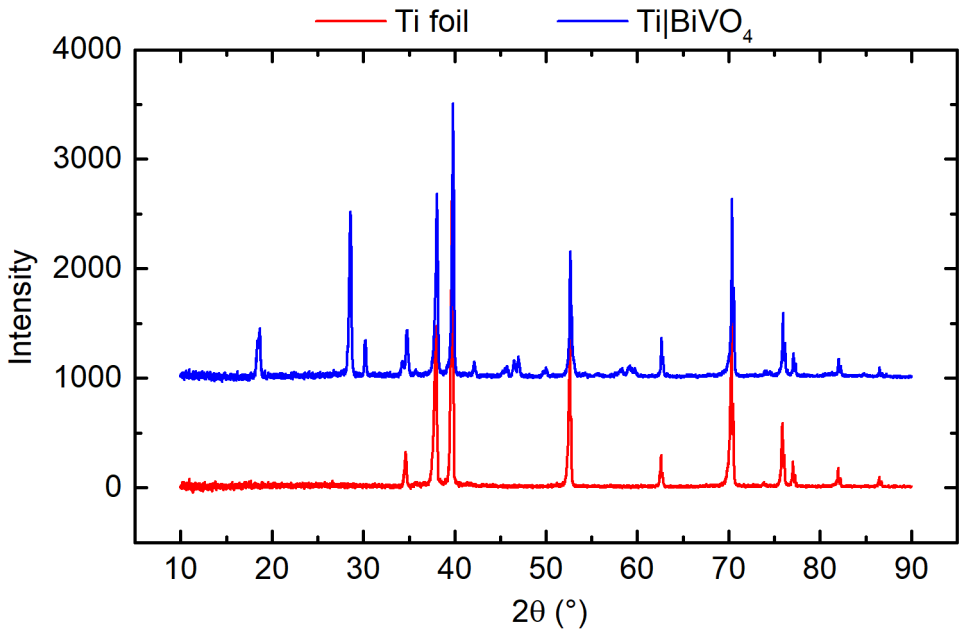

Supplementary Fig. 25 | X-ray powder diffraction (XRD) patterns of a Ti|$BiVO_4$ photoanode, and a pristine Ti foil as reference. The patterns confirm the presence of the $BiVO_4$ phase alongside a TiO_2 layer which likely forms during annealing onto the exposed Ti (see Supplementary Figs. 20b-d, 21). The pristine Ti foil presents the specific diffraction pattern of native TiO_2, a phase which is also visible from Supplementary Fig. 20a.

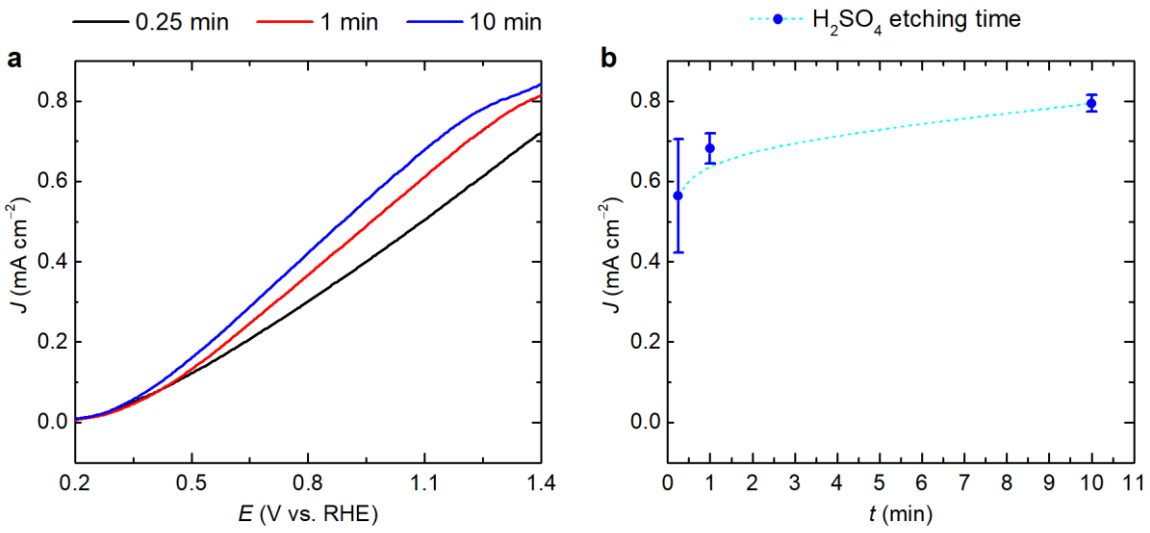

Supplementary Fig. 26 | Photocurrents of Ti|$BiVO_4$ electrodes prepared by submerging Ti foils in 95% H_2SO_4 for varying times. a, Examples of LSVs in forward scan direction under continuous light irradiation. **b**, Average photocurrent density at 1.23 V vs. RHE, extracted from the LSV scans (10 mV s^{-1} scan rate, 0.1 M KB_i, 0.1 M K_2SO_4 buffer, pH 8.5, under N_2, at room temperature). Only a slight increase in photocurrent is observed beyond 1 min of acid treatment, which indicates a fast removal of the native TiO_2 layer.

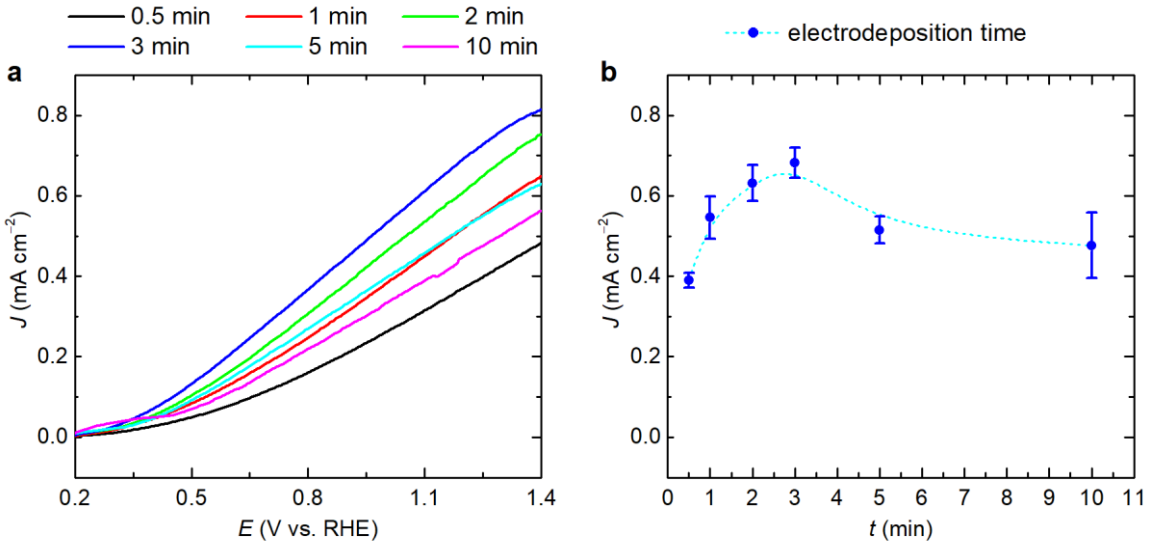

Supplementary Fig. 27 | Photocurrent response of the Ti|$BiVO_4$ photoanodes as a function of the BiOI electrodeposition time. a, Linear sweep voltammograms (LSVs) recorded in forward direction under continuous light irradiation for different electrodeposition times. **b**, Average photocurrent density at 1.23 V vs. RHE. The data points are calculated from triplicates of the LSV scans, and connected by a dotted visual guideline (10 mV s^{-1} scan rate, 0.1 M KB_i, 0.1 M K_2SO_4 buffer, pH 8.5, under N_2, at room temperature).

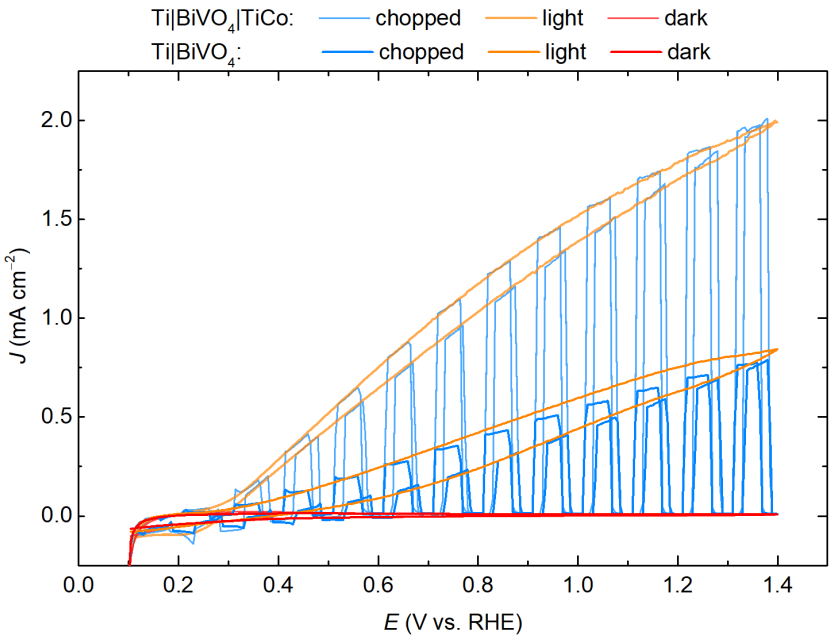

Supplementary Fig. 28 | Comparison between the photocurrents of a Ti|$BiVO_4$ photoanode with or without a TiCo O_2 evolution catalyst. CVs are recorded under chopped, continuous, and no simulated solar light irradiation (AM1.5G, 100 mW cm^{-2}, 10 mV s^{-1} scan rate, 0.1 M KB_i, 0.1 M K_2SO_4 buffer, pH 8.5, under N_2, at room temperature).

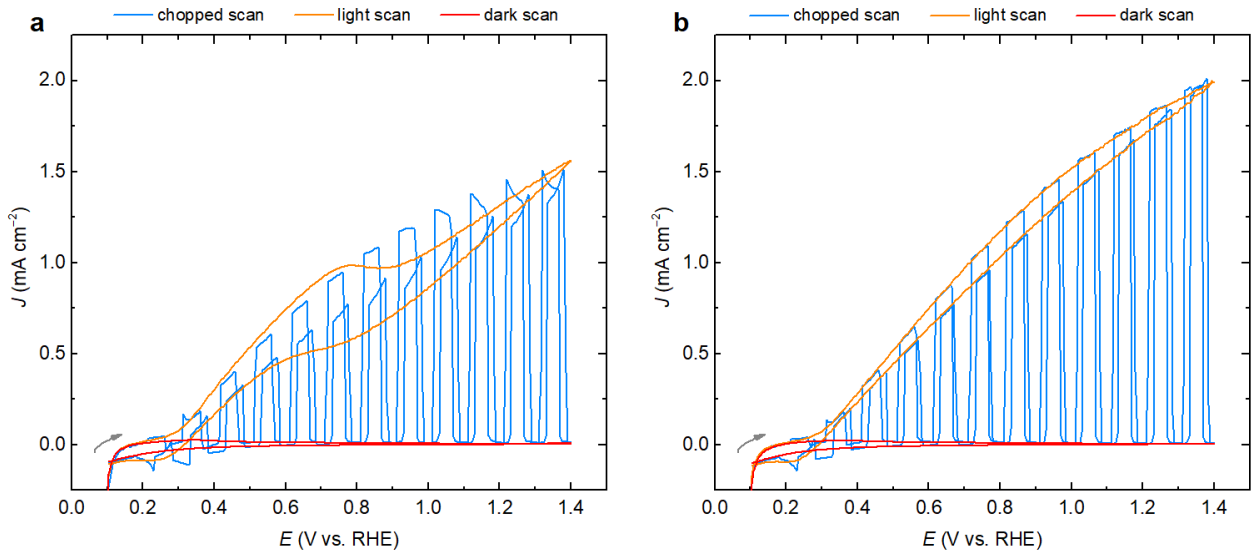

Supplementary Fig. 29 | Influence of stirring on the photocurrent of a Ti|$BiVO_4$|TiCo electrode. a, CVs without stirring. **b**, Photocurrents with solution stirring. CVs are recorded under chopped, continuous, and no simulated solar light irradiation (AM1.5G, 100 mW cm^{-2}, 10 mV s^{-1} scan rate, 0.1 M KB_i, 0.1 M K_2SO_4 buffer, pH 8.5, under N_2, at room temperature). The plots indicate the influence of transport limitations on the photocurrent, which corresponds to previous observations.[29,30]

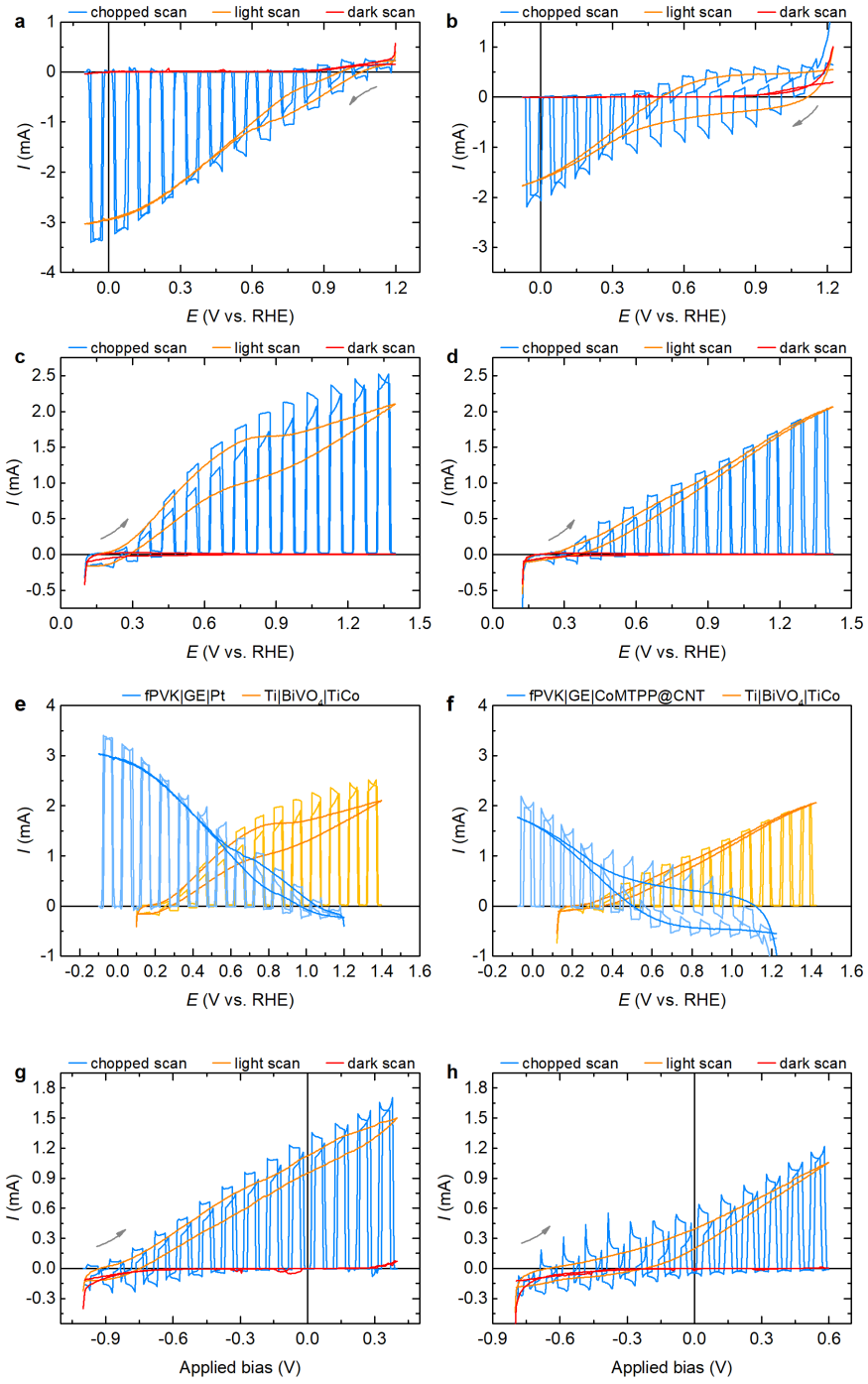

Supplementary Fig. 30 | Absolute photocurrents of wired lightweight perovskite-$BiVO_4$ tandems and of their corresponding photoelectrodes. a,**b**, CVs of perovskite photocathodes using Pt (**a**) and CoMTPP (**b**) catalysts under chopped, continuous, and no light irradiation. **c**,**d**, CVs of $BiVO_4$ photoanodes recorded in a 0.1 M KB_i, 0.1 M K_2SO_4 buffer (**c**) and a 0.5 M $KHCO_3$ solution (**d**). **e**,**f**, Overlap of the perovskite and $BiVO_4$ photocurrents (the sign of the perovskite photocurrent is inverted). **g**,**h**, CVs of the tandem devices. A Pt catalyst is employed in frames **a**,**e**,**g** for H_2 evolution, whereas CoMTPP@CNT is used in frames **b**,**f**,**h** for syngas production. As the perovskite photocathode is directly irradiated (i.e. no absorption or scattering losses are caused by a transparent $BiVO_4$ photoanode), frames **e**,**f** give a close estimate for the photocurrents obtained under bias-free conditions (**g**,**h**). The negative 0.4 V shift in the onset bias of PEC devices (**g**,**h**) over previous reports[1,30] can be traced back to the additional perovskite photovoltage gained by adding the PTAA layer (≈0.2 V) and using direct 1 sun irradiation (≈0.1 V[1]), combined with the ≈0.1 V earlier onset potential of Ti|$BiVO_4$|TiCo.

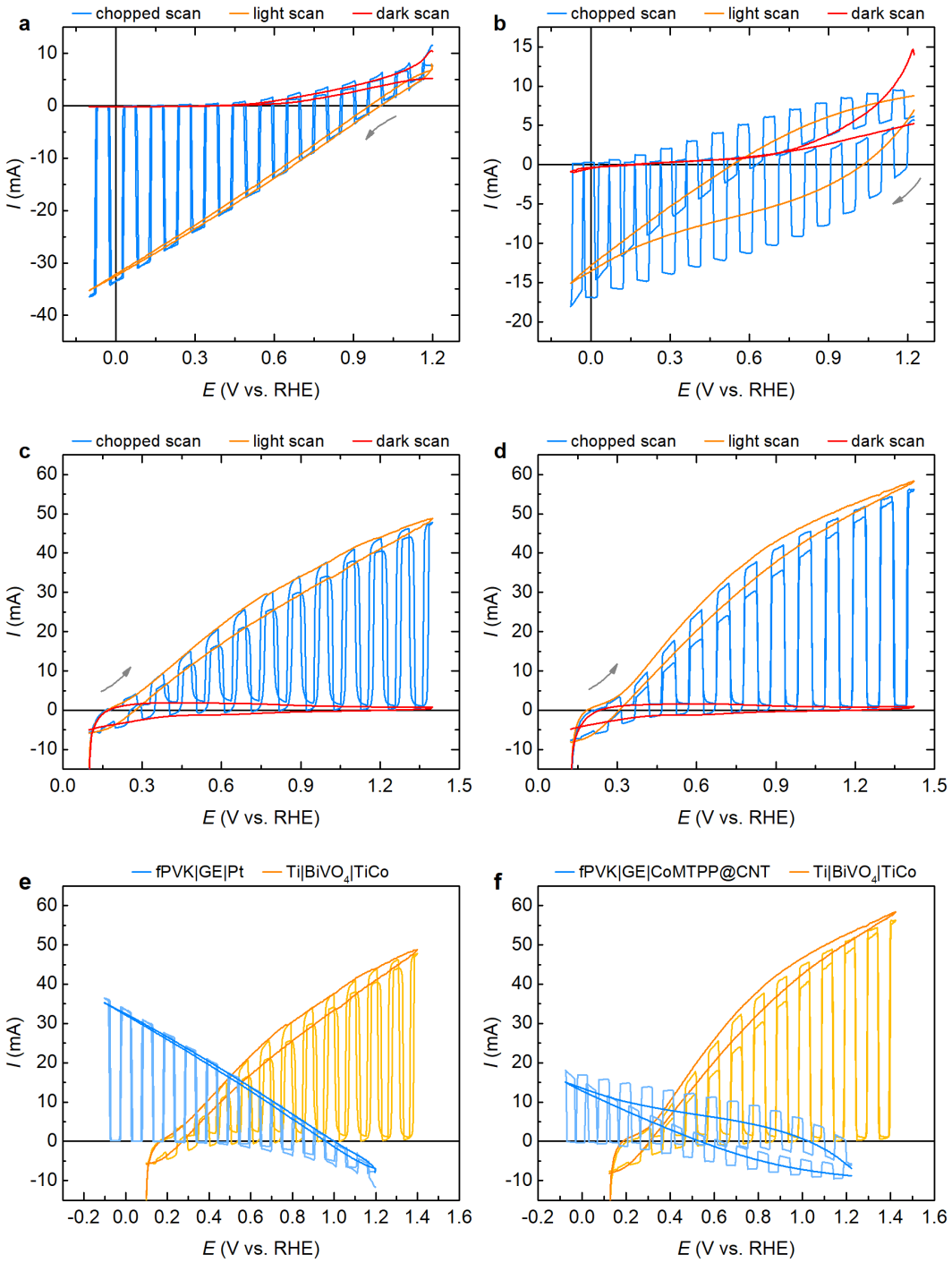

Supplementary Fig. 31 | Absolute photocurrents of up-scaled perovskite and $BiVO_4$ photoelectrodes. **a**,**b**, CVs of 16 cm^2 perovskite photocathodes using Pt (**a**) and CoMTPP (**b**) catalysts under chopped, continuous, and no light irradiation. **c**,**d**, CVs of an 84 cm^2 $BiVO_4$ photoanode recorded in a 0.1 M KB_i, 0.1 M K_2SO_4 buffer (**c**) and a 0.5 M $KHCO_3$ solution (**d**). **e**,**f**, Overlap of the perovskite and $BiVO_4$ photocurrents, indicating the ideal photocurrents obtained in case of the 100 cm^2 unassisted PEC devices (the sign of the photocathode signal is inverted).

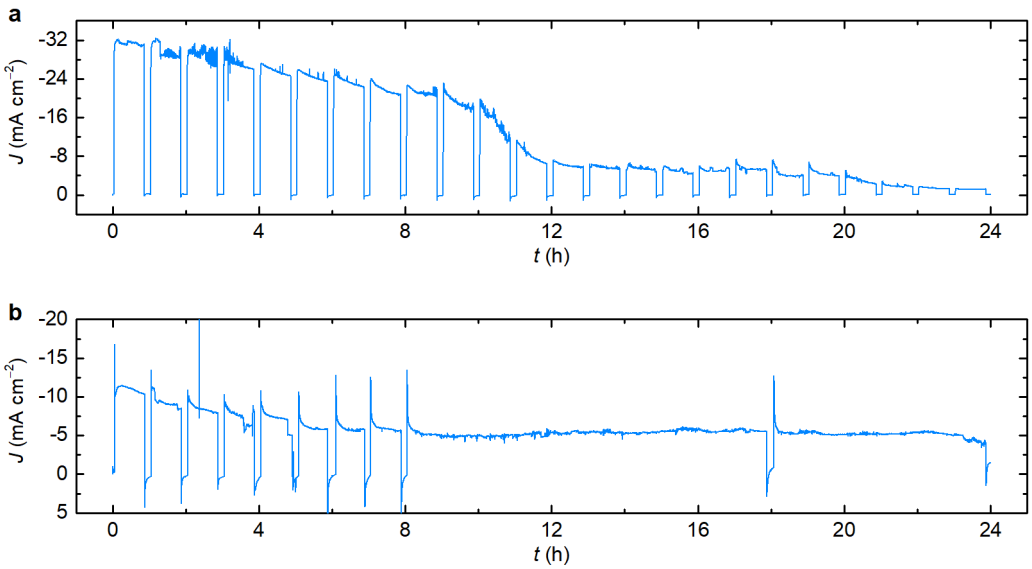

Supplementary Fig. 32 | Stability tests of 16 cm² perovskite photocathodes. a, fPVK|GE|Pt. **b**, fPVK|GE|CoMTPP@CNT. CPE is conducted at 0 V vs. RHE, revealing a similar stability of 12-24 h to the small-scale samples with 0.25 cm^2 active areas.

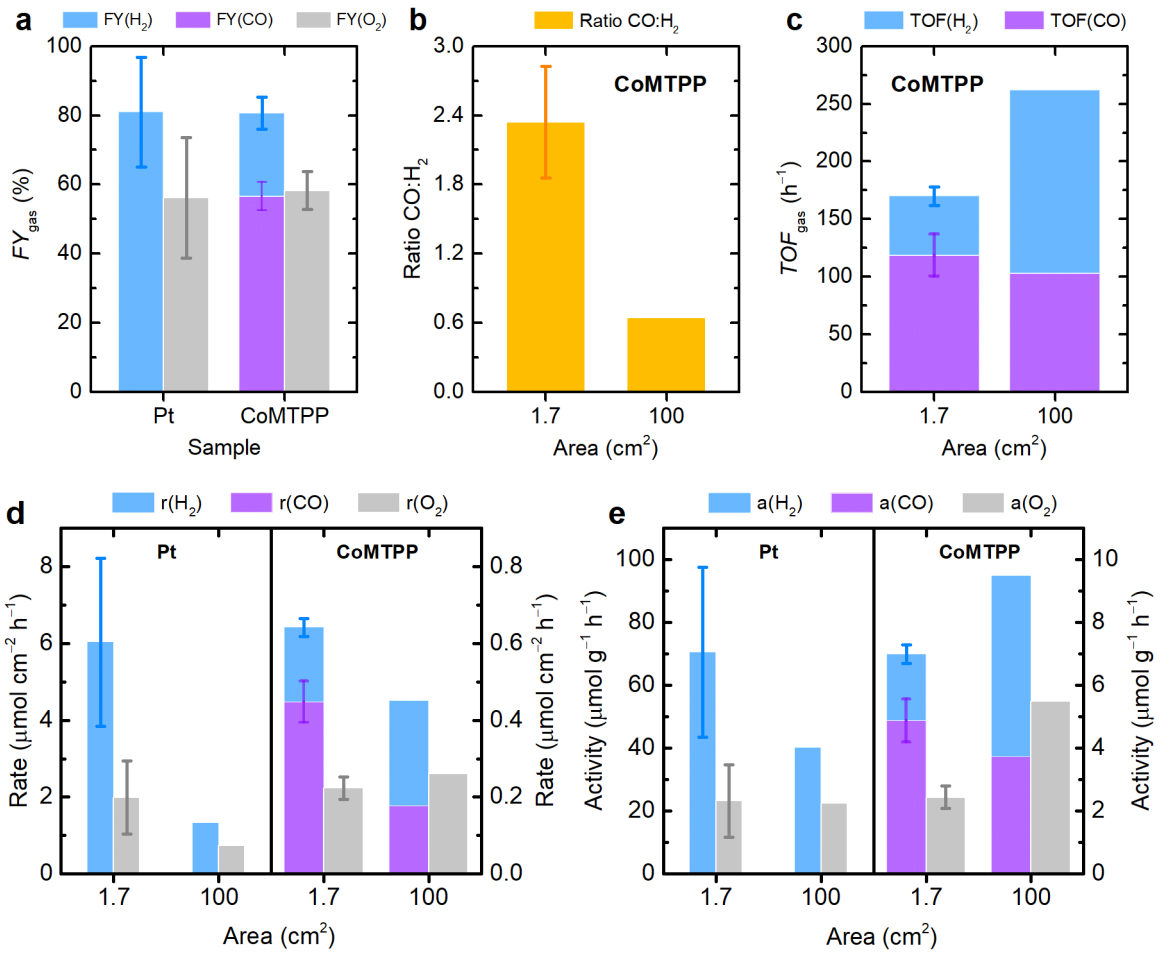

Supplementary Fig. 33 | Photoelectrochemical performance of bias-free perovskite-$BiVO_4$ devices. a, Faradaic yields of the small-scale, wired samples. **b**, CO:H_2 selectivity of devices with a CoMTPP catalyst for CO_2 reduction. **c**, Turnover frequency of the corresponding samples. **d**, Product rates of small- and large-scale PEC devices for water splitting ("Pt" - left side), or syngas production and water oxidation ("CoMTPP" - right). **e**, Activity per gram of the corresponding samples. Values are averaged over 10 h CPE for the wired 1.7 cm^2 samples, and over 18 h for the wireless 100 cm^2 devices. While larger samples display lower product rates than the 1.7 cm^2 devices, their activities remain similar due to the relatively lower mass per area of 100 cm^2 leaves. In their case, the photocathode does not cover the entire back side of the Ti foil, resulting in a mass reduction (see Supplementary Figs. 38, 39). Faradaic yields of small-scale devices amount to around 80% (for H_2 or syngas) and 60% (O_2). Such deviations in the FYs are commonly encountered in one-compartment PEC reactors due to dissolved gases, bubble trapping, or O_2 reduction. A 20% loss in the faradaic yields of H_2 and O_2 is mainly due to O_2 reduction on the cathodic side, which competes with proton reduction. A further decrease in the O_2 faradaic yield can be traced back to water droplets condensing on the tip of the fluorescence O_2 sensor during operation. These droplets cause an apparent decrease in the amount of O_2 and an increase in the signal noise after the first 4-8 h for both small- and large-scale devices (see Fig. 3c,d from the main text).

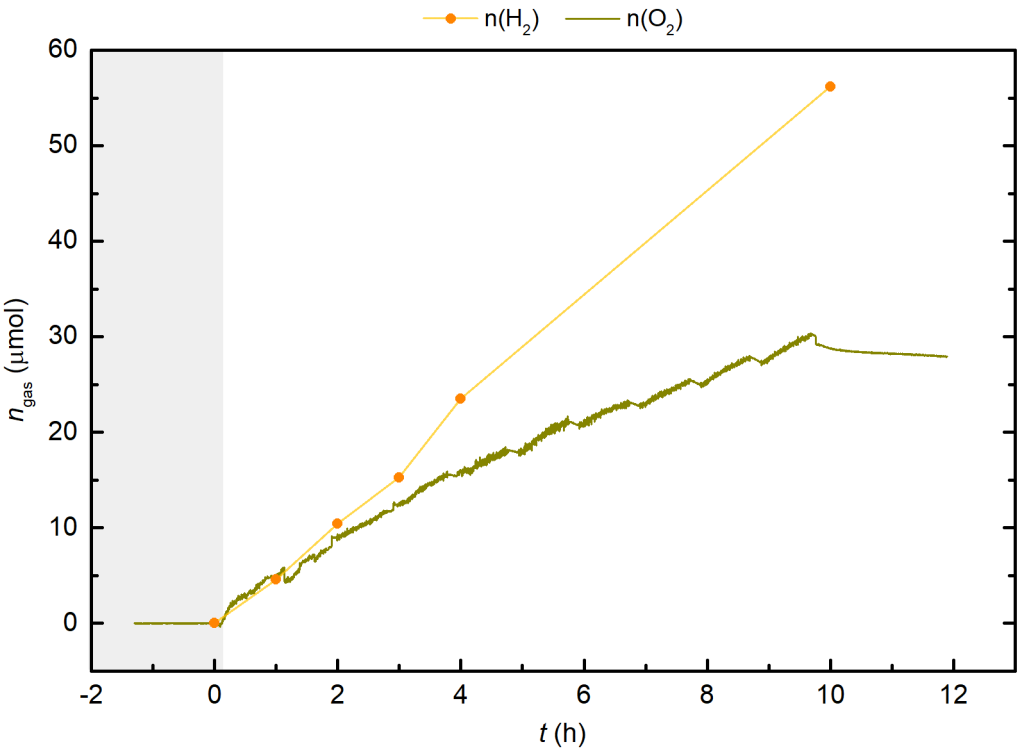

Supplementary Fig. 34 | Demonstration of unassisted water splitting using a lightweight wireless perovskite-$BiVO_4$ PEC device. A higher relative amount of O_2 is detected over the first few hours, as oxygen can easily diffuse from the thin layer of solution in case of floating devices, whereas the reduction products are trapped below the device, enabling flotation (see Supplementary Figs. 40,42). After a prolonged period (e.g. 10 h), the amounts of products in the head space of the reactor equilibrate, resulting in an approximately 2:1 ratio of H_2:O_2. The rates of H_2 and O_2 production are ≈25% lower than those of wired, vertically oriented leaves (Supplementary Fig. 33). This may be due to light scattering and coverage of the active areas by bubbles, or by a partial drying of the photoanode surface (see Supplementary Figs. 40,42). However, natural wave movement enabled the $BiVO_4$ and catalyst surfaces to remain moist during outdoor tests (Supplementary Fig. 46).

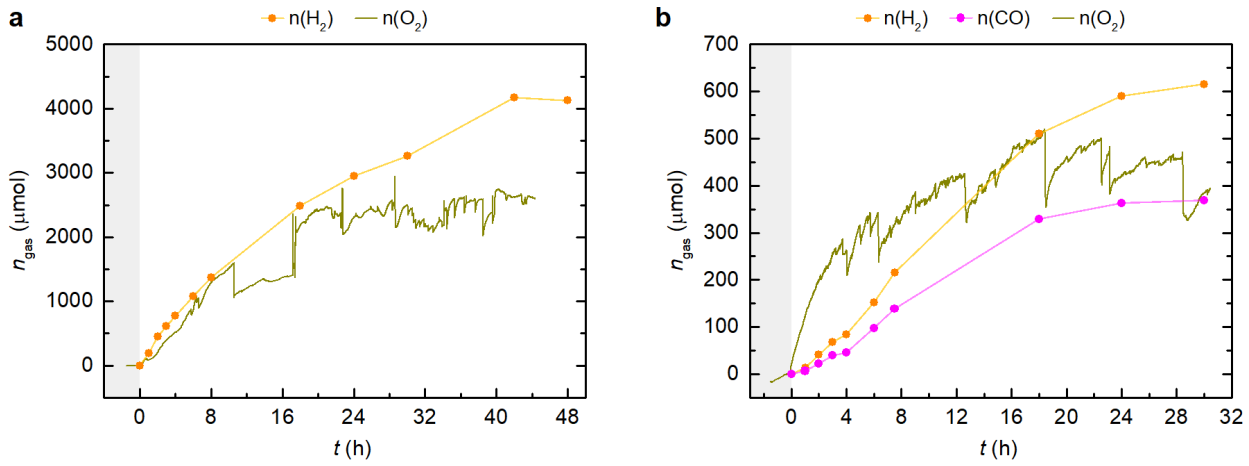

Supplementary Fig. 35 | Amounts of gases produced by the 100 cm² wireless perovskite-$BiVO_4$ PEC devices. **a**, Ti|$BiVO_4$|TiCo – fPVK|GE|Pt artificial leaf for water splitting. **b**, Ti|$BiVO_4$|TiCo – fPVK|GE|CoMTPP@CNT device coupling syngas production with water oxidation. Higher amounts of O_2 are detected during the first few hours, as explained in the caption of Supplementary Fig. 34. Later, a noisy O_2 evolution trace is caused by water droplets forming on the tip of the fluorescence oxygen sensor.

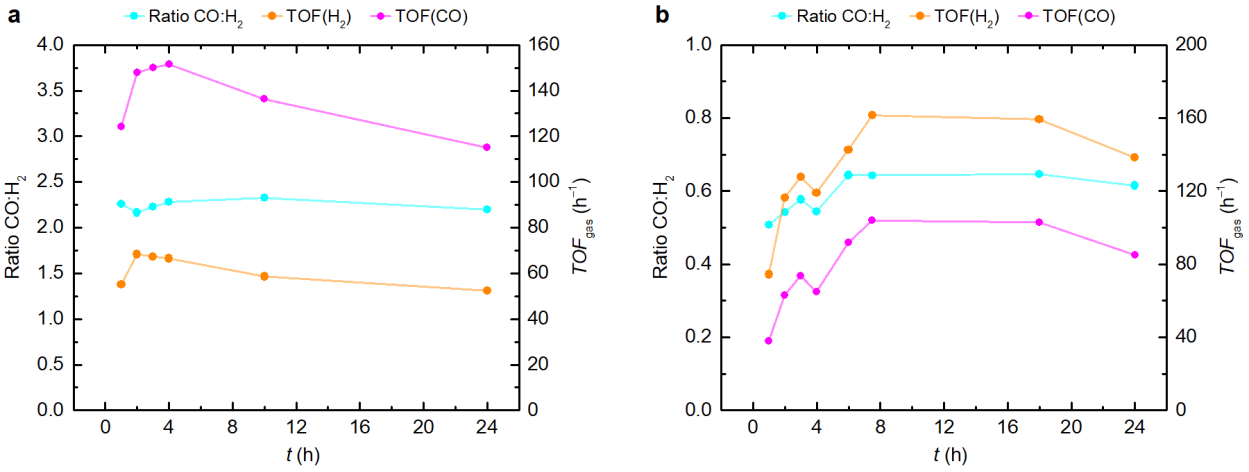

Supplementary Fig. 36 | Time-dependant CO:H_2 selectivity and turnover frequency for PEC devices of different sizes. **a**, Wired 1.7 cm² device. **b**, Wireless 100 cm² artificial leaf. The selectivity and TOF remain relatively constant throughout both experiments. The lower selectivity of the 100 cm² device can be assigned to the cathodic shift in the overlap between the perovskite and $BiVO_4$ photocurrents (Fig. 3a,b, main text). This indicates that the CoMTPP catalyst operates at a more negative potential in case of the larger device, resulting in a higher H_2 production rate (see Supplementary Figs. 5, 33).

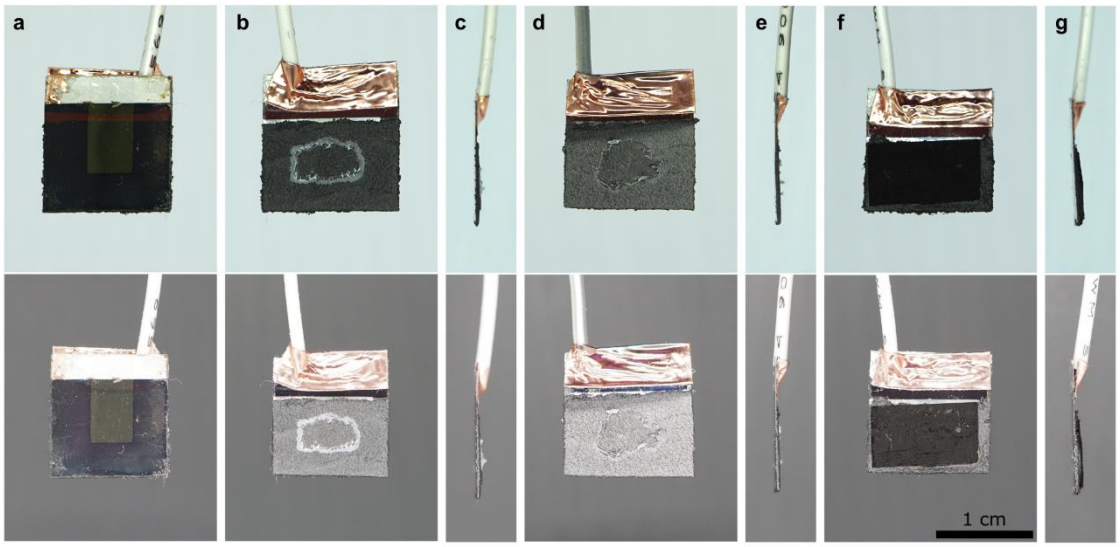

Supplementary Fig. 37 | Photographs of the thin perovskite photocathodes. a, View through the PET-ITO substrate. **b**, Encapsulated fPVK|GE photocathode without catalyst. The central area consists of exposed graphite epoxy, which is not covered by a parylene-C coating. **c**, Side view of a fPVK|GE photocathode. **d**, fPVK|GE|Pt electrode. **e**, Side view of the fPVK|GE|Pt electrode. **f**, fPVK|GE|CoMTPP@CNT. **g**, Side view of the fPVK|GE|CoMTPP@CNT. Samples are photographed on white (top row) and dark (below) backgrounds, to mitigate the high contrast.

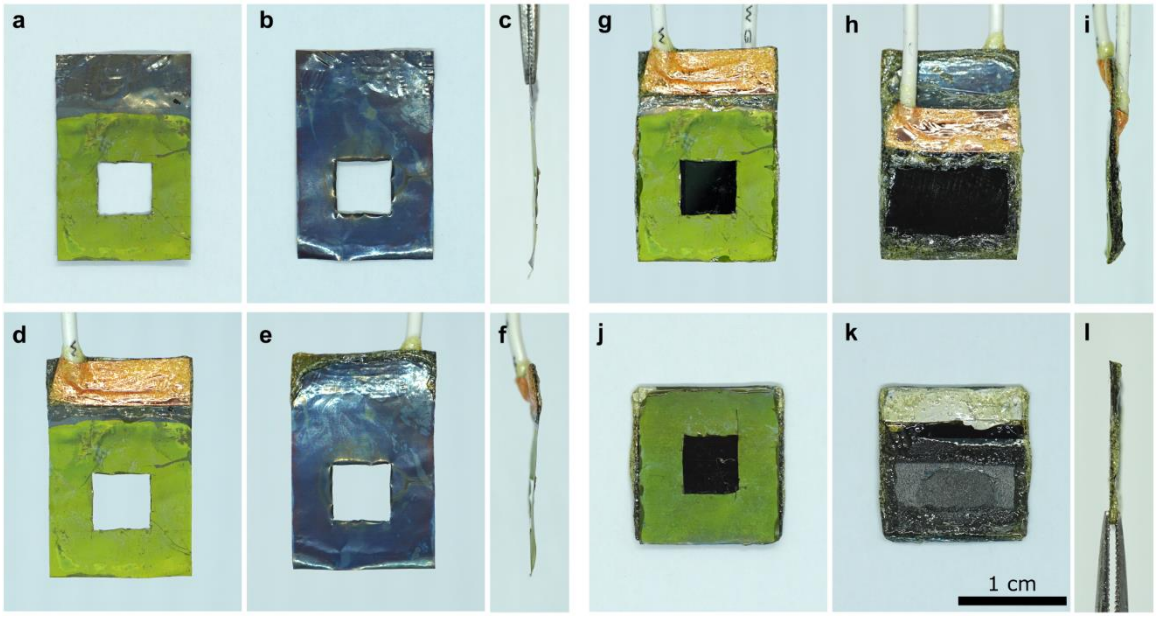

Supplementary Fig. 38 | Photographs of thin Ti|$BiVO_4$|TiCo photoanodes and perovskite-$BiVO_4$ PEC devices. a-**c**, Bare Ti|$BiVO_4$|TiCo photoanode. **d**-**f**, Wired Ti|$BiVO_4$|TiCo photoanode. **g**-**i**, Wired Ti|$BiVO_4$|TiCo – fPVK|GE|CoMTPP@CNT PEC device. **j**-**l**, Standalone Ti|$BiVO_4$|TiCo – fPVK|GE|Pt artificial leaf. **a**,**d**,**g**,**j**, Front views. **b**,**e**,**h**,**k**, Back views. **c**,**f**,**i**,**l**, Side views.

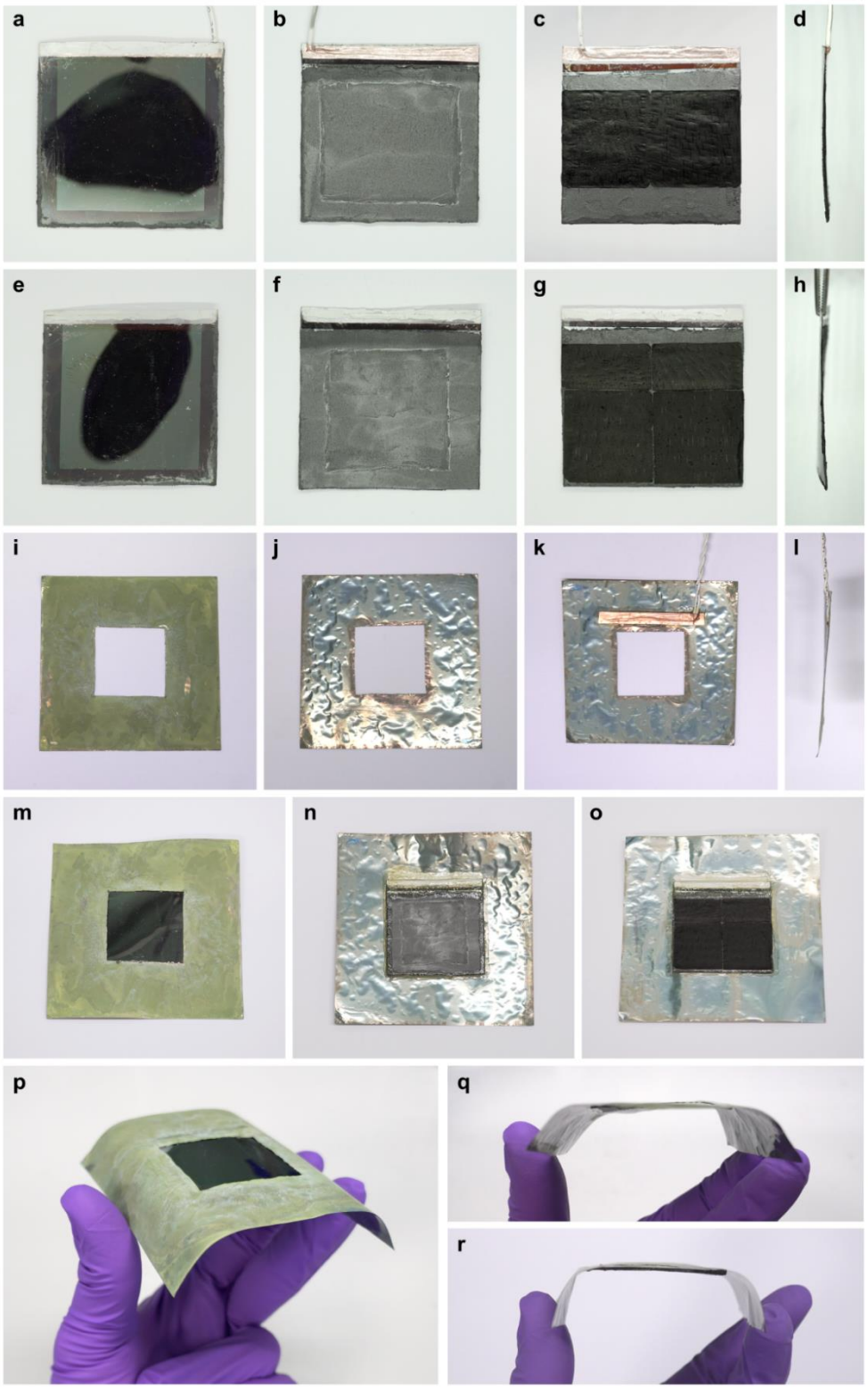

Supplementary Fig. 39 | Photographs of up-scaled perovskite photocathodes, $BiVO_4$ photoanodes and standalone PEC devices. a-**d**, Wired perovskite photocathodes (16 cm^2 active area, 25 cm^2 total substrate area). **e**-**h**, Wireless perovskite photocathodes for the standalone leaves. **i**,**j**, Bare Ti|$BiVO_4$|TiCo photoanode, (100 – 16) cm^2 active area. **k**,**l**, Wired Ti|$BiVO_4$|TiCo photoanode. **m**-**r**, Standalone artificial leaves. **a**,**e**,**i**,**m**, Front views. **b**,**c**,**f**,**g**,**j**,**k**,**n**,**o**, Back views. **d**,**h**,**l**,**q**,**r**, Side views. **b**,**f**,**n**,**q**, Employing a Pt H_2 evolution catalyst. **c**,**g**,**o**,**r**, Employing a CoMTPP@CNT CO_2 reduction catalyst.

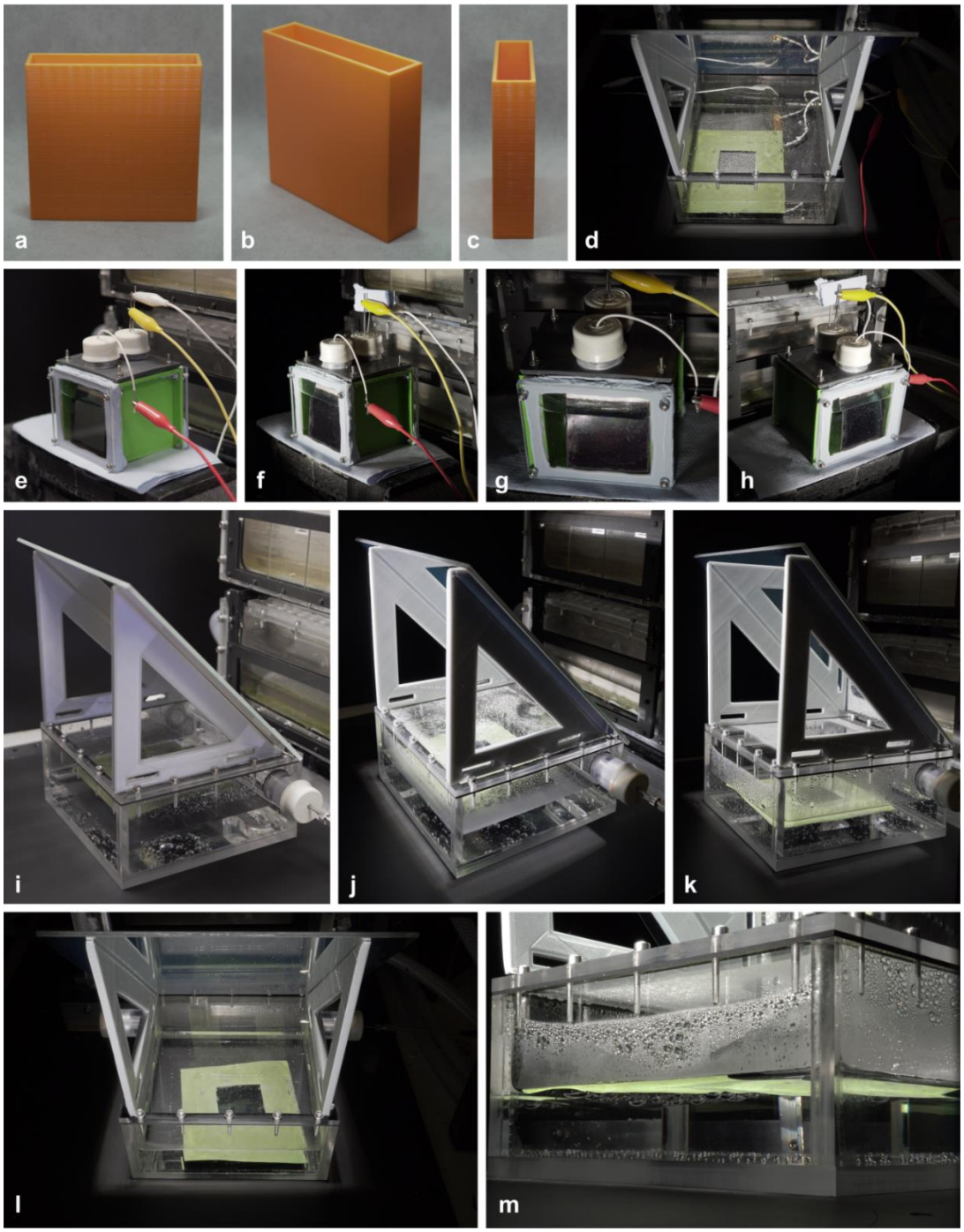

Supplementary Fig. 40 | Photographs of the reactors developed to prepare and characterise the up-scaled samples. a-**c**, 3D-printed chamber developed for the electrodeposition of BiOI on 10×10 cm^2 conductive substrates. **d**, PEC characterisation of the $BiVO_4$ photoanode in a three-electrode, one-compartment configuration. A transparent polymethyl methacrylate panel is placed as a spacer between the photoanode and the graphite foil counter electrode. **e**-**h**, A fPVK|GE|Pt photocathode is characterised inside a one-compartment 3D-printed reactor.[24] **i**-**m**, Photographs of the setup constructed for the scalable artificial leaves. Due to the low density of CNT sheets, trapped gasses and bubbles caused by CO_2 saturation, the device with a CoMTPP@CNT catalyst is floating even before irradiation (see CNT reflection in **i**,**j**). On the other side, the water splitting leaf is not floating at the beginning of the experiment (**l**), and only achieves buoyancy after H_2 bubbles are accumulating underneath (**k**,**m**).

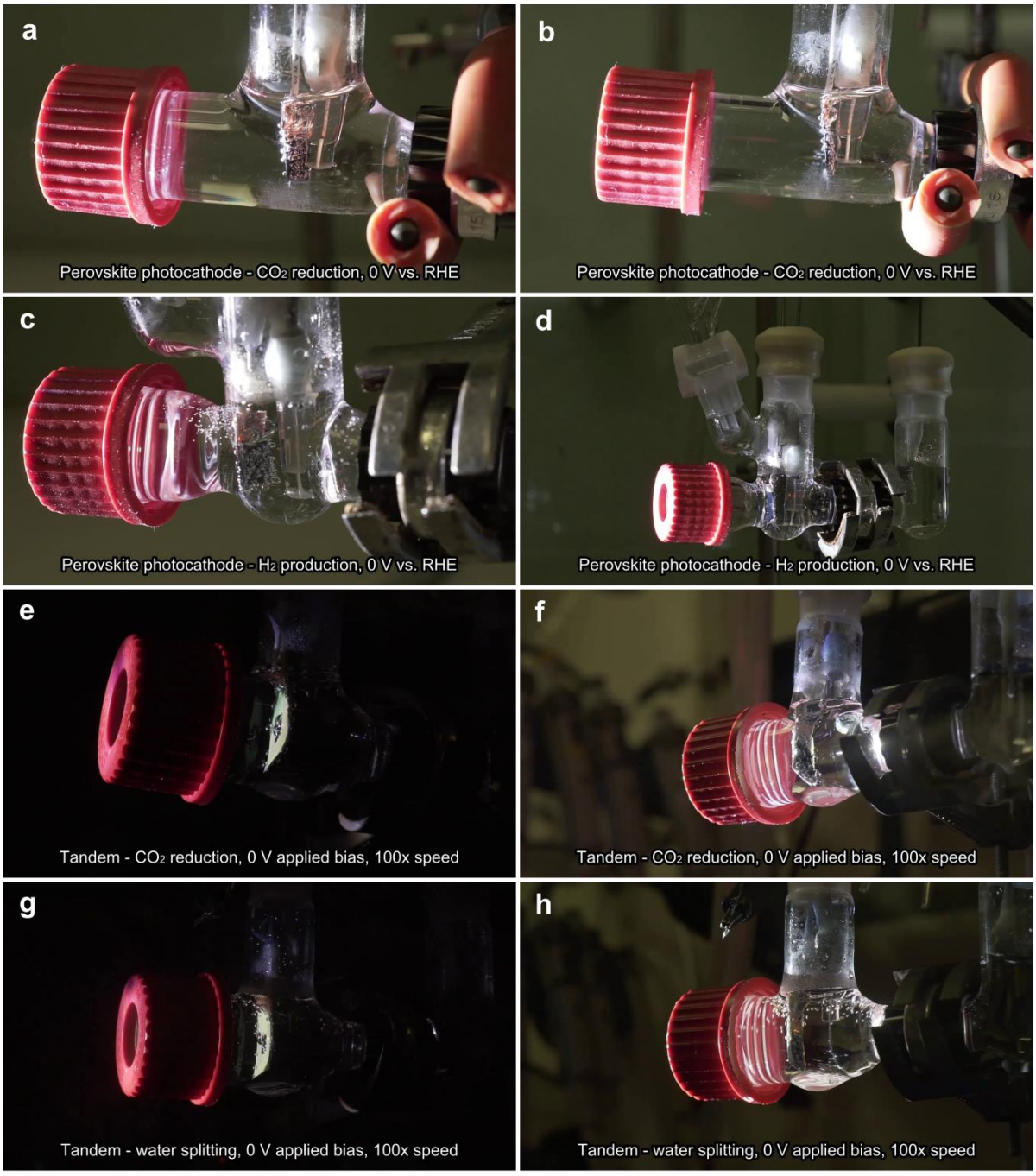

Supplementary Fig. 41 | Snapshots from Supplementary Video 1 depicting thin perovskite photocathodes and PEC devices under operation. a,**b**, fPVK|GE|CoMTPP@CNT photocathode at 0 V vs. RHE. **c**,**d**, fPVK|GE|Pt photocathode at 0 V vs. RHE. **e**,**f**, Ti|$BiVO_4$|TiCo – fPVK|GE|CoMTPP@CNT PEC device at 0 V applied bias. **g**,**h**, Ti|$BiVO_4$|TiCo – fPVK|GE|Pt PEC device at 0 V applied bias. The video is accelerated 100 times in case of the PEC devices to emphasize bubble formation (**e**-**h**).

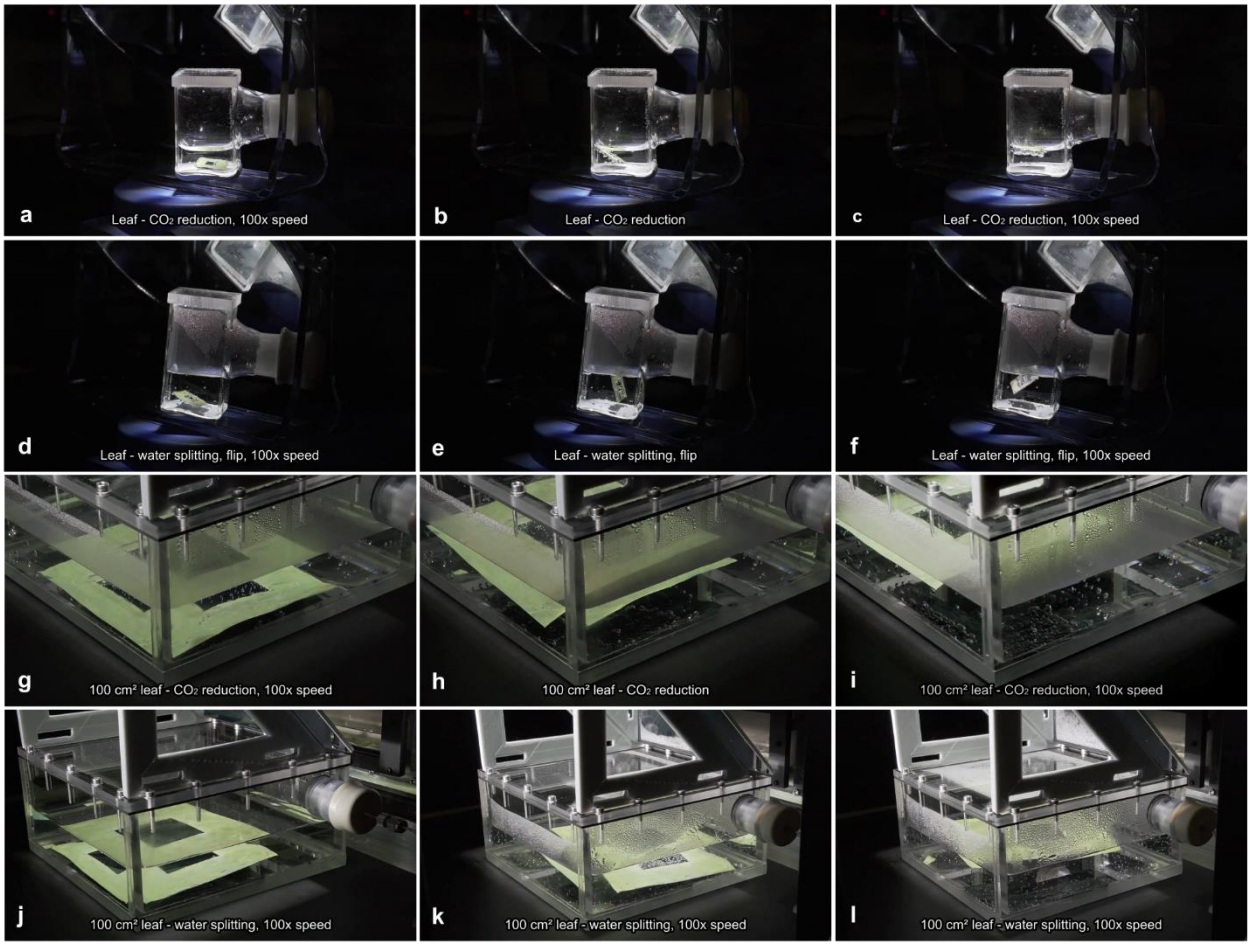

Supplementary Fig. 42 | Snapshots from Supplementary Videos 1 and 2 depicting the "lift-off" of floating lightweight artificial leaves under operation. **a**-**c**, 1.7 cm^2 Ti|$BiVO_4$|TiCo – fPVK|GE|CoMTPP@CNT small-scale PEC device. **d**-**f**, 1.7 cm^2 Ti|$BiVO_4$|TiCo – fPVK|GE|Pt artificial leaf. An initial prototype flips over during “lift-off”, due to a misalignment between the centres of mass of both photoelectrodes (see Supplementary Discussion 1). **g**-**i**, 100 cm^2 Ti|$BiVO_4$|TiCo – fPVK|GE|CoMTPP@CNT device. **j**-**l**, 100 cm^2 Ti|$BiVO_4$|TiCo – fPVK|GE|Pt artificial leaf. The video is accelerated 100 times, except for the lift-off periods which are played in real time.

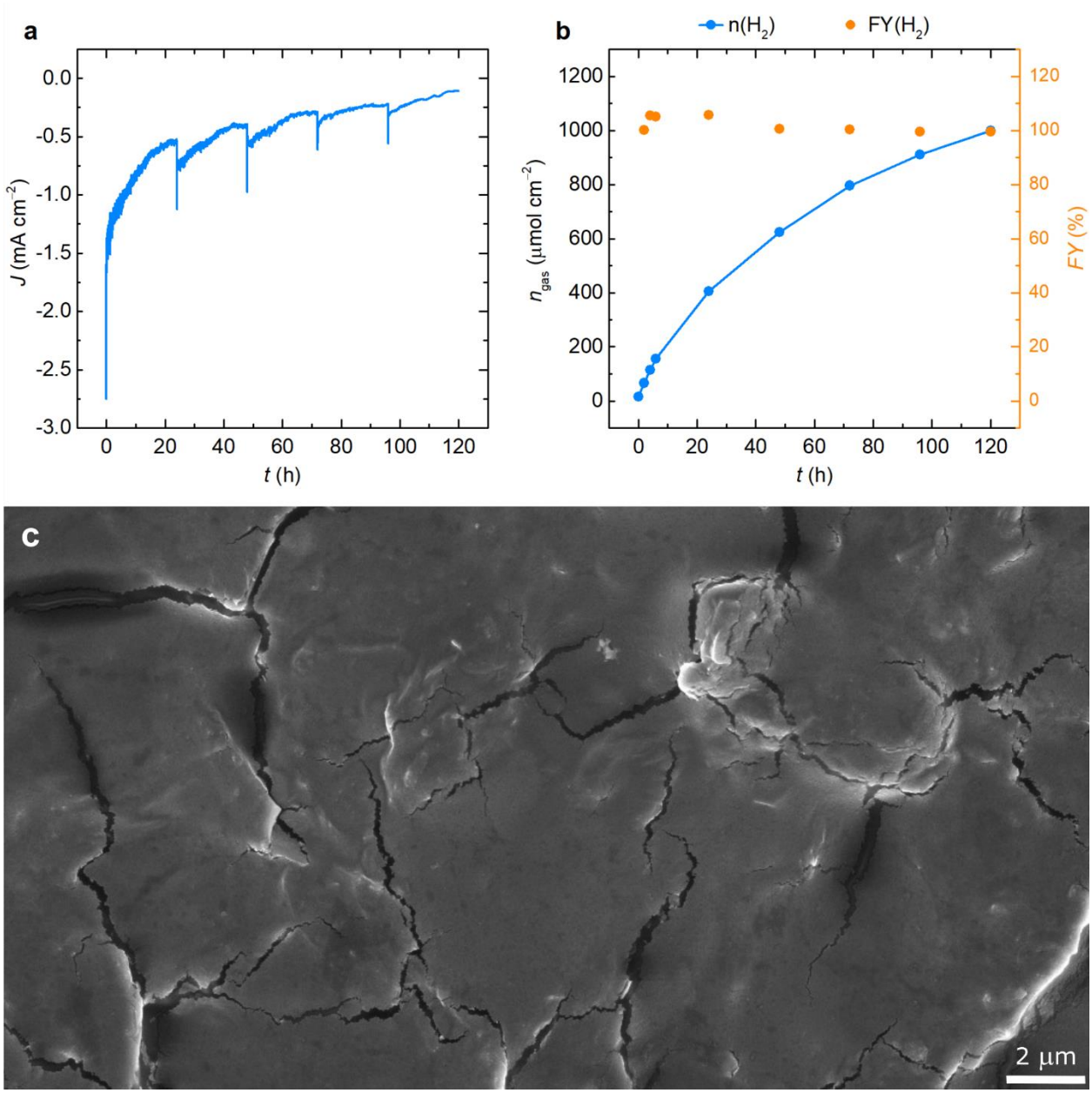

Supplementary Fig. 43 | Long-term stability tests of GE|Pt electrodes. a, Current trace. **b**, Amount of H_2 and faradaic yield. **c**, SEM image of the GE|Pt surface after a long-term test. Chronoamperometry is conducted at -0.2 V vs. RHE, in a three-electrode system with a Ag/AgCl reference and a Pt mesh counter electrode (0.1 M KB_i, 0.1 M K_2SO_4 solution, pH 8.5, replaced and purged with N_2 every 24 h). Tests were performed in a two-compartment cell with both compartments separated by a Selemion ion exchange membrane, hence the H_2 faradaic yield remained ≈100%. A gradual decrease in activity towards hydrogen evolution was observed, which could be traced back to nano-cracks forming in the Pt layer (**c**), as opposed to graphite epoxy degradation. No further degradation occurs due to UV irradiation, as the graphite paste is located underneath the lightweight device under operation, sheltered from direct sunlight irradiation.

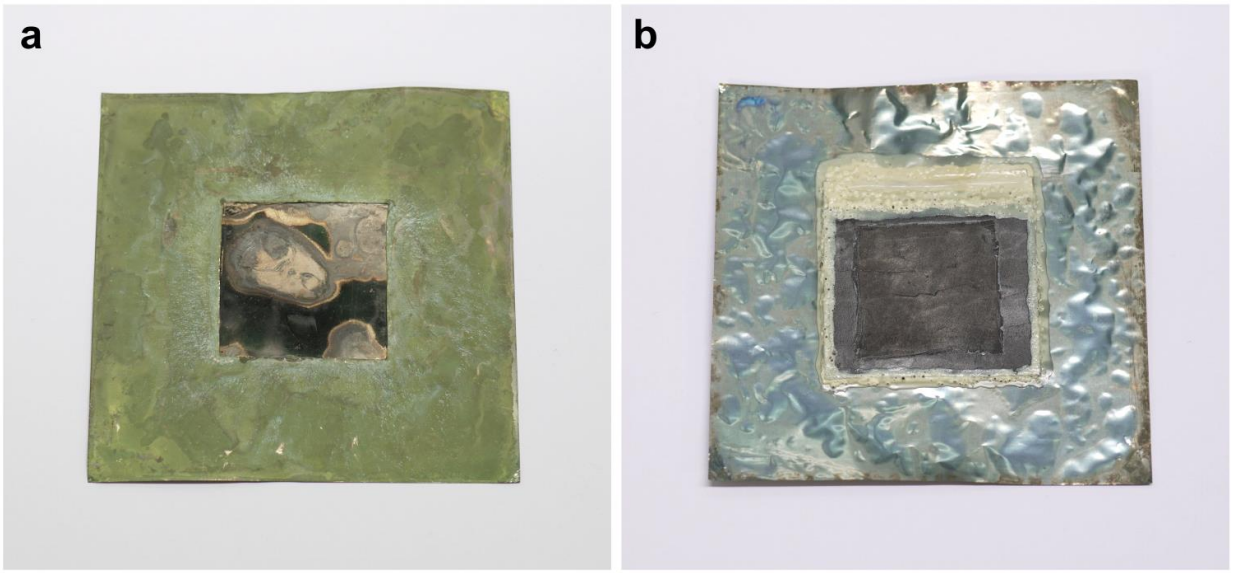

Supplementary Fig. 44 | Photographs of a 100 cm^2 Ti|$BiVO_4$|TiCo – fPVK|GE|Pt leaf after a 48 h water splitting test. a, View from the front side. **b**, Back side. The $BiVO_4$ photoanode displayed no visible signs of corrosion under operation, whereas moisture infiltration gradually degraded the perovskite light absorber. Images of the device before operation are given in Supplementary Fig. 39m,n.

Supplementary Fig. 45 | Interactions of floating leaves with local fauna. a, Inflatable reactors can act as rafts for insects. 13 flies can be seen on the surface of the floating reactor after 2.5 h of operation during outdoor tests, as indicated by the yellow circles. **b**, Birds may mistake the reactors for food.

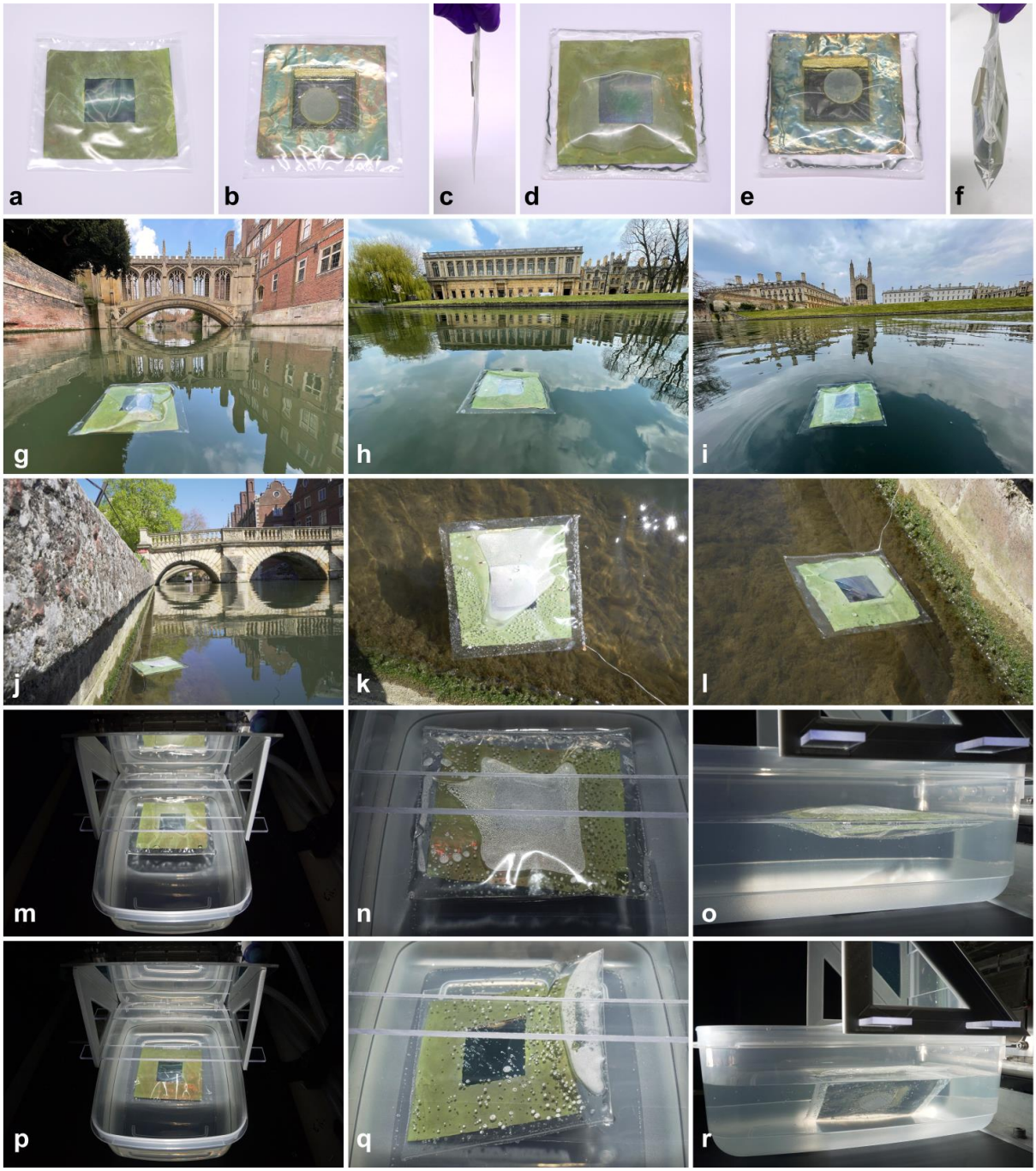

Supplementary Fig. 46 | Water splitting under real-world conditions using up-scaled samples. a-**f**, Thin artificial leaves inside a lightweight reactor. The low cost, lightweight reactor consists of a sealed, 12.5×12.5 cm^2 plastic bag. A rubber disk is attached with contact adhesive as a septum for gas sampling. **a**-**c**, Empty reactor and sample weighing 8.5 g (54 mg cm^{-2}). **d**-**f**, Reactor is filled with 100 mL electrolyte solution (0.1 M KB_i, 0.1 M K_2SO_4 solution, pH 8.5) and 20 mL gas (air or N_2). **g**-**i**, Outdoor test performed along the river Cam on a partly cloudy day in front of: **g** – the Bridge of Sighs, St John's College, **h** – Wren Library, Trinity College, **i** – King's College, Cambridge. **j**-**l**, Outdoor test performed under a clear sky. The reactor is moored on the banks of river Cam close to Wren Bridge, St John's College. The time dependence of the light intensity during the two tests is plotted in Supplementary Fig. 47. **m**-**r**, Laboratory tests of the floating reactor, containing 100 mL electrolyte solution (0.1 M KB_i, 0.1 M K_2SO_4 solution, pH 8.5, under N_2). **m**-**o**, 20 mL N_2 are added to the reactor to facilitate buoyancy and simulate steady-state operation. **p**-**r**, No external gas is added. The reactor gains buoyancy as the H_2 + O_2 product mixture accumulates.

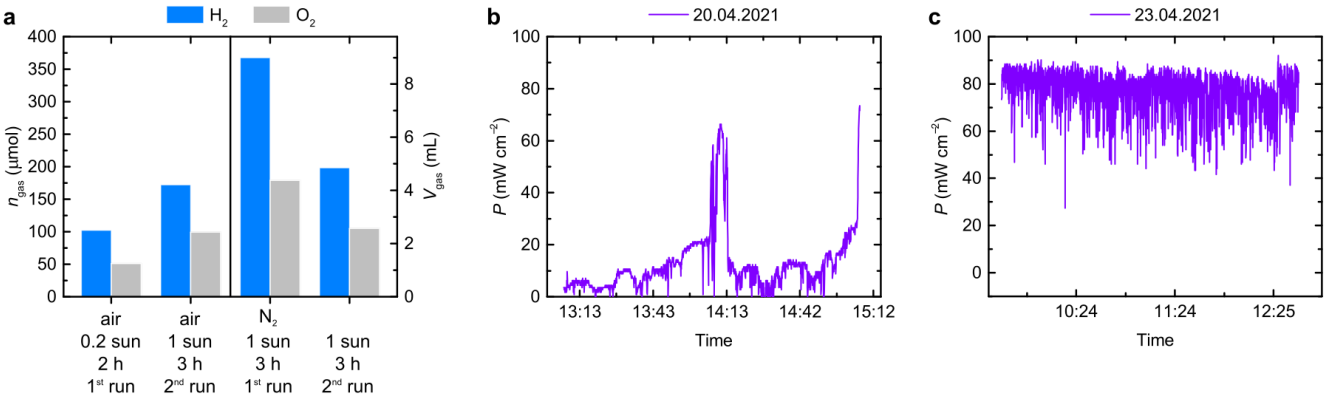

Supplementary Fig. 47 | Performance of the thin artificial leaves for water splitting under real-world conditions. a, Amounts of H_2 and O_2 and corresponding volumes of gas accumulated in the lightweight reactors under outdoor (left) and laboratory (right) conditions (see Supplementary Fig. 46g-i, j-l, m-o and p-r for the respective conditions). **b**, Light intensity during a 2 h test on the 20th of April 2021, between 13:07 - 15:07 (mostly cloudy, corresponding to roughly 0.2 sun, T ≈ 15 °C). **c**, Light intensity during a 3 h test on the 23rd of April 2021, between 9:40 - 12:40 (clear sky, corresponding to ≈1 sun, T_{water} ≈ 15 °C, T_{air} ≈ 20-25 °C). Outdoor tests were performed in 100 mL of an unpurged 0.1 M KB_i, 0.1 M K_2SO_4 (pH 8.5) electrolyte solution, in the presence of 20 mL air, to emulate the simple setup which would be employed in real-world applications, whereas the solution was purged with N_2 for laboratory tests. Electrolysis tests employing FTO|TiCo – GE|Pt as a model 2-electrode system in a one-compartment reactor sustained absolute currents of 0.3-0.4 mA at 1.9 V applied bias, displaying similar faradaic yields ≈60% for H_2 and O_2 production under both N_2 or air atmosphere. These values are in line with the results obtained for the Ti|$BiVO_4$|TiCo – fPVK|GE|Pt devices, indicating that an O_2 atmosphere does not significantly inhibit the device performance towards overall water splitting. While O_2 reduction does decrease the faradaic yields to around 60% (Supplementary Fig. 33), a sufficient amount of product is still formed. In the future, this back reaction can be avoided by integrating the leaf into an ion exchange membrane which separates the reactor into a cathodic and an anodic compartment, as proposed in Supplementary Figs. 49c,51. Two tests were performed for each sample under outdoor and laboratory conditions, to demonstrate the reusability of the leaves. The lightweight leaf employed for outdoor tests was assembled from a 4-month-old encapsulated fPVK|GE device and a reused Ti|$BiVO_4$|TiCo photoanode, whereas the Ti|$BiVO_4$|TiCo electrode used in laboratory tests was fabricated onto a cleaned and reused Ti foil, further demonstrating the recyclability of the leaf components. A H_2:O_2 ratio of roughly 2:1 was observed in all cases (**a**), whereas light scattering through water condensation and gas bubble formation, gradual device degradation and weather conditions influenced the absolute product amounts (see Supplementary Fig. 46). As shown in Supplementary Fig. 46, small O_2 bubbles accumulate into a larger bubble covering 20-40% of the photoanode area inside the inflatable reactor, which may cause optical losses above 5%.[31]

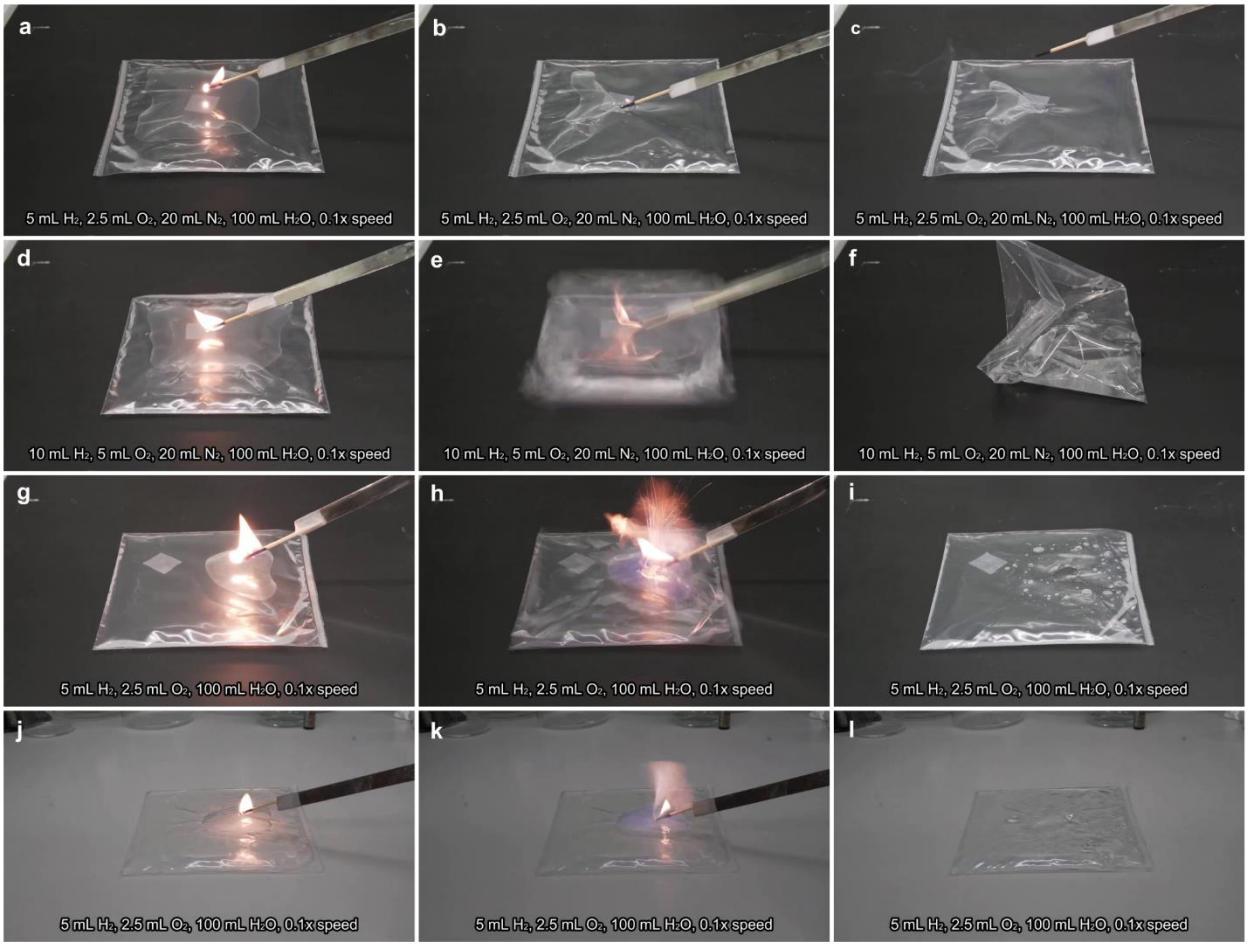

Supplementary Fig. 48 | Snapshots from Supplementary Video 3 depicting ignition tests of explosive gas mixtures in sealed bag reactors. Each reactor contains 100 mL Milli-Q water and given amounts of H_2, O_2 and N_2. The fluids are injected in the bags with a syringe, while the needle holes are secured with common adhesive tape. **a**, 5 mL H_2, 2.5 mL O_2, 20 mL N_2 mixture resembling the experimental results in Supplementary Fig. 47 does not ignite when subjected to an open flame. **b**, A 10 mL H_2, 5 mL O_2, 20 mL N_2 mixture does ignite, however the reactor preserves its contents. **c**,**d**, 5 mL H_2, 2.5 mL O_2 mixtures ignite rapidly in the presence of a flame. In all cases, no damage is observed to the reactor besides the direct burn caused by the flame, which can be easily patched in case of practical applications.

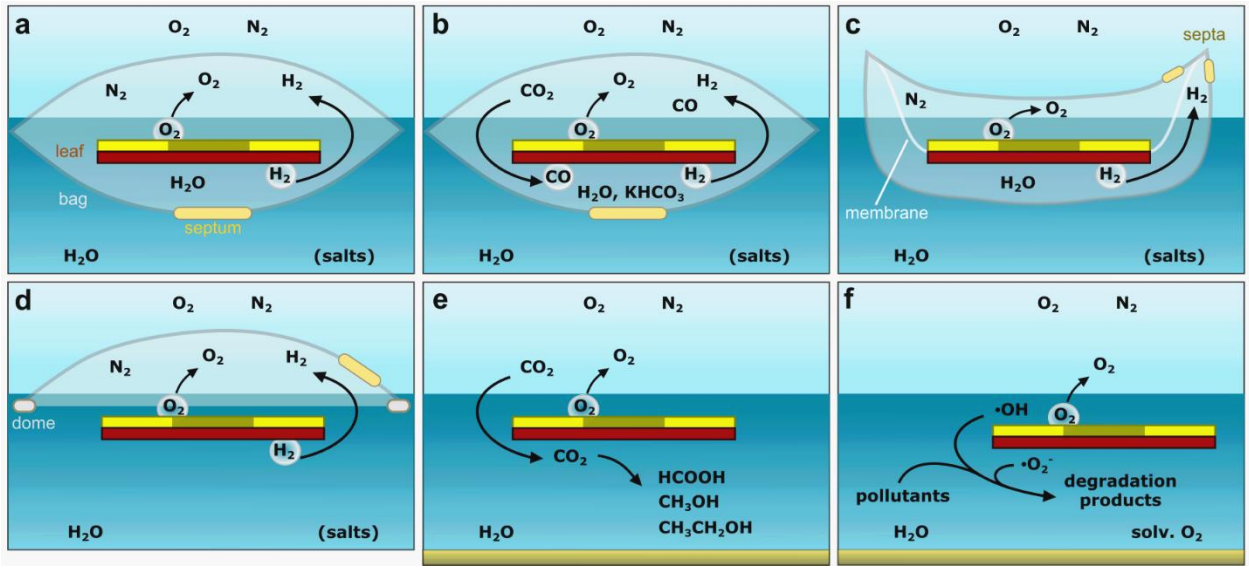

Supplementary Fig. 49 | Potential operation modes of floating PEC devices under real-world conditions. **a**-**c**, Sealed floating reactor. **d**-**f**, Free-floating devices. **a**, Water splitting can be performed from an aqueous solution, in a low-cost sealed bag reactor. In this depiction, the reactor contains a given amount of gas to aid flotation, which is more suitable for deep/open water applications (Supplementary Fig. 46g-o). The O_2 tolerance of the lightweight leaf (see Supplementary Fig. 47) translates in a more facile operation, as the reactors can be loaded and operated under air. No additional gas is required in shallow waters, since the reactor gains buoyancy as products are formed (Supplementary Fig. 46p-r). In that case, a concentrated mixture of products is obtained, which facilitates gas collection and product separation. **b**, The sealed bag reactor also enables aqueous CO_2 reduction to syngas, since the electrolyte solution and atmosphere are separated from the outside (n.b. electrolyte solution and gases can be exchanged through a gastight septum or valve). This approach also mitigates the risks of environmental contamination through lead leakage from perovskite degradation.[32] **c**, The lightweight leaf can be integrated with an ion exchange membrane, which separates the reactor into a cathodic and an anodic compartment. The reductive and oxidative products (e.g. H_2 and O_2) can be collected through separate septa, without forming explosive gas mixtures, or requiring an external gas-separation unit (see Supplementary Discussion 2). **d**, A floating dome approach may suit shallow water applications (i.e. coastal areas, lakes, artificial irrigation or salt evaporation ponds[33]). In this case, the gas products are collected below a membrane, which is held above the device by a floating cord (similar to the booms employed for oil spill removal[34,35]). For examples **a**,**b**,**d**, gas product separation can be performed via molecular sieving on microporous membranes with energy losses around 1%**,** as described in previous literature.[6] **e**, In case of free-floating devices, O_2 can be rapidly released into the atmosphere, while liquid or water-soluble products resulting from reductive processes can be accumulated within shallow waters (e.g. salt evaporation ponds). These products can either be collected by evaporation (e.g. formate[7]), or fed to microorganisms for further bioorganic transformations[16] (e.g. ethanol, methanol). **f**, Similarly, free-floating devices can be employed for water purification,[9] where the benign products of pollutant degradation remain in solution. An electron can be extracted from the pollutant,[9] creating a labile radical species. Dissolved O_2 molecules can be reduced to $\cdot O_2^-$, while hydroxyl groups can be oxidised to form reactive ·OH radicals. The resulting $\cdot O_2^-$ and ·OH radical species can themselves react with pollutants, resulting in their decomposition.[36]

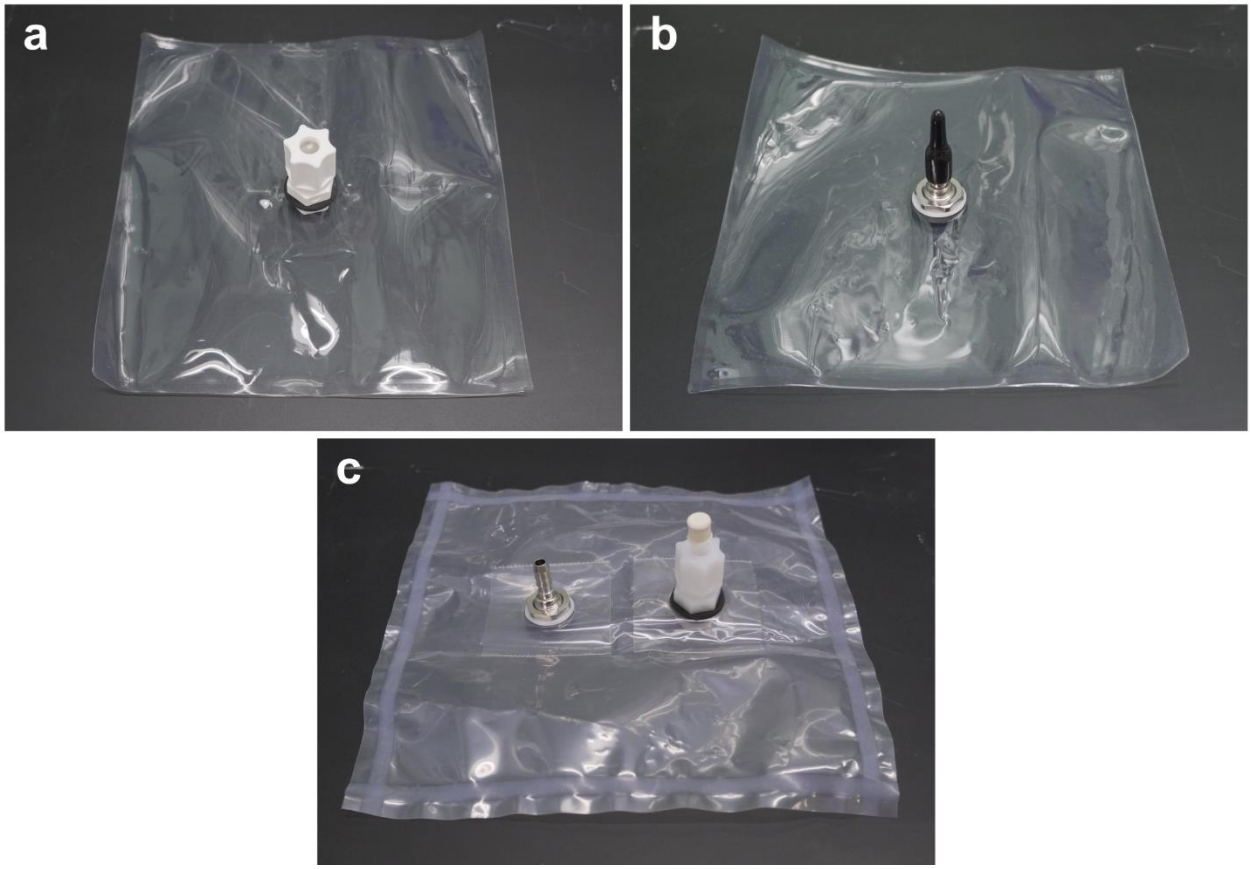

Supplementary Fig. 50 | Photographs of commercially available gas sampling bags. a, 15×15 cm^2 bag with a silicone septum in polypropylene housing. **b**, 15×15 cm^2 bag with an on/off valve (nickel-plated brass hose barb). **c**, Dual-valve model with both on/off valve and rubber septum.

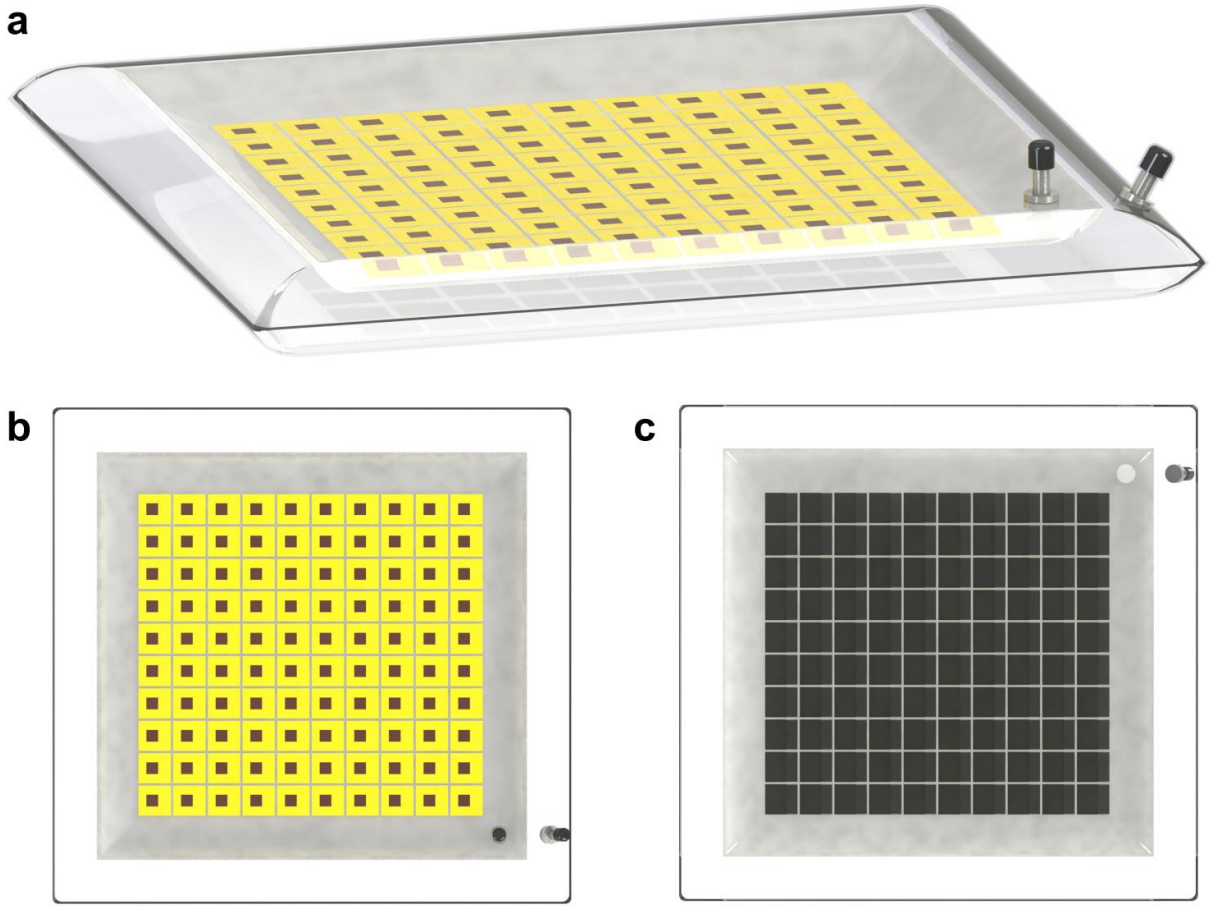

Supplementary Fig. 51 | Concept art for a large-scale floating reactor employing a 10×10 array of floating leaves. The leaves are integrated into an ion exchange membrane, which separates the reactor in an anodic and cathodic compartment, preventing product mixture. The reductive and oxidative gas products can be collected through separate valves. **a**, Perspective view. **b**, Top view. **c**, View from underneath the reactor. Assuming a size of 10×10 cm^2 for each individual lightweight device, the total area of this reactor design would amount to roughly 1.6×1.6 m^2 (valves are not drawn to scale).

Supplementary Discussion 1 | Electrode design and optimisation.

The deposition of $BiVO_4$ and perovskite light absorbers onto thin metal and plastic substrates poses several challenges. Therefore, a careful rational design of the components was needed, and further tests were performed to understand the best deposition conditions. Besides material and device development, a number of other practical considerations were crucial in enabling our lightweight devices to float, as described in detail below.

Perovskite deposition. A key reason for employing perovskite devices has been the high power-per-weight they can achieve when deposited onto lightweight plastic substrates.[37] This could translate to a very high activity per gram of our perovskite photocathodes, which surpasses conventional solar fuel panels and is even comparable to the activity of photocatalyst suspensions (see Fig. 3g and corresponding metrics in Supplementary Table 6). As we use thin plastic substrates, all deposition steps need to be performed via solution processing at temperatures below 423 K (see thermogravimetric analysis in Supplementary Fig. 16).

Perovskite devices with a PEDOT:PSS hole selective layer can only employ a $MAPbI_3$ solution in DMF, as DMSO increases the conductivity of PEDOT:PSS,[38] thereby shorting the device structure. However, the simple $MAPbI_3$ phase is known to degrade faster under continuous irradiation and moisture exposure, whereas the acidic, hydrophilic PEDOT:PSS promotes device degradation. The intermediate PTAA HTL provides a barrier between PEDOT:PSS and the perovskite layer, enabling us to employ a state-of-the-art, DMSO containing triple cation, mixed halide perovskite solution. Hence, the introduction of the PTAA layer is a crucial advance enabling the fabrication of perovskite devices onto flexible substrates.

$BiVO_4$ deposition. Some key considerations also need to be taken into account for the photoanode fabrication. The $BiVO_4$ fabrication occurs at high temperatures, which restricts the choice of substrates to thin metal foils. We found that several metals (e.g. Cu, Fe) are reactive under the BiOI electrodeposition conditions, hence only relatively inert metals are suitable for this procedure. On the other hand, metals like Al, Fe or Ti present passivating surface oxide layers, which can also strongly inhibit the BiOI electrodeposition. Among those, the best BiOI homogeneity was obtained when dipping Ti foils in concentrated H_2SO_4, which briefly removes the native TiO_2 layer before electrodeposition. A further variation of the etching conditions and film thickness was necessary to achieve the optimal $BiVO_4$ nanostructure morphology, which resembles the one previously reported by Choi et al.[28] Finally, adapted procedures, a custom-made 3D-printed electrodeposition chamber and 100 cm^2 graphite foil counter electrode were necessary to upscale the BiOI deposition to 84 cm^2.

Device design. The photocathode window is placed by design in the middle of the $BiVO_4$ photoanode, to conserve the centre of mass and thereby balance the floating leaf under operation. As the perovskite photoanode has a higher mass per area, it needs to be placed at the centre of the device, otherwise the buoyancy force exerted by H_2 and CO bubbles formed underneath the leaf will flip the device over, as observed for some initial small-scale prototypes (see Supplementary Fig. 42d-f, Video 1). This design is also proven from a bio-mimetic perspective, since marine life including lotus leaves, jellyfish and squids follow a similar centrosymmetric pattern.

The size of the photoanode and its window can be simply adjusted by cutting the thin Ti foil with common scissors or a scalpel in any desired shapes, similar to a paper sheet. This enables a more homogeneous perovskite deposition over a square substrate, minimising pinholes and macroscopic defects in the device structure. The central arrangement can also decrease resistive losses within both perovskite and $BiVO_4$ electrodes, as charges may need to travel over a longer distance in a side-by-side configuration.

Supplementary Discussion 2 | Floating leaves in the context of state-of-the-art solar fuels systems.

Comparison of established and lightweight systems. Light-driven fuel production could mitigate our reliance on fossil fuels. Therefore, there is a great interest in bringing solar fuel technologies closer to practical applications.[39] The main challenges towards this goal are their stability, scalability and cost, as commercial systems must operate for several years on a square-meter scale. Yet, due to complex deposition procedures, most prototypes possess small active areas below 5 cm^2, while their stability is only reported for several hours.[39] Solar fuel production can be performed in different configurations, including PV-electrolysers, photoelectrochemical (PEC) or photocatalytic (PC) systems, as indicated in Supplementary Table 6. These systems possess distinct advantages in terms of performance, cost and complexity, which make them suitable for different applications, as described in more detail below.

PV-electrolyser systems are commercially mature and ever more electrolysis plants are installed worldwide. The main advantage of those systems is their modularity, since high-performance electrolysers can be directly coupled to state-of-the-art solar cells or other renewable electricity sources. As a result, PV-electrolyser prototypes can attain a solar-to-hydrogen (STH) efficiency of 20-30%,[39,40] with commercial large-scale systems already reaching 15% STH.[41,42] Hence, these systems are of greater economic and societal importance on the short term. On the other hand, many PV-electrolysers employ corrosive electrolytes and noble metal electrocatalysts, complex flow reactors, additional wiring and electronics, which will increase their overall complexity and operational cost.[43]

Photocatalytic suspensions provide an inexpensive alternative for solar fuel production. Often, semiconductor particles are dispersed in a solution containing a catalyst and a (sacrificial) electron donor. This approach requires no additional components (e.g. substrates, or wiring), which results in a high fuel production activity per gram of photocatalyst.[8] However, the separation of the original components and soluble products from the reaction mixture provides a challenge. This can be mitigated by immobilising photocatalyst powders onto a conductive substrate. The resulting PC sheets can employ either one or two light absorbers for overall water splitting and CO_2 reduction. For example, a 100 m^2 array of Al-doped $SrTiO_3$ sheets could recently operate over 3 months,[44] whereas a $SrTiO_3$ - $BiVO_4$ sheet could achieve a 0.08% solar-to-formate efficiency.[7] However, due to the wider band gap of the light absorbers, best prototypes achieve efficiencies around 1%.[6,44,45] On the other hand, photocatalyst panels require annealing at 573 K to form a good contact between the gold conductive layer and the semiconductor particles.[7] This step limits the choice of substrates, as thin plastic films become deformed or degrade at higher temperatures.

Photoelectrochemical “artificial leaves” provide a middle ground between PV-electrolysis and PC approaches, as compact PEC panels can also attain high STH efficiencies (>10% for state-of-the-art tandem devices[39]). In this case, the oxidation and reduction products are formed on different sides of the integrated devices, which facilitates product separation. Yet, most current prototypes are still bulky, relying on conductive glass substrates and thick encapsulant layers.

As hinted above, the performance of solar fuels systems can be evaluated based on various criteria, such as solar-to-fuel efficiency, rate of product per irradiated area, or activity per gram. Hence, lightweight devices can stand out through a high activity per gram, compensating the difference in efficiency. For example, a 10-times lighter 0.5% STH device could attain a similar activity per gram to a regular 5% STH device. In addition, our floating leaves employ lightweight, low-cost inflatable reactors, and can perform water splitting in benign, neutral pH solutions under air (Supplementary Fig. 47). These aspects become crucial from an economic perspective, as material usage contributes to the overall device cost.[46] Commercial light harvesting systems need to operate for several years to offset their fabrication costs,[47] hence lightweight devices could justify lower efficiencies and stabilities from a cost perspective. Our system provides a good balance between device performance and material consumption, which will play a more important role in the long run, once such lightweight devices approach the efficiency and stability of PV-electrolyser systems.

Further improvements towards practical applications. This work provides a proof-of-concept for lightweight artificial leaves. Small-scale devices reached unassisted solar-to-fuel efficiencies of up to 0.58%, whereas 100 cm^2 floating prototypes could operate for over 30 h. Gas collection was further demonstrated under laboratory and outdoor tests using inexpensive, inflatable reactors. While these experiments showcase the potential of floating PEC devices towards practical uses, further improvements are required in terms of efficiency, upscaling and long-term operation.

Moisture infiltration represents the main cause of perovskite degradation (Supplementary Fig. 44), hence the device lifetime could be increased beyond a month by further developing the encapsulation techniques. This could be performed by optimising the thickness of the parylene-C coating or adjusting the encapsulant paste composition. For the latter, different combinations of carbon allotropes (i.e. carbon nanotubes, graphene) and polymer binders can result in thinner, more conductive, more flexible and less porous coatings.[48,49] Further progress could be made by standardising the encapsulant deposition method, as large-scale blade coating techniques would ensure a more homogeneous deposition over our manual procedure.[50] The perovskite device structure could be further replaced by other thin film alternatives including organic photovoltaic,[51] dye-sensitised[52] or $Cu(In,Ga)Se_2$ (CIGS) solar cells,[53] which are lead-free and may prove more robust in the presence of moisture. Such modifications may push the operational stability of large-scale floating devices beyond a year, which would suit practical applications. Their practical implementation will be accelerated by the reduced fabrication costs and encouraging recyclability of the floating leaves (Supplementary Fig. 47).

The overall efficiency of tandem PEC systems is limited by the overlap between the photocurrents of the two electrodes (examples given in Supplementary Fig. 30). The photocurrent of our lightweight device is constrained by the $BiVO_4$ photoanode, which only absorbs light at wavelengths below 500 nm (Supplementary Fig. 24). In this study, we improved the photocurrent overlap by increasing the active area of the $BiVO_4$ photoanode in respect to the perovskite photocathode (Supplementary Fig. 30). Photocurrents above 4 mA cm^{-2} have been reported for $BiVO_4$ photoanodes deposited on conventional FTO glass substrates,[28,54,55] hence a further optimization of the Ti-based electrodes may increase the STH efficiency of floating leaves beyond 3%. State-of-the-art transparent photoanodes employing wide-bandgap perovskite,[56] or organic photovoltaic[55,57] light absorbers could replace the opaque $Ti|BiVO_4$ electrode, which would further decrease the overall device area. This could result in floating PEC tandems with STH efficiencies beyond 5%, which would suit commercial applications.

Practical and environmental aspects of floating PEC systems. Our lightweight prototypes provide a proof-of-concept for solar fuel production onto open waters. This mode of operation enables a facile device removal from the reaction medium, providing an advantage over conventional PC systems, while sealed floating reactors can also mitigate lead leakage. A reduction in material usage would further reflect on the often-overlooked recyclability of the devices, with the metal-carbon-based skeleton making the component separation straightforward (Supplementary Fig. 47). At last, this example of a lightweight PEC architecture opens up the field to the opportunities of state-of-the-art roll-to-roll techniques (e.g. inkjet, or screen printing; spray, slot-die, or blade coating), which are already in use for the further upscaling of flexible, thin-film solar cells.[50,51] These techniques may be employed to fabricate inexpensive, non-brittle PEC devices, which could be easily deployed on a larger scale. However, a number of other safety and environmental factors also need to be taken into account, including the collection and handling of the gas products, or the effect of floating devices on the aquatic life.

During outdoor tests, we demonstrated that gases can be collected in a facile manner by placing the lightweight leaves in a thin, inflatable reactor. In this case, a rubber disk was attached to the floating reactors, acting as a low-cost septum. Gases could be easily sampled and collected through this septum using gastight syringes. A similar principle can be applied on a larger scale. In this case, the modularity of our approach would mitigate resistive losses, as 100 cm^2 devices can be tiled side-by-side to cover a larger area, instead of requiring a single, square-meter leaf. A larger inflatable reactor could contain an array of 100 cm^2 floating leaves, held together by an ion exchange membrane which would prevent voltage losses due to pH gradient build-up (Supplementary Fig. 51). Since oxidative and reductive products form on

opposite sides of the artificial leaves, the membrane would separate the inflatable reactor into a cathodic and an anodic compartment preventing product mixture, with separate ports for $CO+H_2$ and O_2 collection (Supplementary Figs. 49c,51). This would provide an advantage over PC sheets, which require an additional, external gas-separating membrane unit, which may be challenging to operate at sea. Nevertheless, the ignition of potentially explosive gas mixtures in a closed reactor may confine the blast effect, as recently demonstrated by Domen et al.[44] To prove this, we performed ignition tests on our inflatable reactors, which were filled with given amounts of H_2, O_2 and N_2, to resemble experimental conditions. During those tests, the reactors preserved their liquid contents, and no damage was observed to the reactors besides the direct burn caused by the flame, which can be easily patched (see Supplementary Fig. 48, Video 3). For practical applications, gases could be collected daily or weekly by suction through inbuilt, custom-made septa and valves, which are regularly deployed for gas sampling applications (Supplementary Fig. 50), and pressurised for later use. Several reactors can be confined to a certain area by a floating cord, suitable anchoring, or mooring systems,[58] which facilitate their retrieval for gas collection.

Floating devices would provide an advantage over conventional light harvesting systems by avoiding competition with land use. The effect of such systems on aquatic life and aquatic food production can be estimated by looking at recent studies on floating photovoltaic platforms[58] and floating covers supressing water evaporation.[59] Generally, floating platforms provide shading, decreasing water temperature near the surface.[58] This is particularly beneficial for agriculture in warm countries, where water evaporation from irrigation ponds or water canals poses a major challenge.[59] Shading also decreases photosynthesis, reducing phytoplankton and algae growth, which can in turn improve water quality. However, less photosynthesis can decrease the quantity of dissolved oxygen and disrupt food chains.[58,60] A 50% surface coverage by floating platforms can decrease the net primary production (a measure of the biomass production) by 15-30%.[61] Hence, floating reactors should leave space in between individual artificial leaves, which corresponds to our proposed design in Supplementary Fig. 51. Taking this into account, floating PV solar farms have been successfully combined with aquaculture.[62] Biofouling constitutes a potential challenge for floating systems;[60] however, lightweight inflatable reactors could be easily replaced with little material consumption. In our case, we observed that inflatable reactors can act as rafts for insects, whereas birds may confuse it with food (Supplementary Fig. 45). Hence, the flexible reactors must be fabricated from a sturdy, yet elastic film. Alternatively, floating systems could be installed on abandoned grounds, heavily industrialized or polluted waters with limited aquatic life, such as mining lakes,[63] or near ports where they would supply fuel for ships. In a broader sustainable fuel economy, floating systems could work in parallel with conventional solar fuels technologies. High-performance PV-electrolysers would be more suitable in the vicinity of dense urban centres, whereas floating leaves with lower efficiencies could operate over a wider area in remote locations with smaller fuel demands. Accordingly, such lightweight systems could be deployed over shallow artificial lakes, coastal settlements, islands, offshore ship refuelling facilities, or remote locations which are only accessible by air.

Supplementary References

1. Andrei, V., Reuillard, B. & Reisner, E. Bias-free solar syngas production by integrating a molecular cobalt catalyst with perovskite–$BiVO_4$ tandems. *Nat. Mater.* **19,** 189–194; 10.1038/s41563-019-0501-6 (2020).

2. Edwardes Moore, E., Andrei, V., Zacarias, S., Pereira, I. A. C. & Reisner, E. Integration of a Hydrogenase in a Lead Halide Perovskite Photoelectrode for Tandem Solar Water Splitting. *ACS Energy Lett.* **5,** 232–237; 10.1021/acsenergylett.9b02437 (2020).

3. Cheng, W.-H. *et al.* Monolithic Photoelectrochemical Device for Direct Water Splitting with 19% Efficiency. *ACS Energy Lett.* **3,** 1795–1800; 10.1021/acsenergylett.8b00920 (2018).

4. Rani, A., Kumar Vats, S., Sharma, M. & Kumar, S. Catechin promotes growth of Arabidopsis thaliana with concomitant changes in vascular system, photosynthesis and hormone content. *Biol. Plant.* **55,** 779; 10.1007/s10535-011-0187-3 (2011).

5. Goto, N., Sando, S., Sato, Y. & Hasegawa, K. Effects of Lepidimoide on Growth and Development of *Arabidopsis thaliana*. *J. Weed Sci. Technol.* **40,** 87–94; 10.3719/weed.40.87 (1995).

6. Wang, Q. *et al.* Scalable water splitting on particulate photocatalyst sheets with a solar-to-hydrogen energy conversion efficiency exceeding 1%. *Nat. Mater.* **15,** 611 (2016).

7. Wang, Q. *et al.* Molecularly engineered photocatalyst sheet for scalable solar formate production from carbon dioxide and water. *Nat. Energy* **5,** 703–710; 10.1038/s41560-020-0678-6 (2020).

8. Kasap, H., Achilleos, D. S., Huang, A. & Reisner, E. Photoreforming of Lignocellulose into H_2 Using Nanoengineered Carbon Nitride under Benign Conditions. *J. Am. Chem. Soc.* **140,** 11604–11607; 10.1021/jacs.8b07853 (2018).

9. Achilleos, D., Kasap, H. & Reisner, E. Photocatalytic Hydrogen Generation Coupled to Pollutant Utilization Using Carbon Dots Produced from Biomass. *Green Chem.* **22,** 2831-2839; 10.1039/D0GC00318B (2020).

10. Uekert, T., Kasap, H. & Reisner, E. Photoreforming of Nonrecyclable Plastic Waste over a Carbon Nitride/Nickel Phosphide Catalyst. *J. Am. Chem. Soc.* **141,** 15201–15210; 10.1021/jacs.9b06872 (2019).

11. Uekert, T., Kuehnel, M. F., Wakerley, D. W. & Reisner, E. Plastic waste as a feedstock for solar-driven H_2 generation. *Energy Environ. Sci.* **11,** 2853–2857; 10.1039/C8EE01408F (2018).

12. Achilleos, D. S. *et al.* Solar Reforming of Biomass with Homogeneous Carbon Dots. *Angew. Chem. Int. Ed.* **59,** 18184–18188; 10.1002/anie.202008217 (2020).

13. Roy, S. & Reisner, E. Visible-Light-Driven CO_2 Reduction by Mesoporous Carbon Nitride Modified with Polymeric Cobalt Phthalocyanine. *Angew. Chem. Int. Ed.* **58,** 12180–12184; 10.1002/anie.201907082 (2019).

14. Kuehnel, M. F. *et al.* ZnSe quantum dots modified with a Ni(cyclam) catalyst for efficient visible-light driven CO_2 reduction in water. *Chem. Sci.* **9,** 2501–2509; 10.1039/C7SC04429A (2018).

15. Dogutan, D. K. & Nocera, D. G. Artificial Photosynthesis at Efficiencies Greatly Exceeding That of Natural Photosynthesis. *Acc. Chem. Res.* **52,** 3143–3148; 10.1021/acs.accounts.9b00380 (2019).

16. Liu, C., Colón, B. C., Ziesack, M., Silver, P. A. & Nocera, D. G. Water splitting-biosynthetic system with CO_2 reduction efficiencies exceeding photosynthesis. *Science* **352,** 1210–1213; 10.1126/science.aaf5039 (2016).

17. Weraduwage, S. M. *et al.* The relationship between leaf area growth and biomass accumulation in Arabidopsis thaliana. *Front. Plant Sci.* **6,** 167; 10.3389/fpls.2015.00167 (2015).

18. Khan, Z. U. *et al.* Thermoelectric Polymers and their Elastic Aerogels. *Adv. Mater.* **28,** 4556–4562; 10.1002/adma.201505364 (2016).

19. Marinho, B., Ghislandi, M., Tkalya, E., Koning, C. E. & de With, G. Electrical conductivity of compacts of graphene, multi-wall carbon nanotubes, carbon black, and graphite powder. *Powder Technol.* **221,** 351–358; 10.1016/j.powtec.2012.01.024 (2012).

20. You, J. *et al.* Metal Oxide Nanoparticles as an Electron-Transport Layer in High-Performance and Stable Inverted Polymer Solar Cells. *Adv. Mater.* **24,** 5267–5272; 10.1002/adma.201201958 (2012).

21. Lee, J. *et al.* A Printable Organic Electron Transport Layer for Low-Temperature-Processed, Hysteresis-Free, and Stable Planar Perovskite Solar Cells. *Adv. Energy Mater.* **7,** 1700226; 10.1002/aenm.201700226 (2017).

22. Zhang, L. Q. *et al.* Highly efficient and stable planar heterojunction perovskite solar cells via a low temperature solution process. *J. Mater. Chem. A* **3,** 12133–12138; 10.1039/C5TA01898F (2015).

23. Liu, T., Chen, K., Hu, Q., Zhu, R. & Gong, Q. Inverted Perovskite Solar Cells: Progresses and Perspectives. *Adv. Energy Mater.* **6,** 1600457; 10.1002/aenm.201600457 (2016).

24. Juarez-Perez, E. J., Ono, L. K. & Qi, Y. Thermal degradation of formamidinium based lead halide perovskites into sym-triazine and hydrogen cyanide observed by coupled thermogravimetry-mass spectrometry analysis. *J. Mater. Chem. A* **7,** 16912–16919; 10.1039/C9TA06058H (2019).

25. Juarez-Perez, E. J., Hawash, Z., Raga, S. R., Ono, L. K. & Qi, Y. Thermal degradation of $CH_3NH_3PbI_3$ perovskite into NH_3 and CH_3I gases observed by coupled thermogravimetry–mass spectrometry analysis. *Energy Environ. Sci.* **9,** 3406–3410; 10.1039/C6EE02016J (2016).

26. Divitini, G. *et al.* In situ observation of heat-induced degradation of perovskite solar cells. *Nat. Energy* **1,** 15012; 10.1038/nenergy.2015.12 (2016).

27. Kulbak, M. *et al.* Cesium Enhances Long-Term Stability of Lead Bromide Perovskite-Based Solar Cells. *J. Phys. Chem. Lett.* **7,** 167–172; 10.1021/acs.jpclett.5b02597 (2016).

28. Kim, T. W. & Choi, K.-S. Nanoporous $BiVO_4$ Photoanodes with Dual-Layer Oxygen Evolution Catalysts for Solar Water Splitting. *Science* **343,** 990–994; 10.1126/science.1246913 (2014).

29. Ahmet, I. Y. *et al.* Demonstration of a 50 cm^2 $BiVO_4$ tandem photoelectrochemical-photovoltaic water splitting device. *Sustainable Energy Fuels* **3,** 2366-2379; 10.1039/C9SE00246D (2019).

30. Andrei, V. *et al.* Scalable Triple Cation Mixed Halide Perovskite–$BiVO_4$ Tandems for Bias-Free Water Splitting. *Adv. Energy Mater.* **8,** 1801403; 10.1002/aenm.201801403 (2018).

31. Holmes-Gentle, I., Bedoya-Lora, F., Alhersh, F. & Hellgardt, K. Optical Losses at Gas Evolving Photoelectrodes: Implications for Photoelectrochemical Water Splitting. *J. Phys. Chem. C* **123,** 17–28; 10.1021/acs.jpcc.8b07732 (2019).

32. Li, J. *et al.* Biological impact of lead from halide perovskites reveals the risk of introducing a safe threshold. *Nat. Commun.* **11,** 310; 10.1038/s41467-019-13910-y (2020).

33. Ahmed, M. *et al.* Use of evaporation ponds for brine disposal in desalination plants. *Desalination* **130,** 155–168; 10.1016/S0011-9164(00)00083-7 (2000).

34. Hoang, A. T., Pham, V. V. & Nguyen, D. N. A Report of Oil Spill Recovery Technologies. *Int. J. Appl. Eng. Res.* **13,** 4915–4928 (2018).

35. Violeau, D., Buvat, C., Abed-Meraim, K. & Nanteuil, E. de. Numerical modelling of boom and oil spill with SPH. *Coastal Eng.* **54,** 895–913; 10.1016/j.coastaleng.2007.06.001 (2007).

36. Pelaez, M. *et al.* A review on the visible light active titanium dioxide photocatalysts for environmental applications. *Appl. Catal. B Environ.* **125,** 331–349; 10.1016/j.apcatb.2012.05.036 (2012).

37. Kaltenbrunner, M. *et al.* Flexible high power-per-weight perovskite solar cells with chromium oxide-metal contacts for improved stability in air. *Nat. Mater.* **14,** 1032–1039 (2015).

38. Andrei, V. *et al.* Size Dependence of Electrical Conductivity and Thermoelectric Enhancements in Spin-Coated PEDOT:PSS Single and Multiple Layers. *Adv. Electron. Mater.,* 1600473; 10.1002/aelm.201600473 (2017).

39. Kim, J. H., Hansora, D., Sharma, P., Jang, J.-W. & Lee, J. S. Toward practical solar hydrogen production – an artificial photosynthetic leaf-to-farm challenge. *Chem. Soc. Rev.* **48,** 1908–1971; 10.1039/C8CS00699G (2019).

40. Jia, J. *et al.* Solar water splitting by photovoltaic-electrolysis with a solar-to-hydrogen efficiency over 30%. *Nat. Commun.* **7,** 13237 (2016).

41. The Solhyd Project. Available at https://solhyd.org/en/ (2021).

42. KU Leuven News. KU Leuven scientists crack the code for affordable, eco-friendly hydrogen gas. Available at https://nieuws.kuleuven.be/en/content/2019/belgian-scientists-crack-the-code-for-affordable-eco-friendly-hydrogen-gas (2019).

43. Joya, K. S., Joya, Y. F., Ocakoglu, K. & van de Krol, Roel. Water-Splitting Catalysis and Solar Fuel Devices: Artificial Leaves on the Move. *Angew. Chem. Int. Ed.* **52,** 10426–10437; 10.1002/anie.201300136 (2013).

44. Nishiyama, H. *et al.* Photocatalytic solar hydrogen production from water on a 100 m^2-scale. *Nature* **598,** 304–307; 10.1038/s41586-021-03907-3 (2021).

45. Goto, Y. *et al.* A Particulate Photocatalyst Water-Splitting Panel for Large-Scale Solar Hydrogen Generation. *Joule* **2,** 509–520; 10.1016/j.joule.2017.12.009 (2018).

46. Pinaud, B. A. *et al.* Technical and economic feasibility of centralized facilities for solar hydrogen production via photocatalysis and photoelectrochemistry. *Energy Environ. Sci.* **6,** 1983–2002; 10.1039/C3EE40831K (2013).

47. Ashby, M. F. (ed.). *Materials and the Environment* (Butterworth-Heinemann, Boston, 2013).

48. Hu, K., Kulkarni, D. D., Choi, I. & Tsukruk, V. V. Graphene-polymer nanocomposites for structural and functional applications. *Prog. Polym. Sci.* **39,** 1934–1972; 10.1016/j.progpolymsci.2014.03.001 (2014).

49. Chun, K.-Y. *et al.* Highly conductive, printable and stretchable composite films of carbon nanotubes and silver. *Nat. Nanotechnol.* **5,** 853–857; 10.1038/nnano.2010.232 (2010).

50. Li, Z. *et al.* Scalable fabrication of perovskite solar cells. *Nat. Rev. Mater.* **3,** 18017; 10.1038/natrevmats.2018.17 (2018).

51. Andersen, T. R. *et al.* Scalable, ambient atmosphere roll-to-roll manufacture of encapsulated large area, flexible organic tandem solar cell modules. *Energy Environ. Sci.* **7,** 2925–2933; 10.1039/C4EE01223B (2014).

52. Fakharuddin, A., Jose, R., Brown, T. M., Fabregat-Santiago, F. & Bisquert, J. A perspective on the production of dye-sensitized solar modules. *Energy Environ. Sci.* **7,** 3952–3981; 10.1039/C4EE01724B (2014).

53. Chirilă, A. *et al.* Highly efficient Cu(In,Ga)Se_2 solar cells grown on flexible polymer films. *Nat. Mater.* **10,** 857–861; 10.1038/nmat3122 (2011).

54. Sayama, K. *et al.* Photoelectrochemical decomposition of water on nanocrystalline $BiVO_4$ film electrodes under visible light. *Chem. Commun.,* 2908–2909; 10.1039/B310428A (2003).

55. Ye, S. *et al.* Unassisted Photoelectrochemical Cell with Multimediator Modulation for Solar Water Splitting Exceeding 4% Solar-to-Hydrogen Efficiency. *J. Am. Chem. Soc.* **143,** 12499–12508; 10.1021/jacs.1c00802 (2021).

56. Luo, J. *et al.* Targeting Ideal Dual-Absorber Tandem Water Splitting Using Perovskite Photovoltaics and $CuIn_xGa_{1-x}Se_2$ Photocathodes. *Adv. Energy Mater.* **5,** 1501520; 10.1002/aenm.201501520 (2015).

57. Cho, H.-H. *et al.* A semiconducting polymer bulk heterojunction photoanode for solar water oxidation. *Nat. Catal.* **4,** 431–438; 10.1038/s41929-021-00617-x (2021).

58. Sahu, A., Yadav, N. & Sudhakar, K. Floating photovoltaic power plant: A review. *Renewable Sustainable Energy Rev.* **66,** 815–824; 10.1016/j.rser.2016.08.051 (2016).

59. Shalaby, M. M., Nassar, I. N. & Abdallah, A. M. Evaporation suppression from open water surface using various floating covers with consideration of water ecology. *J. Hydrol.* **598,** 126482; 10.1016/j.jhydrol.2021.126482 (2021).

60. de Lima, R. L. P., Paxinou, K., C. Boogaard, F., Akkerman, O. & Lin, F.-Y. In-Situ Water Quality Observations under a Large-Scale Floating Solar Farm Using Sensors and Underwater Drones. *Sustainability* **13,** 6421; 10.3390/su13116421 (2021).

61. Karpouzoglou, T., Vlaswinkel, B. & van der Molen, J. Effects of large-scale floating (solar photovoltaic) platforms on hydrodynamics and primary production in a coastal sea from a water column model. *Ocean Sci.* **16,** 195–208; 10.5194/os-16-195-2020 (2020).

62. Pringle, A. M., Handler, R. M. & Pearce, J. M. Aquavoltaics: Synergies for dual use of water area for solar photovoltaic electricity generation and aquaculture. *Renewable Sustainable Energy Rev.* **80,** 572–584; 10.1016/j.rser.2017.05.191 (2017).

63. Pouran, H. M. From collapsed coal mines to floating solar farms, why China's new power stations matter. *Energy Policy* **123,** 414–420; 10.1016/j.enpol.2018.09.010 (2018).